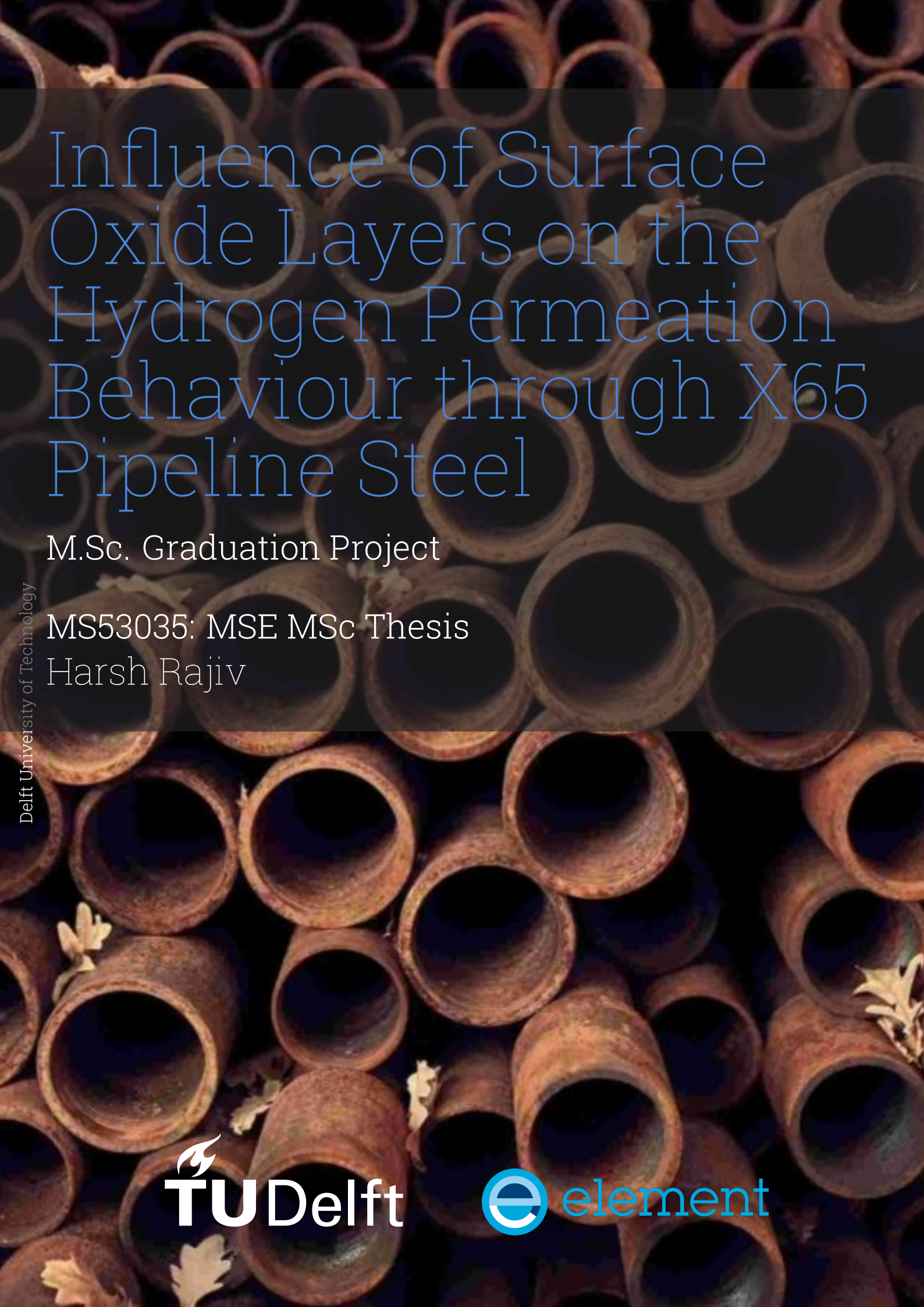

Influence of Surface Oxide Layers on the Hydrogen Permeation Behaviour through X65 Pipeline Steel

M.Sc. Graduation Project

MS53035: MSE MSc Thesis

Harsh Rajiv

Delft University of Technology

TU Delft

element

Influence of Surface Oxide Layers on the Hydrogen Permeation Behaviour through X65 Pipeline Steel

M.Sc. Graduation Project

by

Harsh Rajiv

to obtain the degree of Master of Science

at the Delft University of Technology,

to be defended publicly on January 31, 2025.

Student number:	5833949	
Project duration:	January 15, 2024 – January 31, 2025	
Thesis committee:	Prof. Yaiza Gonzalez-Garcia,	Supervisor, TU Delft
	Dr. Farid Afshar,	Supervisor, Element Materials Technology
	Prof. Poulumi Dey,	TU Delft

This thesis is confidential and cannot be made public until 31 December, 2025.

TU Delft element

Acknowledgements

My first and sincere gratitude goes to my project supervisors, Dr. Yaiza Gonzalez-Garcia and Dr. Farid Afshar, for their constant support and guidance throughout the duration of this challenging yet innovative project. This work would not have been possible without their efforts and encouragement. I also extend my heartfelt thanks to Element Materials Technology for giving me the opportunity to undertake this project and for their unwavering support throughout its course.

I would also like to thank Agnieszka Kooijman for her invaluable assistance and guidance in the electrochemical lab. She was always willing to answer my questions and provide support whenever needed, which greatly contributed to the success of this project.

My heartfelt thanks go to Tim Boot for not only providing me with the electrochemical permeation setup but also offering invaluable guidance on the setup procedure. His support ensured the smooth execution of these critical experiments.

I am also grateful to Amir Mohseni Armaki for his assistance and guidance during the Raman analysis, which helped me gain valuable insights into the material properties. My thanks also extend to Kees Kwakernaak for assisting with the Pd sputtering of the samples. Additionally, I would like to express my gratitude to Ehsan Rahimi for his support and expertise with the EIS fitting, which was crucial for interpreting the data accurately. I would also like to thank Prasad Gonugunta and Prasaanth Ravi Anusuyadevi for their invaluable help with performing the XPS analysis and fitting.

I would also like to acknowledge the assistance of the student assistants and technicians in the sample preparation labs.

Finally, I would like to extend my heartfelt thanks to my friends and family, whose constant support and encouragement helped me navigate through this project period. Their unwavering belief in me kept me motivated and grounded throughout this journey.

Harsh Rajiv

M.Sc. Student

January 21, 2025

TU Delft, the Netherlands

Abstract

The global transition to sustainable energy has accelerated the demand for hydrogen as a clean fuel source. Carbon steel pipelines play a vital role in hydrogen transport and storage infrastructure, but their potential susceptibility to hydrogen embrittlement poses a significant challenge. Hydrogen ingress, facilitated by environmental and operational factors, undermines the structural integrity of these steel pipelines, making it critical to develop strategies to mitigate hydrogen-induced degradation. The formation of internal surface oxide layers on these steels significantly influences hydrogen-material interaction processes, underscoring the need for further investigation and understanding, a focus of this study.

This study focuses on a naturally formed oxide layer on pipeline steel API 5L X65 and its role in influencing hydrogen permeation behaviour. Using characterization techniques including optical microscopy, scanning electron microscopy (SEM), energy-dispersive X-ray spectroscopy (EDS), and Raman spectroscopy, the composition and thickness of the oxide layer were studied.

Electrochemical hydrogen permeation experiments using the Devanathan–Stachurski (D-S) cell were performed on bare steel samples (with oxide removed from the surface) and oxide-covered steel samples. The results showed a significant delay in hydrogen permeation in the case of oxide-covered steel. An estimation of the hydrogen diffusion coefficient (D_{eff}) was carried out, showing significantly lower values for oxide-covered steel (5.57×10^{-10} cm^2/s and 7.13×10^{-11} cm^2/s) compared to bare steel (3.46×10^{-6} cm^2/s).

Electrochemical analysis by cyclic voltammetry (CV) and electrochemical impedance spectroscopy (EIS) of the surface before and after hydrogen charging revealed a significant degradation of the barrier properties of the oxide after charging. Further optimization of the experimental conditions during the D-S method will be necessary to verify that the oxide integrity is solely affected by hydrogen ingress and not by the potential or current applied during charging.

This research provides a better understanding of the properties of naturally formed oxide layers on pipeline steel and their role in mitigating hydrogen permeation. These insights contribute to a deeper understanding of the role of oxide layers in the hydrogen transportation steel infrastructure. Recognizing the significance of these interactions is crucial for developing accurate testing and qualification protocols to ensure the reliability and performance of these materials in hydrogen transport applications.

Contents

List of Figures

List of Tables

1

Introduction

In the context of the growing emphasis on renewable energy, ensuring safe and efficient transport of hydrogen via pipelines has become a critical issue. Steel pipes, preferred for their strength, durability, and resistance to corrosion, serve as the primary medium for fluid transportation. However, the likelihood of hydrogen embrittlement (HE) remains a challenge. This phenomenon of hydrogen permeation into steel, which results in increased brittleness and enhances the possibility of pipeline failure, requires detailed examination.

To mitigate these issues, steel plates designated for pipeline construction undergo rigorous production processes during thermomechanical controlled processing (TMCP) [1]. This involves the fine-tuning of various manufacturing parameters to strengthen the capabilities of pipeline steel. Key factors meticulously managed during the steel production process include the temperatures at which rolling and cooling occur, as well as the precise incorporation of micro-alloying elements [2]. Adjustments in these process variables, along with a carefully tailored chemical composition, have facilitated the creation of pipeline steel grades with superior mechanical qualities, while adhering to the standards established by API 5L [3]. One such pipeline steel grade is API 5L X65 steel. Nonetheless, enhancements in the mechanical properties of pipeline steel can inadvertently affect its corrosion resistance and susceptibility to cracking. Thus, it is insufficient to evaluate pipeline steel merely on the grounds of strength, toughness, and weldability. In the context of hydrogen transportation, a more comprehensive approach should also account for pipeline steel's compatibility with hydrogen-containing environments, ensuring that its properties are specifically tailored to withstand the unique challenges posed by hydrogen exposure in its intended application.

The majority of research into the interactions between hydrogen and steel has concentrated on the material's bulk, examining how microstructural features like phases, interfaces, and dislocations may affect hydrogen diffusion and serve as sites for reversible or irreversible hydrogen trapping [4, 5]. However, the condition of the material's surface, being the initial point of contact with potentially hydrogen-rich environments, warrants further attention. Structural steels (such as X65) tend to form surface oxide layers upon exposure to air or an oxygen-containing environment, the composition and thickness of which are dependent on the alloy composition and processing [6, 7]. The exposure of these steels to different environments during its use can alter or form new surface oxides, complicating the understanding of how the surface influences HE processes. These oxide layers that form on steel surfaces may act as barriers to hydrogen diffusion, thereby potentially mitigating the risk of embrittlement.

2

Background and Literature

The first section of this literature review is dedicated to characterizing the various types of surface oxide layers formed on steel, while exploring the external factors that may influence the key parameters of these layers. These oxide layers can be categorized into native oxide layers, corrosion-induced oxide layers, and high-temperature oxide layers, each with unique characteristics influenced by their formation conditions. Following this, the hydrogen/surface oxide layer interaction in steel is discussed in detail, examining the behaviour of these oxide layers under hydrogen exposure. This section also highlights their effectiveness in preventing hydrogen permeation into the steel substrate, which is crucial for applications such as hydrogen transport infrastructure. Understanding the hydrogen-oxide layer interaction and the relevant oxide layer parameters that influence this interaction provides a foundational context for evaluating and selecting appropriate experimental methodologies. This framework is essential for the formulation and execution of hydrogen permeation experiments on X65 steel, which is the focus of this thesis. The subsequent and last section of this literature review discusses the various experimental techniques used to evaluate hydrogen permeation in steel. These techniques are analysed for their applications, advantages, and limitations, with a particular focus on their relevance to steel specimens.

2.1. Formation and Characteristics of Surface Oxide Layers on Steel

Steel surfaces can develop various oxide layers, including native oxide layers, corrosion layers, and high-temperature oxide layers. Each type forms under specific environmental or processing conditions and significantly impacts the steel's durability and resistance to environmental factors. This section reviews the formation and characteristics of these layers.

2.1.1. Native Oxide Layers - Formation and Characteristics

Iron

The composition and thickness of the native oxide film on iron has been extensively studied by various researchers. Initial investigations into iron exposed to humid air (40–45% relative humidity) at room temperature revealed that the average thickness of the native oxide film ranges between 1 and 3 nm within the first 24 hours of exposure, showing minimal increase subsequently, as found in studies [8, 9, 10]. This thickness range for short exposure durations was similarly identified in later research [11, 12, 13].

It is generally agreed among researchers that the native oxide film on iron features a layered composition of oxides and oxyhydroxides. However, there is no consensus on the exact layered composition of the native oxide layer. Nagayama et al. [14] discovered that on pure iron exposed to air for 3–14 days, the oxide film is composed of an external γ-FeOOH layer and an internal Fe_3O_4 layer. Grosvenor et al. [15] identified that upon exposure to water vapour (with a dose of 10^8 L) at ambient temperature, the resulting oxide film on pure iron formed after 5 minutes displayed a duplex structure composed of FeOOH and Fe_3O_4, with a thickness of less than 2.0 nm. In contrast, when reacting with an equivalent dose of O_2, the film formed a layered structure consisting of γ-Fe_2O_3 on top of Fe_3O_4, reaching a total thickness of approximately 3.5 nm. Furthermore, Suzuki et al. [16] observed that the native oxide layer on pure iron, after 15 years of exposure to air at room temperature, comprises an inner Fe_2O_3 layer and an external FeOOH layer, as shown in figure 2.1.

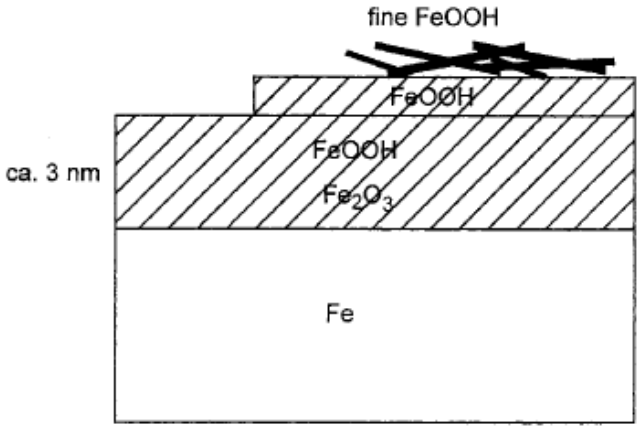

Figure 2.1: Schematic illustration of the layered structure consisting of oxide and oxyhydroxide formed on the surface of high-purity iron [16].

The differences in the compositions of the native oxide layers formed on iron reported by the various authors can be attributed to the considerable variation in exposure times and variations in moisture content present in the exposed environments. The findings by Grosvenor et al. [15] indicate the preferential formation of a FeOOH top layer over a γ-Fe_2O_3 top layer if the iron sample is exposed to environments containing higher amounts of water vapour. However, further analysis is required to identify the exact relative humidity conditions for such preferential formation. The results by Suzuki et al. [16] point towards the preferential formation of an inner γ-Fe_2O_3 layer compared to a Fe_3O_4 layer after long-term exposure to air. However, insufficient literature with a comparable exposure period is present to confirm this hypothesis.

On the basis of the existing research mentioned above, it can be hypothesized that the native oxide layer on iron undergoes a gradual oxidation process with increasing exposure time, starting from the outermost layer to the innermost layer.

Carbon Steels

Investigations into the characteristics of the native oxide layer on carbon steels have been limited, as mentioned in the previous section. This section will focus on a key piece of literature which investigated the native oxide layer formed on carbon steels.

Chan-Rosado and Pech-Canul [17] investigated the influence of air exposure at 45% relative humidity for 4 hours, 24 hours and 120 hours on the native oxide layer of AISI 1018 carbon

steel. XPS analysis revealed that: i) prolonged exposure to air led to continuous oxidation of the oxide layer, marked by a gradual conversion from Fe(II) to Fe(III), ii) the oxide layer featured a dual-layer structure, comprising an inner Fe_3O_4 oxide region and an outer FeOOH oxyhydroxide region, and iii) Fe(II) predominantly resided in the inner oxide region, with its proportion diminishing with increased air exposure, whereas the presence of FeOOH experienced an uptick. An estimation of the native oxide layer thickness was made using the Strohmeier equation [18], which utilizes the intensities of the Fe $2p_{3/2}$ photoelectron peaks of the metal and oxide:

$$d = \lambda_{ox} \cos\theta \ln\left(1 + (N_m \lambda_m I_{ox} / N_{ox} \lambda_{ox} I_m)\right) \tag{2.1}$$

As a first approximation, it is assumed that the steel is covered by a homogeneous Fe_3O_4 layer. Here, λ_{ox} and λ_m are attenuation lengths of photoelectrons emitted by the Fe $2p_{3/2}$ core level in the oxide and in the bulk metal, respectively. θ is the takeoff angle of photoelectrons w.r.t. the normal, N_m and N_{ox} represent the atomic densities of iron in the metal and in the oxide, respectively. I_m and I_{ox} represent the intensities of the Fe $2p_{3/2}$ photoelectron peaks of the metal (the peak area of Fe(0)) and the oxide (sum of the peak areas of Fe(III) and Fe(II)), respectively. Values of λ and N were taken from existing literature [19, 20].

XPS was performed after the three aforementioned exposure times and at three takeoff angles of θ = 0°, 30° and 50°. As can be seen in figure 2.2, average film thicknesses of 3.2, 3.6 and 4.5 nm were estimated after exposure times of 4 hours, 24 hours and 120 hours, respectively.

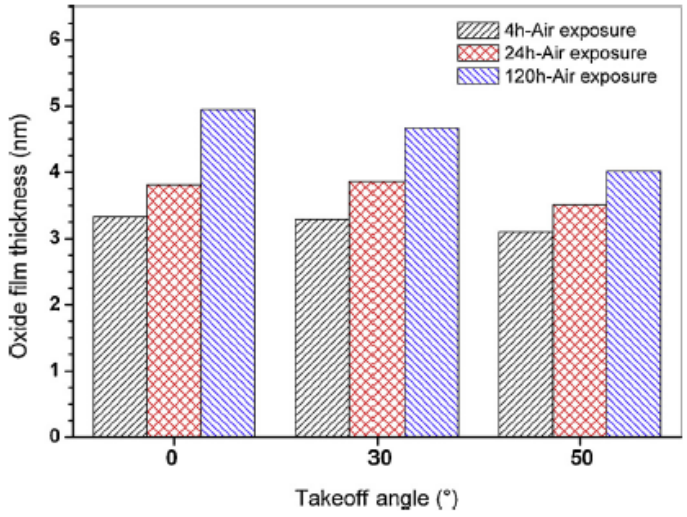

Figure 2.2: Estimated values of the native oxide film thickness (after 3 exposure times in air) using Eqn.(2) and (Fe(II)+Fe(III))/Fe^0 intensity ratios obtained at three takeoff angles [17].

Suzuki et al. [13] reported native oxide layer thicknesses of around 2.5 nm on high-purity iron after short-term exposure to air, while Frankenthal et al. [21] reported thicknesses of 5-6 nm after 20 years of exposure. With regards to thickness, the calculated native oxide layer thicknesses by Chan-Rosado and Pech-Canul for carbon steels were within these range of values. However, these values consider a homogeneous Fe_3O_4 layer, distinctly different from the observed dual-layer structure of the native oxide layer. In order to calculate accurate thickness values in line with the actual dual-layer structure, a modification of the Strohmeier equation is required.

With regards to composition, the reported dual-layer structure of the native oxide layer was in agreement with those reported by Nagayama et al. [14] and Grosvenor et al. [15] for iron. On the basis of this finding, it can be hypothesized that iron and carbon steels exhibit similar native oxide layer compositions if exposed to environments with similar moisture content. However, due to insufficient research reporting the native oxide layer composition of carbon steels, further investigation is required to confirm this hypothesis.

Influence of Exposure Time - Carbon Steels

Existing literature has highlighted that exposure time is a critical parameter to take into account when studying the composition and thickness of the native oxide layer on carbon steels. Chan-Rosado and Pech-Canul [17] performed XPS analysis in order to investigate the influence of air exposure at 45% relative humidity for 4 hours, 24 hours and 120 hours on the native oxide layer of a carbon steel. Using the Strohmeier equation, only a slight increase in the oxide layer thickness with exposure time was reported, which was in agreement with existing literature [13, 21, 22, 23]. However, the calculations were made considering the native oxide layer to be a homogeneous Fe_3O_4 layer as a first approximation, which doesn't accurately represent the dual-layer structure proposed by the authors.

Regarding the composition of the native oxide layer, the authors reported a continuous oxidation of the layer from Fe(II) to Fe(III) with increasing exposure time to air. Figure 2.3 supports this assertion by illustrating an increase in the ratio of Fe(III) to Fe(II) peak areas obtained from the XPS spectra for the native oxide layers with increased exposure time to air. Existing research by Elsener et al. [23] also reports similar behaviour for the native oxide layer. The observation of Fe(III) to Fe(II) peak areas gradually tending to a 2:1 ratio supports the hypothesis of an inner Fe_3O_4 layer, which was also proposed by earlier investigations [14, 15, 24]. Additionally, a decrease in the ratio of (O^{2-}) lattice to (OH^-) lattice peak areas with increased exposure time to air can also be seen in figure 2.3. This supports the hypothesis put forth by other authors [23, 24, 25] of an outer FeOOH layer whose concentration increases with exposure to air.

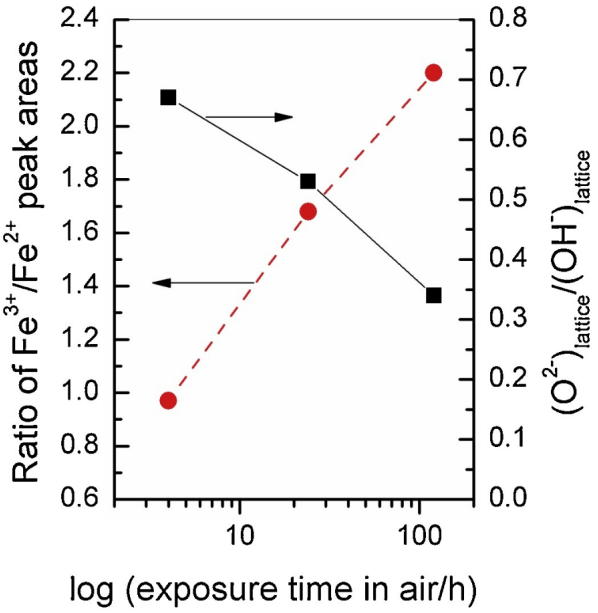

Figure 2.3: Peak area ratios for Fe(III) to Fe(II) and (O^{2-}) lattice to (OH^-) lattice derived from the XPS spectra obtained for the native oxide films, as a function of exposure time in air [17].

To summarize, this section focused on investigating the composition and thickness of native oxide layers formed on iron and carbon steels. Both types of materials tend to form native oxide layers in the 2-6 nm thickness range for a majority of exposure times. Additionally, it may be hypothesized that iron and carbon steels tend to form similar native oxide layer compositions (inner Fe_3O_4 layer and outer FeOOH/Fe_2O_3 layer) if exposed to environments with similar moisture content. However, insufficient literature on the native oxide layer formed on carbon steels is available to confirm this hypothesis.

2.1.2. Corrosion Layers - Formation and Characteristics

Corrosion layer formation on steel (also known as rust) involves the development of oxide and hydroxide phases that vary in composition, structure, and protective quality based on environmental exposure. Figure 2.4 illustrates the dual structure of a corrosion layer formed in one such exposure case. Table 2.1 shows the corrosion products most frequently found in the corrosion layers formed on mild steel exposed to the atmosphere [26]. Key factors like humidity, atmospheric composition, and alloying elements influence the thickness, compactness, and stability of these layers, impacting steel's overall corrosion resistance. This section discusses how these conditions shape corrosion layer characteristics on various steel types.

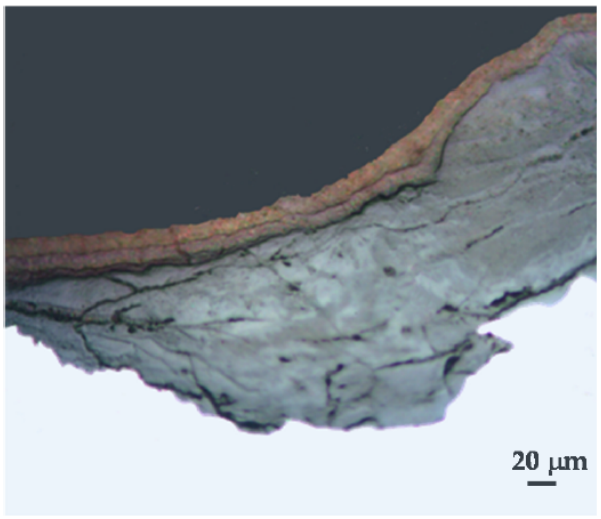

Figure 2.4: Dual structure of a consolidated rust layer formed on carbon steel during one year of exposure to unsheltered conditions in a marine atmosphere with low chloride deposit (21 mg $Cl^-/m^2 \cdot d$) [27]. The outer orange-coloured layer is mainly lepidocrocite while the inner greyish layer is mainly goethite and magnetite [28].

De la Fuente et al. [26] aimed to investigate the composition, morphology, and structure of corrosion layers formed on mild steel after long-term exposure to various atmospheres (summarized in table 2.2). They found that these layers consist primarily of lepidocrocite (γ-FeOOH) and goethite (α-FeOOH), which are commonly present across all environments. Table 2.3 shows the crystalline phases encountered in the corrosion products formed on mild steel in the different atmospheres.

Name	Composition
Oxides	
Haematite	α-Fe_2O_3
Maghemite	γ-Fe_2O_3
Magnetite	Fe_3O_4
Ferrihydrite	$Fe_5HO_8 \cdot 4H_2O$
Hydroxides	
Ferrous hydroxide	$Fe(OH)_2$
Ferric hydroxide	$Fe(OH)_3$
Goethite	α-FeOOH
Akaganeite	β-FeOOH
Lepidocrocite	γ-FeOOH
Feroxyhyte	δ-FeOOH
Others	
Ferrous chloride	$FeCl_2$
Ferric chloride	$FeCl_3$
Ferrous sulphate	$FeSO_4$
Ferric sulphate	$Fe_2(SO_4)_3$

Table 2.1: Some of the chemical species found in rust layers [26].

Atmosphere	Test Site	Time of Wetness (h/year)	SO_2 Deposition Rate (mg/m^{2}d)	Cl^- Deposition Rate (mg/m^{2}d)
Rural	El Escorial	3900	8	Negligible
Urban	Madrid	2100	56	Negligible
Industrial	Bilbao	3000	81	41
Marine (Light)	Barcelona	3200	52	27
Marine (Severe)	Alicante	4300	126	219

Table 2.2: Atmospheric corrosion stations: Environmental characteristics (modified from [26]).

Atmosphere	Test Site	γ-FeOOH (%)	α-FeOOH (%)	β-FeOOH (%)	Fe_3O_4/γ-Fe_2O_3 (%)	α-Fe_2O_3 (%)
Rural	El Escorial	60.6	24.6	–	14.8	–
Urban	Madrid	60.6	24.6	–	14.8	–
Industrial	Bilbao	46.5	18.9	–	11.4	23.3
Marine (Light)	Barcelona	39.1	15.8	35.5	9.6	–
Marine (Severe)	Alicante	43.2	17.5	39.3	–	–

Table 2.3: Crystalline phases of corrosion products on mild steel in different atmospheres (modified from [26]).

The corrosion layers in these different environments are typically structured into distinct zones. Lepidocrocite (γ-FeOOH) tends to form the outermost layer, providing a protective but porous barrier. In more aggressive marine conditions, akaganeite (β-FeOOH), which readily incorporates chloride ions, accumulates in the outer regions, increasing the layer's permeability and thus vulnerability to further chloride penetration. In industrial atmospheres with higher sulphur dioxide levels, magnetite (Fe_3O_4) and maghemite (γ-Fe_2O_3) are typically found in intermediate

layers, where lower oxygen availability favours their formation. In particularly severe industrial settings, haematite (α-Fe_2O_3) and ferrihydrite ($Fe_5HO_8 \cdot 4H_2O$) are also found, forming dense inner layers that resist further corrosion by blocking ion diffusion.

The study by Xiao et al. [29], which investigated corrosion layers formed on carbon steel under controlled humidity and exposure durations, also identified lepidocrocite (γ-FeOOH) and maghemite (γ-Fe_2O_3) as primary phases during early corrosion. However, unlike De la Fuente et al., Xiao et al. focused on initial exposure stages (1–30 days) and analysed the role of humidity, finding that increased moisture expedited the formation of denser oxides like goethite (α-FeOOH), which developed into compact layers that adhered well to the steel surface. This led to faster growth in thickness but with better adherence and compaction, reducing flaking or spalling risks. Over time, prolonged humidity exposure in Xiao's study resulted in a transition to goethite-dominant layers, which Xiao et al. found to offer a more stable, protective barrier than the porous lepidocrocite structures identified by De la Fuente et al.

In contrast to De la Fuente et al., who observed high variability in layer thicknesses across atmospheric conditions (ranging from 100–300 µm), Xiao's controlled conditions allowed for uniform layer growth, emphasizing the importance of environmental stability. Both studies underscore humidity's crucial role in influencing corrosion rate, morphology, and layer compactness, with Xiao's findings aligning with De la Fuente's observations in humid, chloride-rich marine atmospheres. However, De la Fuente's study extends beyond humidity, incorporating factors such as sulphur dioxide and chloride deposition rates, which were shown to shape not only the corrosion rate but also the chemical composition and stratification of corrosion layers over extended exposure times.

Asami and Kikuchi's [30] investigation into long-term corrosion in coastal-industrial environments demonstrated that weathering steels, enriched with alloying elements like copper and chromium, form dense, compact corrosion layers primarily composed of goethite (α-FeOOH), which effectively blocks chloride penetration and enhances corrosion resistance in coastal-industrial environments. In contrast, plain carbon steel, lacking these protective alloys, displayed higher concentrations of akaganeite (β-FeOOH) in thicker, outer rust layers. This phase's affinity for chloride resulted in porous, less stable structures that facilitated chloride ingress and accelerated corrosion. Both materials contained magnetite (Fe_3O_4) near the steel interface, but weathering steels' higher α-FeOOH and lower β-FeOOH content contributed to a more stable, protective rust layer overall.

Compared with De la Fuente et al. [26], who examined plain mild steel across various atmospheres and observed that compacted goethite (α-FeOOH) layers offer moderate protection, Asami and Kikuchi's study highlights the additional corrosion resistance achieved with alloying elements in weathering steels, especially under high-chloride conditions. Both studies agree that dense, α-FeOOH-rich layers provide enhanced protection; however, Asami and Kikuchi emphasize that alloying elements like copper and chromium in weathering steels significantly improve this protective effect by promoting a compact, stable layer that effectively blocks chloride ions, unlike plain steel, which forms more porous, chloride-permeable layers rich in akaganeite (β-FeOOH) in similar conditions.

Similarly, Xiao et al. [29] supports the importance of layer compactness, showing that higher humidity levels foster the formation of denser, protective oxides in controlled settings. Xiao's findings align with both De la Fuente's and Asami and Kikuchi's conclusions on the value of compact corrosion layers, particularly in challenging environments.

In summary, the studies reviewed demonstrate that the composition, thickness, and compactness of corrosion layers on steel are critically influenced by environmental conditions, material composition, and exposure duration. Factors such as humidity, chloride, and sulphur dioxide levels play essential roles in determining the phases that form within rust layers, with increased humidity promoting denser oxides like goethite (α-FeOOH), which provides more stable, protective coverage. In chloride-rich environments, phases like akaganeite (β-FeOOH) emerge, particularly on plain carbon steels, leading to porous, less protective layers that enable further ion ingress and accelerate corrosion. The presence of alloying elements in weathering steels fosters the formation of compact and stable (α-FeOOH) layers that resist chloride penetration, maintaining layer integrity and offering enhanced corrosion resistance.

2.1.3. High Temperature Oxide Layers - Formation and Characteristics

In the conventional flat hot-rolling process for steel production, oxide scale formation is a significant concern due to the exposure of steel surfaces to high temperatures in oxidizing environments. As the steel is heated, iron reacts with oxygen, forming layers of iron oxides such as wustite (FeO), magnetite (Fe_3O_4), and haematite (Fe_2O_3). These oxide scales initially serve as barriers to further oxidation but can negatively affect the surface quality of the steel if not properly managed. The hot-rolling process includes key stages — slab reheating, roughing rolling, and finishing rolling [31] — during which different scales form, classified as primary, secondary, and tertiary.

During slab reheating, a thick primary scale layer [31, 32] forms due to the oxidizing atmosphere in the furnace. This scale, consisting of wustite, magnetite, and haematite, is removed by a hydraulic descaler before the steel enters roughing rolling, where the steel undergoes multiple passes to reduce its thickness. During this stage, secondary scale [31, 33] forms, which is thinner than the primary scale and is removed using high-pressure water between passes. In the finishing rolling stage, the steel is further reduced to a strip with a thickness of 1.2 to 12 mm. During and after this process, tertiary scale [31, 33] forms and remains on the steel surface as it is coiled.

Chen and Yuen [34] explored the oxidation behaviour of pure iron and various types of carbon steels under high-temperature conditions, particularly in the range of 700°C to 1250°C. The study focused on how the oxidation process affected the composition, thickness, and compactness of oxide layers formed at the various conditions.

The formation and characteristics of oxide scales during steel oxidation are influenced by several critical parameters, including temperature, atmosphere composition, cooling rate, and oxidation time. Each parameter plays a crucial role in determining the composition, thickness, and compactness of the oxide layers that form on the steel surface.

Influence of Temperature

Temperature significantly impacts oxide scale formation on iron and steel, with distinct behaviours across various ranges. Chen and Yuen [35] identified that in the range of 450–560°C, both SAE-AISI 1006 steel and pure iron form two-layer scales of haematite (Fe_2O_3) and magnetite (Fe_3O_4), though steel scales are less stable and prone to detachment, especially on cold-rolled samples. In contrast, pure iron forms more stable, well-adhered layers, particularly when cold-worked [36, 37]. Wüstite was not present due to its thermodynamic instability at temperatures below 570°C [38].

In the 580–760°C range, steel oxidation produces primarily haematite and magnetite, with sporadic wüstite (FeO) formation above 660°C; the haematite layer often grows thick enough

to dominate the scale [35]. Pure iron develops a more defined three-layer structure with a thick inner wüstite layer, intermediate magnetite, and outer haematite [39, 40].

Above 700°C, oxide scale formation becomes increasingly sensitive to temperature, with blistering becoming prominent in the 980–1100°C range. Here, blistering results in irregular scale structures due to scale detachment, interrupting outward iron diffusion and causing local wüstite to convert into higher oxides [35, 41]. In this range, wüstite's increased plasticity allows stress relief through blistering, while gases such as CO or N_2 accumulate beneath the scale, forming pockmarks or raised areas [42, 43]. Blistering slows the oxidation rate, peaking scale thickness near 980–1010°C [44, 45, 46]. As temperatures exceed 1100°C, blistering diminishes, allowing oxidation to proceed more uniformly.

Overall, temperature directly affects the composition, thickness, and stability of oxide scales on steel and iron, with higher temperatures promoting thicker, multi-layered scales but also introducing blistering and structural irregularities that compromise stability.

Influence of Atmosphere Composition

The influence of atmospheric composition, particularly relative humidity and oxygen partial pressure, plays a crucial role in the oxidation behaviour and scale formation on Fe–C alloys, iron, and mild steel. Baud et al. [47] investigated the effect of relative humidity on the oxidation behaviour of Fe–C alloys (0.4 and 0.5 wt.% C) at 700–735°C, using dry air, ambient air (1–2% water vapour), and moist air (31% water vapour) over oxidation periods ranging from 2 to 256 hours. They found that water vapour significantly enhanced the oxidation rate, resulting in thicker, more adherent oxide scales by promoting the diffusion of iron ions. In contrast, dry air often led to scale detachment from the alloy, likely due to the presence of cementite, resulting in lower oxidation rates. Atmospheric composition thus directly influenced the scale's growth kinetics and final structure, with water vapour uniquely impacting the Fe–C alloys by increasing oxidation rates and adherence, while having minimal effect on the oxidation behaviour of pure iron.

Additionally, previous research [48, 49] has also shown that oxygen partial pressure significantly affected the initial oxidation rate of iron and mild steel at elevated temperatures. For pure iron at 800–1000°C, Goursat and Smeltzer [48] found that higher oxygen pressures increased haematite formation on the surface, while wüstite dominated 95% the scale, and oxidation followed a parabolic rate law that was independent of oxygen pressure. Similarly, Abuluwefa et al. [49] observed that for mild steel at 1000–1250°C, initial oxidation followed a linear rate law, with rate constants increasing alongside oxygen pressure up to 15% before transitioning to a parabolic, pressure-independent phase. Together, these findings indicate that while higher oxygen pressures enhance initial oxidation and scale thickness, steady-state oxidation remains pressure-independent under parabolic kinetics.

In summary, atmospheric composition—whether in terms of humidity or oxygen pressure—affects both the growth rate and stability of oxide scales, highlighting its critical role in controlling the oxidation behaviour of steel and Fe–C alloys.

Influence of Cooling Rate

The cooling rate after high-temperature oxidation plays a critical role in determining the thickness, composition, and structural integrity of the oxide scale on mild steel. Rapid cooling tends to trap wüstite as the dominant phase, producing thinner, less compact oxide layers prone to defects because the limited time prevents further phase transformation. In contrast, slower cooling rates allow wüstite to transform more fully into stable phases like magnetite and

haematite, resulting in thicker, denser, and more adherent oxide scales that offer enhanced oxidation resistance [35].

Chen and Yuen's study [35] on low-carbon, low-silicon mild steel at 880–900°C for 12 seconds further illustrates these cooling rate effects. At high cooling rates (15–60°C/min), the oxide scale structure was consistent, with a magnetite-to-wüstite thickness ratio of approximately 1:7 and the formation of magnetite precipitates near the magnetite layer, creating a total scale thickness of about 30–31 µm. However, as cooling rates decreased to 30, 15, and 5°C/min, scale thicknesses increased to 35, 46, and 74 µm, respectively. At the slowest rate (5°C/min), an Fe_3O_4/Fe eutectoid began to form near the magnetite layer, and a thicker haematite layer developed on the surface. These findings indicate that slower cooling rates allow for complete oxide transformations, producing thicker, more protective scales, whereas rapid cooling restricts oxidation, leading to thinner and less stable oxide layers.

Influence of Oxidation Time

Oxidation time, in combination with temperature, plays a crucial role in determining oxide scale structure, thickness, and stability on steel. In the 450–560°C range, short exposure produces a stable two-layered scale of magnetite and haematite, but with extended oxidation, detachment issues arise, particularly on cold-rolled samples. At intermediate temperatures (580–760°C), short oxidation times yield a three-layer scale similar to that on pure iron, with a thick inner wüstite layer, a middle magnetite layer, and a thin haematite surface layer [35, 40, 50]. However, prolonged exposure in this range initiates blistering, which disrupts iron diffusion and converts detached wüstite into higher oxides, introducing structural irregularities [35, 41].

At higher temperatures (980–1100°C), extended oxidation significantly increases blistering, causing initial growth in scale thickness to peak around 980–1010°C before decreasing until 1100°C due to blister-related disruptions [44, 45, 46]. Figure 2.5 illustrates this relationship between oxidation time, oxidation temperature and blistering. This blistering weakens scale stability, producing thicker but more irregular and less adherent scales, especially in carbon-containing steels [35, 41]. Overall, longer oxidation times at each temperature range lead to increasingly thick but unstable oxide layers, with blistering as a primary factor compromising scale integrity.

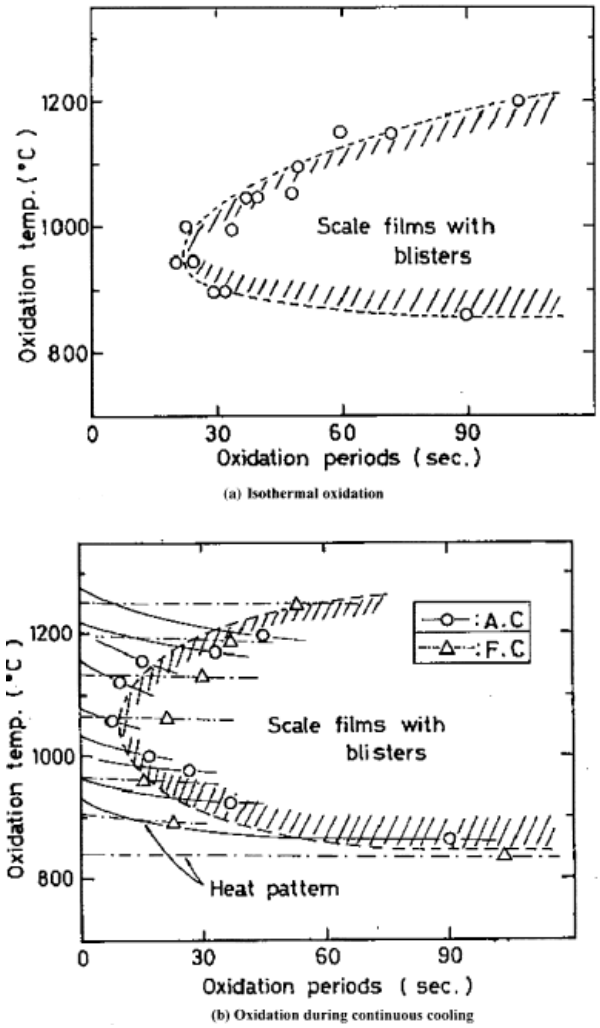

Figure 2.5: Blistering behaviour of scale films during steel oxidation: (a) Isothermal oxidation; (b) oxidation during continuous cooling [41].

In summary, the composition, thickness, and stability of oxide scales on steel are significantly influenced by temperature, atmosphere composition, cooling rate, and oxidation time, with each parameter uniquely shaping the scale's structure and protective effectiveness. Effective control over these variables is essential to optimize oxide layer characteristics, ensuring durability and performance in high-temperature applications.

2.2. Interaction of Hydrogen with Oxide Layer on Steel

The detrimental process of HE in steel is generally attributed to three primary mechanisms: (i) Hydrogen-Enhanced Decohesion (HEDE), (ii) Hydrogen-Enhanced Localized Plasticity (HELP), and (iii) Adsorption-Induced Dislocation Emission (AIDE). However, hydrogen absorption into steel occurs before HE can occur, with even small amounts causing significant reductions in the mechanical properties of the material [51, 52]. This takes place in a sequence of events — starting with the absorption of hydrogen at the surface, progressing through absorption into the metal microstructure, and culminating in diffusion and trapping [53] — that ultimately enhance the possibility of various forms of structural deterioration, such as blistering, flaking, and hydrogen-induced cracking (HIC). Such phenomena represent persistent challenges across a wide range of materials, especially high-strength steels (with tensile strengths exceeding 1000 MPa), which demonstrate increased susceptibility to hydrogen-induced delayed fracture [54, 55].

In the context of pipeline steels such as X65, hydrogen-induced pipeline degradation is strongly dependent on the trapping behaviour of the various microstructural features within the steel lattice structure [56]. As can be seen in figure 2.6, these features, such as dislocations, grain boundaries, alloying elements, defects, and interfaces, can act as potential hydrogen traps. These traps can either be reversible or irreversible in nature. Irreversible trap sites (such as inclusions and interfaces) are characterized by high potential energy barriers that prevent the escape of hydrogen atoms [57]. On the other hand, reversible trap sites (such as dislocations and grain boundaries) are characterized by lower potential energy barriers that permit the escape of hydrogen atoms. It is suggested that while a high concentration of irreversible hydrogen traps in steel increases the total hydrogen content, it also reduces the amount of diffusible hydrogen within the lattice, which is unlike when a high concentration of reversible hydrogen traps are present. This depletion of diffusible hydrogen may limit the hydrogen available for crack initiation and propagation, which lowers the chances of HE [57, 58, 59, 60, 61].

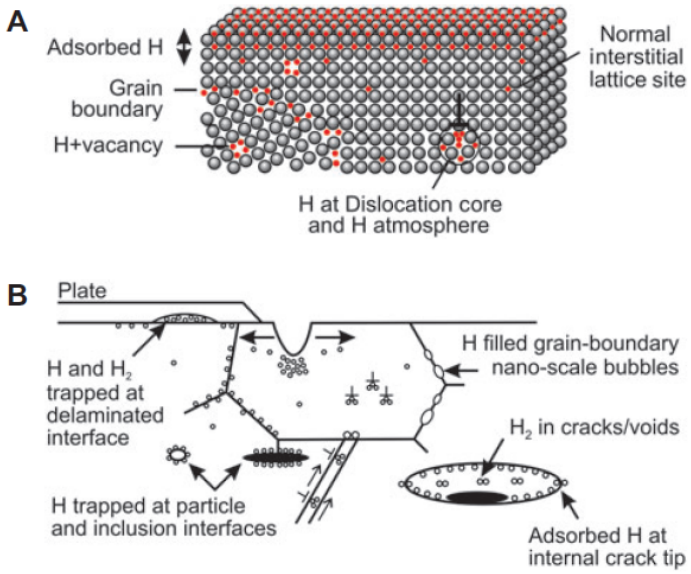

Figure 2.6: Schematic illustrations of sites and traps for hydrogen in materials (A) on the atomic scale, and (B) on a microscopic scale [62].

Therefore, examining how hydrogen permeates, is trapped, and is distributed within pipeline steels is crucial for assessing their vulnerability to HIC and gaining a better understanding of

the mechanisms behind their failure.

The majority of research into the interactions between hydrogen and metal has concentrated on the influence of bulk microstructural features on hydrogen diffusion and trapping [63, 64]. However, any oxide layer on the metal surface is significant, as it serves as the initial point of contact in an environment containing hydrogen, possibly trapping hydrogen and influencing its permeation into the metal [65]. The previous section illustrated that both carbon and stainless steels tend to form various types of surface oxide layers upon exposure to the atmosphere, varying in composition and thickness based on several factors. Hence, a review of the existing literature investigating this hydrogen/surface oxide interaction is required to establish the extent of hydrogen permeation and trapping into the steel in the presence of surface oxide layers. Additionally, identification of the relevant oxide layer parameters that influence this interaction is paramount.

2.2.1. Oxide Layer Characteristics Influencing Hydrogen Permeation

In order to effectively characterize the hydrogen/surface oxide interaction in steel, the various characteristics of oxide layers formed on steel surfaces need to be identified before examining their impact on the extent of hydrogen permeation through these layers. This section delves into the primary oxide layer parameters identified in existing research that significantly influence hydrogen permeation behaviour in steels, providing a detailed investigation of each factor's role and effect.

Thickness

In this subsection, existing research was investigated in order to collectively evaluate the influence of oxide layer thickness in influencing hydrogen permeation resistance.

Using a DS setup, Rubben et al. [65] investigated the hydrogen discharging behaviour through single-layered (magnetite) and bi-layered (inner magnetite/outer haematite) oxides thermally grown on the exit surface of SAE 1010 steel. They reported that increased thickness of the magnetite layer reduced the hydrogen flow rate (refer to figure 2.7) and led to a minor reduction in the total amount of oxidized hydrogen from the exit surface (refer to figure 2.8). These effects were due to the lower diffusion speed through the magnetite layer [66, 67] and minimal bulk trapping effects within the layer [58], respectively. However, the influence of increased thickness was more limited for the magnetite layer compared to the bi-layered oxide, suggesting that the steel/magnetite interface played a more critical role than thickness alone. This was supported by findings from figure 2.8, which showed that while a 26 nm-thick magnetite layer reduced the total oxidized hydrogen by half compared to a blank specimen, doubling the thickness to 51 nm resulted in only a minor additional decrease.

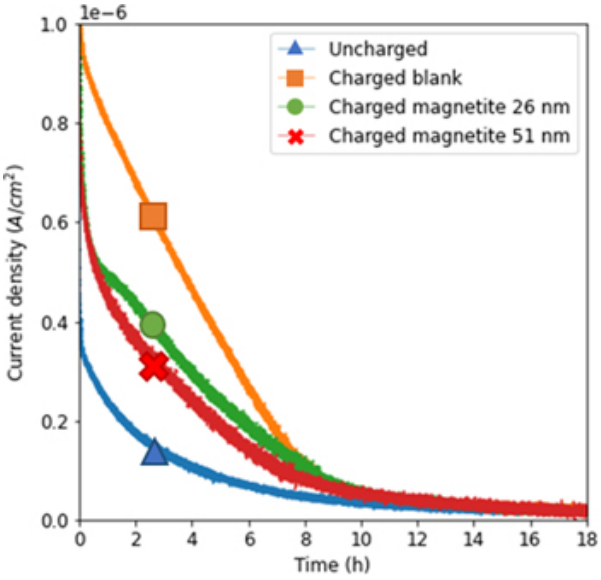

Figure 2.7: Chronoamperometric curve of the discharging step after 1.5 hours of charging, comparing specimens with and without magnetite layers of varying thickness [65].

The amount of hydrogen that was oxidised during discharging could be calculated from the chronoamperometric curves using Faraday's law of electrolysis:

$$n(H_{discharging}) = Q_{discharging}/zF = \int I_{discharging}dt/zF = \int J_{discharging}Adt/zF \qquad (2.2)$$

where J is the current density, A is the exposed surface area, z is the valency and F is the Faraday constant.

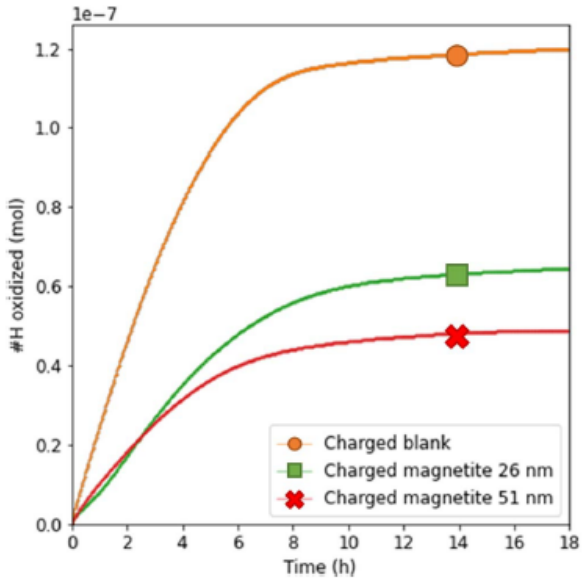

Figure 2.8: Amount of hydrogen that was oxidized at the exit side during the discharging step after 1.5 hours of charging [65].

Chikada et al. [68] investigated the influence of erbium oxide (Er_2O_3) coating thickness on deuterium permeation through ferritic/martensitic steel using a gas-phase permeation setup.

Figure 2.9 illustrates the relationship between permeability and temperature for the various oxide coatings investigated. The study found that increasing the coating thickness on both the HPV (high-pressure volume) and LPV (low-pressure volume) side directly reduced deuterium permeability by extending the diffusion path, with thicker coatings offering greater resistance. However, coating both sides of the substrate dramatically reduced permeability - up to two orders of magnitude lower compared to single-sided coatings of equivalent total thickness - suggesting that barriers on both sides independently contributed to overall resistance. This implies that the erbium coating's effectiveness in reducing deuterium permeability was not solely due to providing a longer diffusion pathway. This aligns with Rubben et al. [65]'s findings, reinforcing the idea that while thickness improves resistance, the effect is subject to a point of non-linear saturation and other structural considerations. Additionally, coatings of equal thickness on the HPV side reduced deuterium permeability more than those on the LPV side, as can be seen in figure 2.10. The authors attributed this behaviour to the difference in driving pressure for the reactions occurring at the HPV and LPV sides. This would imply that the adsorption of deuterium into the erbium coating is the more efficient permeability-reducing step compared to the desorption of deuterium out of the erbium coating.

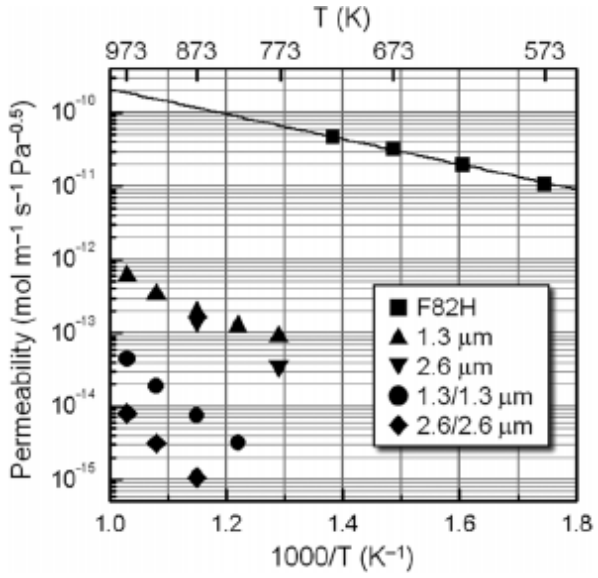

Figure 2.9: Arrhenius plots of deuterium permeability of the substrate and the coated samples deposited on one side and both sides [68].

Li et al. [69] investigated the influence of coating thickness on the permeation reduction factor (PRF) of Er_2O_3 hydrogen isotope permeation barriers. They found that thinner coatings (0.2 μm) effectively reduced deuterium permeation by a factor of 1/10 to 1/20 at temperatures between 300 °C and 600 °C. However, as the coating thickness increased beyond 0.2 μm, the PRF decreased. This reduction in permeation resistance with thicker coatings was attributed to the development of cracks and intrinsic stresses within the coatings, which allowed for increased deuterium permeation and reduced barrier effectiveness. This finding aligns with those of Rubben et al. [65] and Chikada et al. [68], emphasizing that while initial thickness can enhance barrier properties, excessive thickness may introduce structural vulnerabilities.

Li et al. [70] investigated the reduction factor for deuterium permeability (D-PRF) of Al_2O_3 coatings on 316L stainless steel, finding that it remained relatively constant with coating thickness from 0.2 to 1.6 μm. At thinner dimensions, the barrier effect was primarily due to surface interactions, where the microstructure and density of the coating played vital roles in resisting

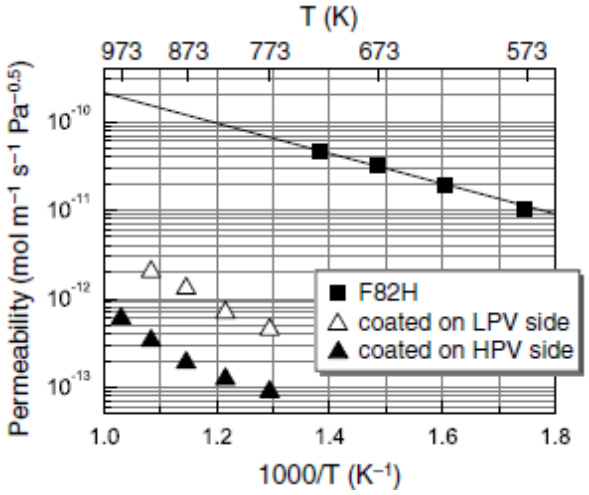

Figure 2.10: Comparison of deuterium permeability between the 1.3μm thick coatings facing the HPV and the LPV [68].

hydrogen diffusion. However, beyond a certain threshold thickness, the intrinsic properties of the coating material began to dominate, leading to improved performance in preventing hydrogen permeation. This suggests that while increased thickness can enhance barrier effectiveness, the relationship is not linear, and optimal thickness must be carefully considered. This result builds on the findings by Chikada et al. [68] and Rubben et al. [65], suggesting that thickness should be balanced with microstructural integrity for optimal permeation resistance.

Ishikawa et al. [71] investigated the effect of oxide layer thickness on deuterium permeation in 316L stainless steel, focusing on Fe and Cr oxides formed under controlled oxidation. The study found that Cr-rich oxide layers significantly reduced deuterium permeability and diffusion coefficients as thickness increased, particularly up to about 100 Å, demonstrating an effective barrier. In contrast, Fe-rich oxide layers showed minimal change in permeability and diffusion with increased thickness, indicating a less effective barrier. The results suggest that Cr-rich oxides, especially with higher Cr/(Cr + Fe) ratios, are more effective at reducing hydrogen permeation, emphasizing the importance of both oxide composition and thickness in optimizing barrier performance. This agrees with Rubben et al. [65], Chikada et al. [68], and Li et al. [69], reinforcing that while increased thickness can enhance resistance, other factors like composition, microstructural stability, and oxide/steel interfaces play equally, if not more, significant roles.

Compactness

This subsection reviews existing research to identify the role of oxide layer compactness in affecting hydrogen permeation resistance.

Zhang et al. [72] investigated the influence of different oxide films on hydrogen permeation and embrittlement in X80 steel. They used three types of oxide preparation methods: high-temperature oxidation (specimen 1#), blackening treatment (specimen 2#), and passivation in concentrated H_2SO_4 (specimen 3#). Through permeation experiments and slow strain rate tests (SSRTs), they assessed each sample's susceptibility to hydrogen embrittlement (HE) and analysed the oxide films' thickness, composition, and compactness via EDS analysis.

Although specimen 2# had the largest thickness, it also showed the poorest compactness. EDS analysis revealed that the blackened oxide film on specimen 2# was porous, with cracks and voids, unlike the denser films on specimens 1# and 3#. Consequently, despite its greater

thickness, the poor compactness of specimen 2# allowed for easier hydrogen diffusion, leading to higher permeability compared to the more compact oxide films.

Using permeation data and a hydrogen diffusion model, Zhang et al. calculated the hydrogen permeability ratio (ϕ_m/ϕ_f) between the steel substrate and the oxide film. As can be seen in figure 2.11, specimen 1# had the highest ϕ_m/ϕ_f value of 3828, indicating that the oxide film from high-temperature oxidation offered the strongest resistance to hydrogen permeation. In contrast, the thicker but porous oxide on specimen 2# had a much lower ϕ_m/ϕ_f value, highlighting that its lack of compactness reduced its effectiveness.

Surface conditions	Permeation current (μA cm^{-2})	Film thickness (μm)	ϕ_m/ϕ_f
0#	5.687	–	–
1#	1.178	1.00	3828
2#	4.946	3.11	48
3#	1.717	1.44	1606

Figure 2.11: Hydrogen permeation parameters of X80 steels with and without oxide films. Specimen 0# refers to the bare steel [72].

SSRTs further emphasized the importance of compactness. Figure 2.13 illustrates that specimen 1#, with its dense oxide layer, showed the lowest embrittlement index (F_H) of 4%, indicating low susceptibility to HE. In comparison, specimen 2#, with its thicker but porous oxide, had a higher embrittlement index of 11.68%, as cracks and pores created pathways for hydrogen ingress into the steel (refer to figure 2.12).

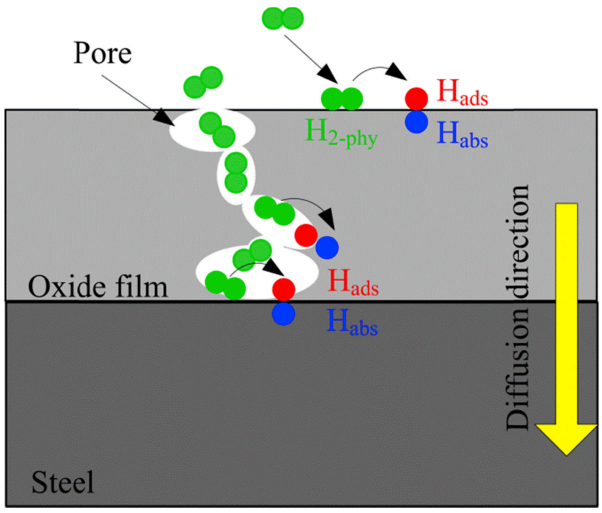

Figure 2.12: Schematic of hydrogen diffusion in a defect-containing oxide film-steel system [72].

It must be noted that reduction in cross-section was chosen as the relevant parameter as existing research indicates susceptibility to HE manifests as higher embrittlement index values [73]. F_H was calculated using the following equation:

$$F_H = (Z_A - Z_H)/Z_A \tag{2.3}$$

where Z_A and Z_H refer to the reduction in cross-section in air and gaseous hydrogen, respectively.

Specimen	Environment	Tensile strength (MPa)	Elongation (%)	Reduction of area (%)	HE index (%)
0#	Air	673 ± 7	21	76.34 ± 1.38	–
0#	1.2 MPa H_2	665 ± 8	16	47.28 ± 1.44	38.07 ± 2.15
1#	1.2 MPa H_2	655 ± 6	20	73.29 ± 1.53	4.00 ± 2.64
2#	1.2 MPa H_2	678 ± 7	19	67.42 ± 1.69	11.68 ± 2.66
3#	1.2 MPa H_2	660 ± 9	17	66.40 ± 1.55	13.02 ± 2.53
3#-dehydrogenation	1.2 MPa H_2	652 ± 8	20	72.11 ± 1.62	5.54 ± 2.70

Figure 2.13: Mechanical parameters of X80 steel with different surface conditions in air or high-pressure hydrogen gas [72].

These findings demonstrate that compactness, rather than thickness alone, is crucial to the oxide layer's effectiveness as a hydrogen permeation barrier.

In agreement with Zhang et al. [72], Zhou et al. [74] investigated the hydrogen permeability of oxide films formed on X52 pipeline steel in air at heat treatment temperatures of 300°C, 400°C, and 500°C. The findings highlighted that the compactness of the oxide films was the key factor influencing their ability to block hydrogen diffusion. Despite having the least thickness, the oxide films formed at 300°C were more compact and uniform, showing no visible defects and a dense structure that effectively hindered hydrogen permeation. As the oxidation temperature increased to 400°C and 500°C, the films became thicker but also more porous, with micropores and larger defects forming on the surface. This increase in porosity at higher temperatures reduced the films' protective capabilities, as these defects created pathways for hydrogen to penetrate. In contrast, the thinner but denser 300°C film offered the most effective hydrogen barrier. This finding reinforces Zhang et al. [72]'s conclusion that compactness, rather than thickness alone, determines the permeation resistance of oxide films.

Together, these studies highlight a consistent trend: while increasing thickness can theoretically enhance hydrogen resistance by lengthening the diffusion path, this benefit is contingent upon the compactness and structural integrity of the oxide layer. When oxide films are porous or contain defects, additional thickness may fail to improve, or even reduce, their effectiveness as a hydrogen barrier. This suggests that optimizing oxide films for hydrogen permeation resistance requires a balance between adequate thickness and high compactness, as compact and defect-free films provide more reliable protection against hydrogen diffusion.

Composition

The studies by Rubben et al. [65], Ishikawa et al. [71], and He et al. [75] collectively demonstrate the significant role of oxide layer composition in influencing hydrogen permeation resistance.

As discussed earlier, Rubben et al. [65] grew magnetite and bi-layered oxide films on the exit surface of SAE 1010 steel and studied their influence on hydrogen transport out of the steel using both electrochemical discharging and Scanning Kelvin Probe Force Microscopy (SKPFM) experiments. Chronoamperometric measurements illustrated in figure 2.14 compared the discharging current levels through both the oxide types of similar thickness. Compared to the blank samples, those with the magnetite layer and the bilayer reported a rapid drop in discharging current values initially, followed by a slower decline to the background current. Additionally, while both the layers were of similar thickness, the decline in discharging current values was significantly slower in the case of the bilayer. This would indicate that the hydrogen flow rate through the bilayer is lower than through to the magnetite layer. The authors attributed this to the presence of the more insulating outer haematite layer [7] and the possibility of hydrogen trapping at the magnetite/haematite interface.

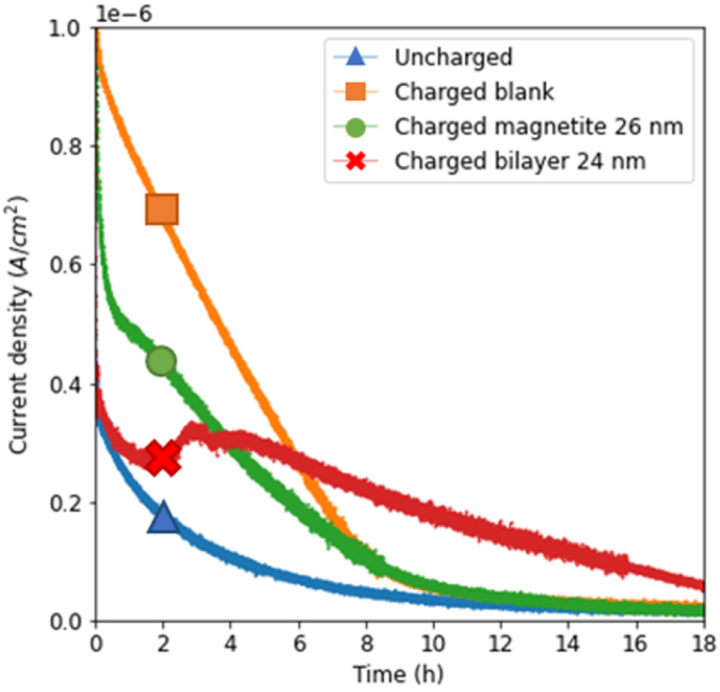

Figure 2.14: Chronoamperometric curve of the discharging step after 1.5 hours of charging, comparing specimens with a magnetite layer to those with a bilayer of comparable thickness [65].

In order to support the results obtained from the electrochemical discharging experiments, SKPFM was performed to investigate the hydrogen release rate into the Pd layer of all the specimens. Time-resolved potential maps were generated by scanning regions containing the bare and the oxide-covered steel, providing information on the influence of oxide layers on the hydrogen release rate into the Pd layer. The potential was calculated using the following formula:

$$E = E^{*}_{SHE} + (RT/F) \cdot ln(a(H^{+})/a(H_{ab})) \tag{2.4}$$

According to the above equation, a reduction in the potential would indicate a higher hydrogen content in the Pd layer and a higher release rate from the sample surface [76]. Figure 2.15 describes the average potential values versus time of the bare and the oxide-covered steel for both the oxide layers of 41 nm thickness. Both plots illustrated a potential reduction over time for all the specimens, indicating continuous release of hydrogen into the Pd layer. However, the potential decrease over time was lower for the oxide-covered specimens compared to the blank specimens, which was attributed to a reduced hydrogen flow rate through both oxide layers. Additionally, the specimen with the 41 nm bilayer oxide reported the lowest potential reduction over time, indicating that the bilayer was more effective at inhibiting hydrogen release into the Pd layer compared to the magnetite layer. Both these results were in agreement with those from the discharging experiments.

This study highlights that specific oxide compositions and layer arrangements can have a substantial impact on hydrogen barrier effectiveness, beyond simple thickness considerations.

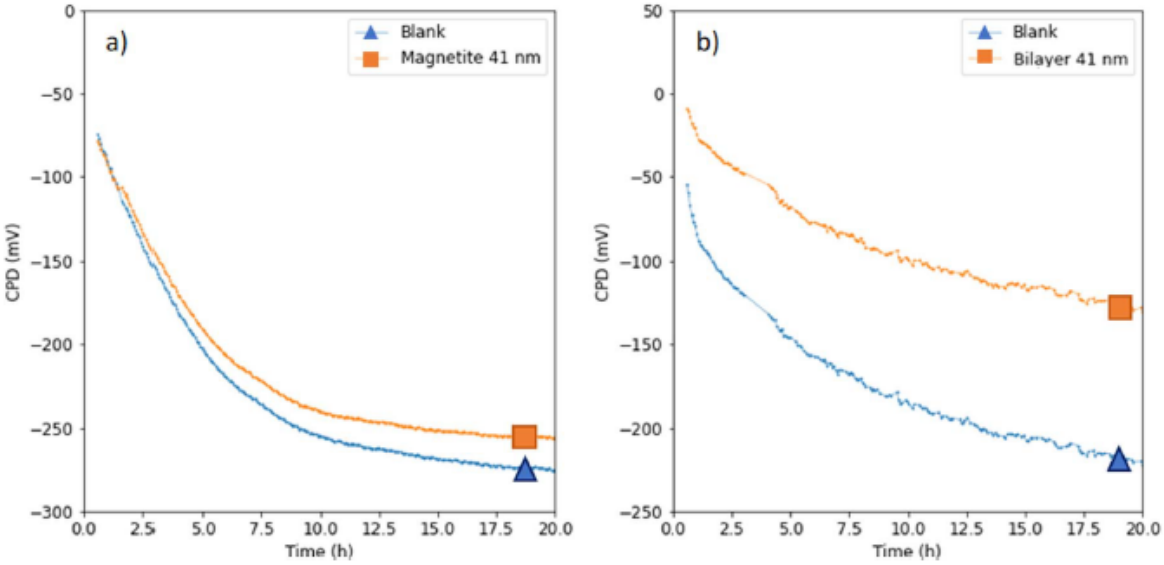

Figure 2.15: Evolution in time of the measured contact potential difference (CPD) (a) averaged over the bare steel and the magnetite 41 nm surface and (b) averaged over the bare steel and the bilayer 41 nm surface [65].

Similarly, Ishikawa et al. [71] reinforced the influence of oxide composition, examining the deuterium permeation behaviour of Cr-rich versus Fe-rich oxide layers formed on 316L stainless steel. The study demonstrated that Cr-rich oxides significantly lowered deuterium permeability and diffusion coefficients, with both metrics decreasing as the Cr/(Cr + Fe) ratio increased. This indicates that Cr-rich oxides form a more effective diffusion barrier compared to Fe-rich oxides, which showed minimal changes in permeability regardless of composition. These findings emphasize that enhancing the chromium content in the oxide layer is crucial for improving hydrogen barrier performance in stainless steel. This aligns with Rubben et al. [65]'s findings, emphasizing that particular oxide compositions—especially those rich in chromium—can form more effective hydrogen barriers due to their ability to create compact, dense oxide layers that minimize hydrogen diffusion pathways.

He et al. [75] further explored this influence of oxide composition on hydrogen permeation by examining the deuterium permeability of single-layered Al_2O_3 and Cr_2O_3 coatings on 316L stainless steel. The Cr_2O_3 film, with a thickness of approximately 156 nm, exhibited a lower reduction in deuterium permeability, with permeability reduction factor (PRF) values ranging from 24 to 117 at temperatures between 823 K and 973 K. In comparison, the Al_2O_3 coating, at a similar thickness of 174 nm, showed higher permeation resistance, with PRF values between 95 and 247 over the same temperature range. These findings suggest that despite both coatings being close in thickness, the amorphous Al_2O_3 film offered greater resistance to hydrogen permeation than the crystalline Cr_2O_3 layer, likely due to fewer diffusion pathways within the amorphous structure.

In addition to the single-layer coatings, He et al. [75] investigated a composite Al_2O_3/Cr_2O_3 structure with a combined thickness of approximately 330 nm. It is interesting to note that this composite coating demonstrated significantly enhanced deuterium permeation resistance compared to the individual layers. The composite's PRF values ranged from 211 to 496 across temperatures between 823 K and 973 K, outperforming both the single 174 nm Al_2O_3 layer (PRF: 95 to 247) and the 156 nm Cr_2O_3 layer (PRF: 24 to 117) over the same temperature range. The improved performance of the composite structure can be attributed to the synergistic effects of the layered Al_2O_3 and Cr_2O_3, which likely combine the diffusion resistance of the

amorphous Al_2O_3 with the durability and stability of the Cr_2O_3. This comparison underscores that while the Al_2O_3 layer alone provides greater permeability resistance than Cr_2O_3, the composite structure offers superior protection by leveraging the properties of both materials.

In summary, these studies collectively underscore that oxide layer composition, structure, and configuration are vital factors in controlling hydrogen permeation. While increasing oxide thickness is beneficial, the specific composition—such as the inclusion of chromium or the use of amorphous alumina—has a more pronounced effect on permeation resistance. Composite structures that combine complementary oxides, like the Al_2O_3/Cr_2O_3 composite, offer further improvements by utilizing the unique properties of each material. Thus, optimizing hydrogen barriers requires careful consideration of both oxide composition and structural arrangement, which can significantly enhance their effectiveness beyond thickness alone.

Crystallinity

Limited information exists on the role of crystallinity across different oxide coatings and its effect on hydrogen permeability. In this context, we explore the case of alumina to understand how crystallinity impacts hydrogen permeation behaviour and the integrity of underlying substrates.

Specific crystalline forms of alumina, such as α-Al_2O_3, have demonstrated better resistance to hydrogen permeability than amorphous forms, as reported by Xiao et al. [77]. α-Al_2O_3 is particularly stable at high temperatures and exhibits the lowest hydrogen permeability among alumina phases [78]. However, achieving this stable phase requires annealing at temperatures as high as 1473 K, which can introduce thermal stresses, pores, and cracks in sensitive substrates like stainless steel. This temperature constraint poses a challenge for practical applications on substrates prone to thermal damage, as the formation process of α-Al_2O_3 may compromise substrate integrity.

He et al. [79] further confirmed these concerns regarding substrate damage when studying the effect of crystallinity on hydrogen permeability in alumina coatings on 316L stainless steel. They found that coatings annealed at 700°C remained amorphous and exhibited lower hydrogen permeability, while those annealed at 900°C developed crystalline phases, including γ-alumina and $MnCr_2O_4$ spinel, which increased permeability. The crystalline structure created diffusion “short-cuts” for hydrogen and led to delamination during testing, which further compromised the barrier and exposed the substrate to potential damage. These findings confirmed that, as suggested by Xiao et al., high temperatures required for crystallinity can introduce mechanical vulnerabilities to the substrate, making amorphous alumina coatings a preferred choice for sensitive materials like stainless steel.

Similarly, Levchuk et al. [78] investigated the hydrogen permeability of alumina coatings on Pd–Ag substrates, reaching conclusions that support the findings of both He et al. [79] and Xiao et al. [77]. They found that amorphous alumina coatings, formed at lower temperatures, provided significantly higher resistance to hydrogen permeation compared to coatings with mixed crystalline and amorphous structures. Crystalline regions, especially those containing γ-alumina, introduced grain boundaries and diffusion pathways that facilitated hydrogen transport. In contrast, the uniform structure of amorphous alumina restricted these pathways, resulting in reduced permeability and improved barrier effectiveness. This study on Pd–Ag substrates reinforces the conclusion that amorphous alumina structures, formed at lower temperatures, enhance hydrogen resistance and avoid the substrate damage seen with crystalline alumina coatings.

In summary, the case of alumina demonstrates that crystallinity plays a crucial role in deter-

mining hydrogen permeability, impacting both the barrier effectiveness and the integrity of the underlying substrate. While certain crystalline forms, such as α-Al_2O_3, offer excellent permeability resistance, their high-temperature formation can introduce mechanical stress and damage to sensitive substrates like stainless steel. Studies by He et al. [79] and Levchuk et al. [78] confirm that amorphous alumina, which forms at lower temperatures, provides superior resistance to hydrogen permeation by limiting diffusion pathways without compromising substrate stability. Together, these findings underscore the importance of carefully selecting coating crystallinity based on substrate compatibility and operating conditions, with amorphous alumina emerging as a favourable choice for applications requiring both effective hydrogen barriers and substrate protection.

2.2.2. Overview and Relevance of Oxide Layer Characteristics

In conclusion, the key characteristics of oxide layers — thickness, compactness, composition, and crystallinity — collectively influence hydrogen permeation resistance, though they impact it in distinct ways. While increasing thickness generally enhances resistance by extending the diffusion pathway, its benefits are limited if the oxide layer lacks compactness or structural integrity, as demonstrated across several studies. Compactness emerges as especially critical, as denser layers with fewer defects consistently show lower hydrogen permeability, even at thinner dimensions. Composition and crystallinity further refine the layer's protective capabilities; for instance, Cr-rich compositions and amorphous structures often provide greater resistance to hydrogen diffusion by creating fewer diffusion pathways. Among these parameters, compactness is perhaps the most crucial, given its direct role in blocking hydrogen ingress. However, a balanced optimization of compactness with composition and crystallinity is essential to design oxide layers that offer robust hydrogen permeation resistance across varied applications.

2.3. Evaluation of Hydrogen Permeation - Experimental Techniques

Experimental techniques for investigating hydrogen permeation encompass a range of methods that enable precise measurement of hydrogen diffusion rates, barrier properties, and material interactions under controlled conditions. Commonly used techniques include Thermal Desorption Spectroscopy (TDS), which analyses hydrogen release upon heating; Electrochemical Impedance Spectroscopy (EIS), which assesses material impedance to hydrogen ion migration; Hydrogen Microprint Technique (HMT), a visualization method for tracking hydrogen diffusion pathways; and the Devanathan-Stachurski (DS) cell, a widely used setup for electrochemical measurement of hydrogen permeation across a membrane. This section reviews these techniques, highlighting their principles, strengths, and applications in evaluating hydrogen permeation behaviour in materials.

2.3.1. Thermal Desorption Spectroscopy (TDS)

Thermal desorption spectroscopy is a technique used to analyse hydrogen content in materials by gradually heating a hydrogen-charged sample and monitoring the release of hydrogen as a function of temperature. A typical TDS set-up is illustrated in figure This method enables the identification and quantification of different types of hydrogen traps within the material based on the temperature at which hydrogen is released. By correlating the desorption peaks to specific traps, TDS provides insights into the binding energies and the nature of hydrogen interactions within the material's microstructure.

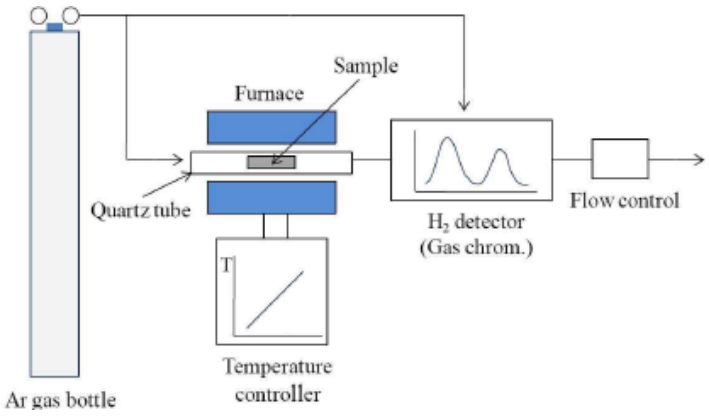

Figure 2.16: Typical setup for thermal desorption spectroscopy (TDS) [80].

TDS has been effectively applied in various studies to investigate hydrogen permeation behaviour in steel. For instance, Zheng et al. [81] used TDS to study X80 pipeline steel, identifying shallow and deep hydrogen traps with binding energies of 13.5 ± 0.2 kJ/mol and 47.1 ± 0.2 kJ/mol. Their analysis involved electrochemical hydrogen charging, followed by TDS at heating rates of 100, 150, 200, and 250 °C/h. They analysed the desorption peaks using Choo-Lee's method [82] to calculate activation energies and differentiate traps based on hydrogen retention.

Xu et al. [83] applied TDS to measure hydrogen desorption in X52 pipeline steel, charging the samples at 2 MPa partial pressure for 12 hours. Using a heating rate of 100 °C/h from 30 °C to 700 °C, they observed that higher charging temperatures (up to 60 °C) increased hydrogen trapping, as indicated by elevated desorption peaks. Zhao et al. [84] investigated hydrogen permeation in QP1180 steel using TDS, heating samples to 800 °C at a rate of 350 °C/h in an argon atmosphere to evaluate hydrogen trapping behaviour.

In spite of its limitations, TDS remains a valuable tool for studying hydrogen content and trapping behaviour in steels. However, to overcome the challenges of spatial resolution, surface interference, and incomplete detection of deeply trapped hydrogen, TDS should be used in conjunction with other complementary techniques. Methods such as atom probe tomography (APT) or transmission electron microscopy (TEM) can provide spatial insights, while electrochemical permeation testing may offer additional data on hydrogen transport through the material. By combining TDS with these techniques, a more comprehensive understanding of hydrogen permeation and trapping in steels can be gained, allowing for more accurate assessments of hydrogen-induced material degradation.

2.3.2. Hydrogen Microprint Technique (HMT)

Also known as the silver decoration technique, the hydrogen microprint technique (HMT) is used to visualize hydrogen diffusion and trapping at the microscopic level [85]. Developed by Ovejero-Garcia [86], the procedure involves charging polished steel with hydrogen, applying a silver bromide (AgBr) emulsion, and allowing hydrogen to evolve from the steel surface. The hydrogen atoms react with silver ions (Ag^{+}), reducing them to metallic silver (Ag^{0}), which forms visible silver particles under a microscope. After exposure, photographic fixing removes unreacted AgBr crystals, leaving behind silver particles that map where hydrogen exited the surface. The step-by-step process of HMT is illustrated in figure 2.17.

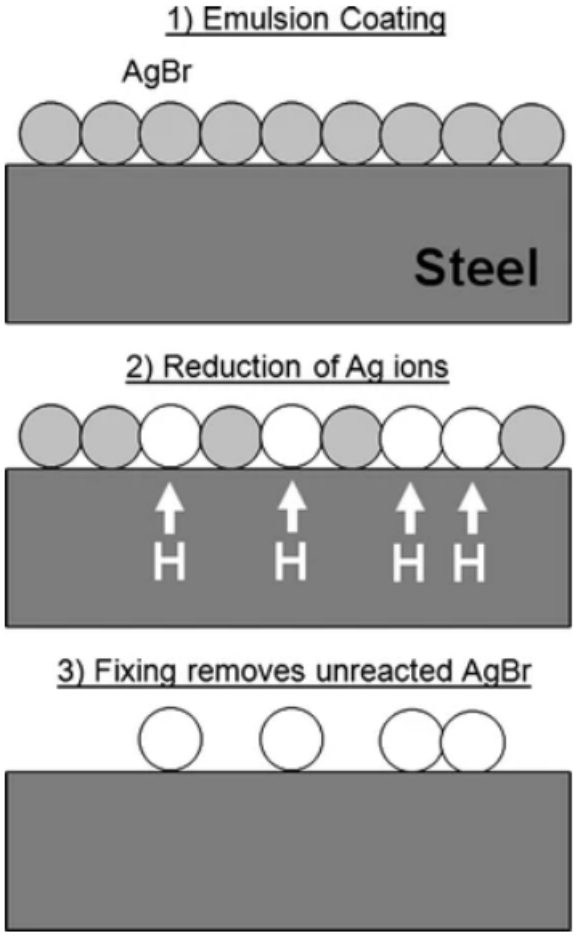

Figure 2.17: Schematic of HMT. (1) AgBr emulsion is coated on polished steel. (2) As H atoms evolve out of steel, reduction of Ag^{+} to Ag occurs on surface. (3) Fixing removes unreacted AgBr crystals and reveals Ag grains where H evolved from surface [85].

The key reaction involved is:

$$AgBr + \frac{1}{2}H_2 \rightarrow Ag^0 + H^+ + Br^- \quad (7)$$

These silver particles indicate the locations and density of hydrogen activity, providing spatial information about hydrogen diffusion and trapping sites within the material.

HMT is particularly effective for visualizing hydrogen pathways and identifying trapping sites at the microstructural level. Thomas and Szpunar [87] utilized HMT to study hydrogen diffusion in X70 pipeline steel, showing that hydrogen mainly diffused through grain boundaries, triple junctions, and cementite phases, which acted as reversible traps. These microstructural features served as key pathways, with higher hydrogen concentrations observed compared to grain interiors.

In the study by Ichitani and Kanno [88], high sensitivity HMT was employed to investigate hydrogen diffusion in low-carbon and hypo-eutectoid steels. This advanced version of conventional HMT, with a spatial resolution of 0.1 µm, allowed detailed visualization of hydrogen diffusion paths. The findings revealed that hydrogen predominantly diffuses through grain boundaries, proeutectoid ferrite, ferrite in pearlite, and along carbide/ferrite interfaces, where reversible hydrogen trapping occurs. The technique demonstrated significantly higher detection efficiency than conventional HMT, with 75% efficiency for low-carbon steel and 40% for hypo-eutectoid steel, providing clearer insights into hydrogen diffusion mechanisms.

Building on these findings, Matsuda et al. [89] applied high sensitivity HMT to a wider range of steels, including tempered martensitic steel. This study confirmed the earlier results, showing that hydrogen diffuses through the crystal lattice in low-carbon steel and through proeutectoid ferrite in hypoeutectoid steel. Additionally, it revealed that in tempered martensitic steel, hydrogen diffusion occurs primarily along martensitic lath interfaces. These findings further demonstrated high sensitivity HMT's ability to capture subtle hydrogen diffusion patterns across various microstructures, reinforcing its value in studying hydrogen trapping mechanisms in steels.

Despite its limitations, HMT remains valuable for visualizing hydrogen pathways, especially in simpler microstructures. Combined with techniques like TDS, which quantifies hydrogen content, EIS, which analyses hydrogen permeation, and electrochemical permeation testing to measure diffusion rates, HMT provides a more complete understanding of hydrogen behaviour. These methods complement HMT by offering subsurface insights and quantitative data.

2.3.3. Electrochemical Impedance Spectroscopy (EIS)

Electrochemical impedance spectroscopy (EIS) is a non-destructive technique that provides detailed information about hydrogen permeation and trapping by analysing the impedance response of materials to an applied alternating current (AC) signal. In hydrogen permeation studies, EIS monitors changes in the material's electrochemical behaviour as it absorbs and diffuses hydrogen, measuring impedance at the metal-electrolyte interface. These measurements enable the assessment of hydrogen uptake, diffusion rates, and interactions with microstructural features like grain boundaries. Additionally, EIS is effective in evaluating the barrier properties of surface layers, such as oxide films, by detecting how these layers impede hydrogen diffusion and affect overall impedance. This is achieved by analysing changes in resistance and capacitance across different frequencies. Its sensitivity to various electrochemical phenomena makes EIS a powerful tool for evaluating hydrogen-induced degradation and embrittlement in pipeline steels [90].

Peng and Cheng [91] applied EIS to investigate the hydrogen-induced corrosion behaviour of X65 and X80 pipeline steels. Their study measured the impedance of these steels in a near-neutral pH solution (NS4), which consisted of 0.483 g/L $NaHCO_3$, 0.122 g/L KCl, 0.181 g/L $CaCl_2{\cdot}H_2O$, and 0.131 g/L $MgSO_4{\cdot}7H_2O$, after hydrogen charging. The results demonstrated that hydrogen charging reduced the charge-transfer resistance, thereby enhancing corrosion in both materials. Despite this overall increase in corrosion, X80 steel showed better corrosion resistance compared to X65 steel, which was attributed to its finer grain structure and the presence of bainitic ferrite. This suggests that, although X80 steel's higher strength may increase its susceptibility to HIC, it demonstrates superior resistance to corrosion when exposed to hydrogen.

In the study by Zeng et al. [92], EIS was used to evaluate the hydrogen interaction characteristics of oxide films formed on stainless steel at 450 °C and 750 °C. EIS measurements showed that hydrogen exposure reduced the impedance of both films by about 60%, indicating diminished protection. The 450 °C films, with dense chromia and $FeCr_2O_4$ layers, displayed better hydrogen resistance and a higher phase angle at low frequencies. In contrast, the 750 °C films had more surface defects and lower impedance, reflecting weaker hydrogen protection.

Equivalent circuit analysis further highlighted the 450 °C films' superior resistance, increasing from 32.5 kΩ to 46.8 kΩ after hydrogen annealing, while the 750 °C films showed much lower resistance. Complementary techniques like XPS and AES confirmed these findings, supporting the conclusion that 450 °C oxide layers were more effective at preventing hydrogen permeation.

Given its limitations, EIS is often complemented by other techniques to provide a more comprehensive understanding of hydrogen permeation and trapping. While EIS excels at detecting changes in impedance and electrochemical phenomena, it cannot directly measure hydrogen concentrations or pinpoint the exact locations where hydrogen is trapped. Techniques such as TDS offer precise quantitative data on hydrogen trap densities and binding energies, while HMT helps to visualize hydrogen interactions with microstructural features. Additionally, electrochemical permeation testing can give a more direct measure of hydrogen diffusion rates across a material, offering insights that EIS can only infer indirectly.

2.3.4. Electrochemical Devanathan-Stachurski (DS) Method

The Devanathan-Stachurski (DS) method is a standard electrochemical technique for studying hydrogen permeation in materials. This technique utilizes a dual-electrochemical cell setup, where hydrogen is introduced on one side of a metallic membrane through electrochemical charging (charging side), while the permeated hydrogen is detected on the opposite side (detection side) as it oxidizes, producing a measurable current. This current is proportional to the hydrogen flux, enabling the calculation of key parameters such as the hydrogen diffusion coefficient, permeation rates, and breakthrough times. Figure 2.18 illustrates a typical DS double cell setup. The hydrogen diffusion coefficient can be calculated with the following equations [93]:

$$D = \frac{d}{15.3t_b^2} \tag{2.5}$$

$$D = \frac{d}{6t_{0.63}^2} \tag{2.6}$$

where D is the hydrogen diffusion coefficient in m^2/s; d is the sample thickness in meters; t_b is the transferring time (the time corresponding to the intersection of the tangent line at the inflection point and the horizontal axis in the permeation curve) in seconds; and $t_{0.63}$ is the retardation time (the time when the permeation current reaches 0.63 times the steady-state current value) in seconds. The principle of the electrochemical measurement and the parameters mentioned above in analysing the electrochemical hydrogen permeation current curves are described in figure 2.19. The DS method is particularly useful for evaluating the material's resistance to hydrogen permeation and provides real-time, quantitative data on hydrogen permeation behaviour.

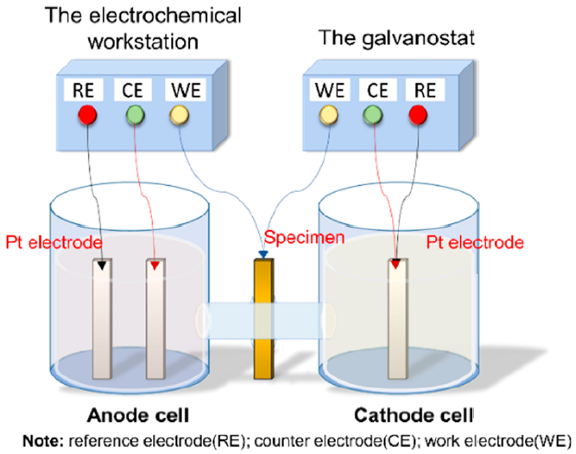

Figure 2.18: Schematic of a typical DS permeation cell [94].

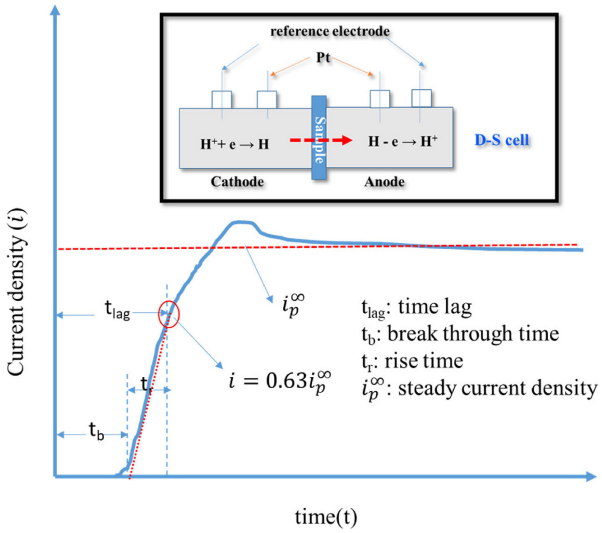

Figure 2.19: Schematic working principle of the DS cell (top) and the illustration of electrochemical hydrogen permeation current curve (bottom) [95].

Mechanism of Hydrogen Permeation

In the case of electrochemical hydrogen charging, the charging cell is cathodically polarized in order to generate atomic hydrogen on the entry surface of the steel membrane. This is achieved via the Volmer reaction (1) [65, 96, 97]:

$$H_2O + e^- \rightarrow H_{ads} + OH^- \tag{1}$$

Post-hydrogen adsorption, the Tafel (2) and Heyrovsky (3) desorption reactions take place in parallel with the hydrogen absorption reaction (4), which introduces atomic hydrogen into the bulk of the steel membrane [65, 96, 97]:

$$2H_{ads} \rightarrow H_2(gas) \tag{2}$$

$$H_{ads} + H_2O + e^- \rightarrow H_2(gas) + OH^- \tag{3}$$

$$H_{ads} \rightarrow H_{abs} \tag{4}$$

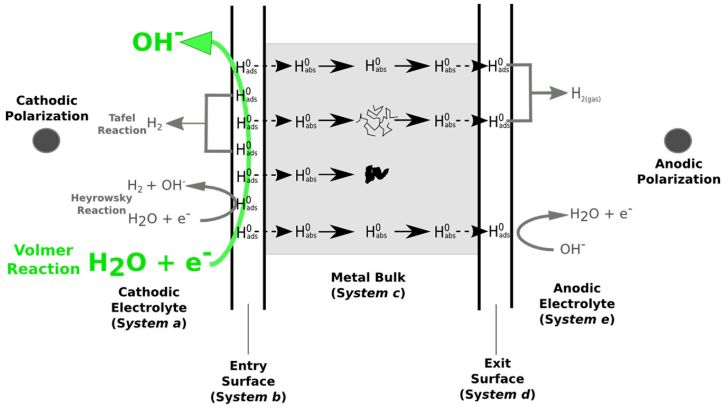

Figure 2.20: A detailed summary of the hydrogen diffusion process in the DS cell [97].

However, this mechanism does not take into account the presence of an oxide layer on the charging or detection side and how it may influence hydrogen permeation behaviour.

Vecchi et al. [97] utilized finite element modelling in order to gain a better understanding of the impact of an oxide layer on the detection side of a permeation cell. The research proposed two distinct diffusion mechanisms for hydrogen through the oxide layer on the detection side. As can be seen in figure 2.21, model 1 assumed simple atomic hydrogen diffusion through the oxide layer, showing a substantial delay in hydrogen permeation due to very low diffusion coefficients typical of oxides. As can be seen in figure 2.22, model 2 considers hydrogen diffusion as protons (or partially charged particles), facilitated by an electric field through the oxide layer. This model suggests that while the diffusion might still be impeded, the presence of an electric field can enhance the diffusion rates compared to simple atomic diffusion. However, the authors mentioned that both mechanisms did not accurately represent the experimental results commonly obtained. As a result, an alternative mechanism was proposed in the research, which can be seen in figure 2.23. This mechanism considers the partial reduction of the oxide layer at the exit side due to hydrogen atoms and the subsequent re-oxidation due to the anodic polarization imposed. As a result, a circular mechanism of iron reduction/re-oxidation is established.

While these proposed mechanisms provide a suitable starting point for understanding hydrogen diffusion within the oxide layer on the detection side, further investigation is needed to confirm these processes, particularly with the addition of a Pd layer at the detection side and an oxide layer at the entry side. It can be hypothesized that the underlying mechanism would not change in the presence of an oxide layer; rather, the oxide layer would primarily influence the amount of atomic hydrogen permeating into the steel membrane by acting as a barrier or modifying the entry flux. However, potential variations in the hydrogen diffusion mechanism due to the presence of an oxide layer on the entry surface have not been confirmed, highlighting the need for more comprehensive studies to fully elucidate the influence of oxide layers on both sides of the membrane.

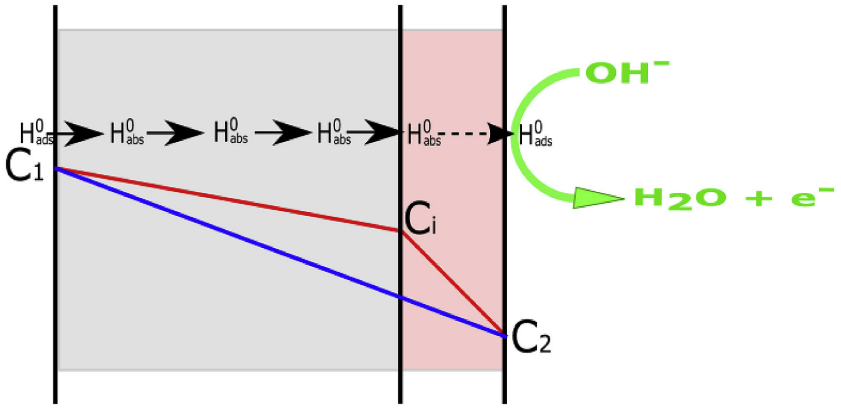

Figure 2.21: Case with H^0 diffusion in the oxide layer. In red, the concentration of hydrogen in each subsystem is presented. In blue the average concentration gradient effectively measured in the Devanathan-Stachurski cell [97].

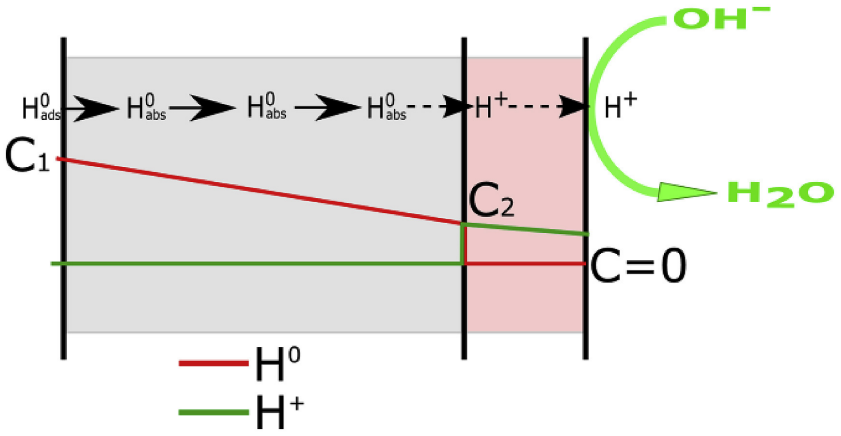

Figure 2.22: Case with hydrogen proton (H^+) diffusion in the oxide layer. The electron exchange takes place underneath the oxide layer [97].

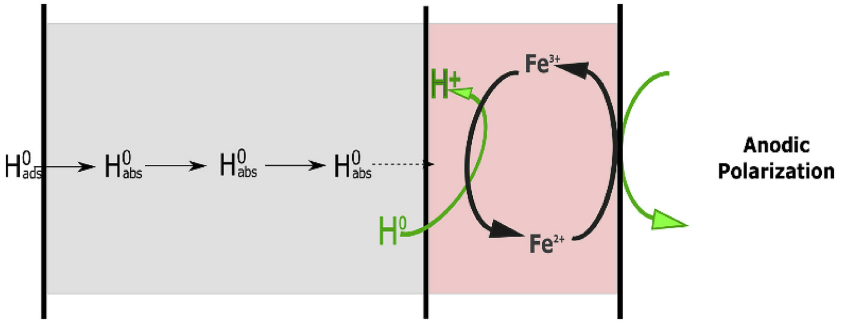

Figure 2.23: Proposed mechanism taking place at the oxide layer [97].

While the DS setup is effective for assessing hydrogen diffusion, concentration, and trapping in steel membranes, it has notable limitations. Factors such as sample roughness, electrolyte composition, and current density can impact hydrogen entry flux and uptake, leading to inconsistencies. Additionally, the setup does not fully simulate in-situ gaseous conditions. Liu et al. [98] and Koren et al. [99, 100] showed that equivalence between electrochemical and

gaseous charging can be achieved by matching hydrogen fugacity, enabling realistic comparisons. Oxide layers, whether naturally formed or developed during anodic polarization, pose significant challenges by altering boundary conditions, impeding hydrogen entry, and affecting permeation flux. While Pd coatings are commonly used to mitigate surface issues and stabilize measurements, underlying oxide layers can still influence results, as shown by Ma et al. [101]. Techniques such as argon plasma sputtering to remove these oxide layers have been shown to restore stable and accurate hydrogen permeation currents. Careful control of surface preparation and experimental parameters is essential for reliable and reproducible hydrogen permeation studies.

2.3.5. Gas-Phase Permeation Techniques

In addition to electrochemical permeation techniques, Li et al. [94] discussed the gas-phase permeation technique, which is a standard approach for evaluating hydrogen permeation through barrier coatings and base materials. This technique involves measuring hydrogen transfer across a membrane under a differential pressure, with hydrogen diffusing from a high-pressure side to a low-pressure vacuum side. Figure 2.24 illustrates the overall structure and working principle of this permeation setup. The hydrogen permeating through the membrane is measured using a quadrupole mass spectrometer (QMS).

To avoid the influence of hydrogen molecules in the gas-collecting chamber during the detection of permeable hydrogen by the mass spectrometer, deuterium gas is often used as the gas source [102, 103]. Both pressure and temperature can be well controlled in this method.

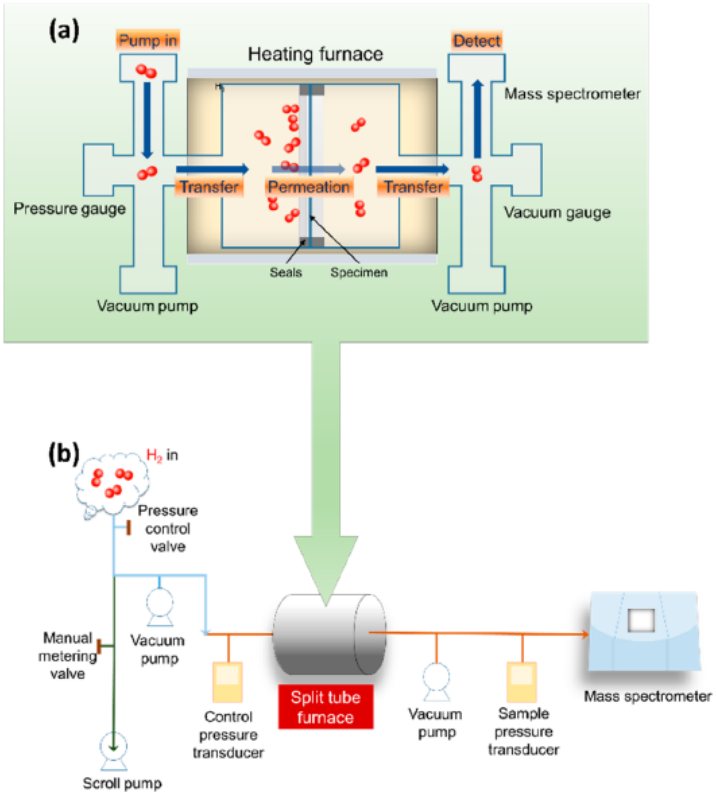

Figure 2.24: Working principle of hydrogen permeation testing apparatus with (a) hydrogen permeation chamber and (b) the hydrogen testing process diagram [94].

The method is essential for assessing the permeability and calculating the permeation reduc-

tion factor (PRF) of coatings. The permeability can be calculated using the following formula [93, 79]:

$$P_m = \frac{J \cdot d}{P^n} \tag{2.7}$$

where P_m is the hydrogen permeability in mol$/(\mathrm{m}\cdot\mathrm{s}\cdot\mathrm{Pa}^n)$, J is the hydrogen flux in mol$/(\mathrm{m}^2\cdot\mathrm{s})$, d is the thickness of the membrane in meters (m), and P is the gaseous hydrogen source pressure in pascals (Pa), with n being the pressure exponent. Hydrogen diffusion is the rate-limiting process for permeation when the pressure exponent n is 0.5, while a pressure exponent n of 1 indicates that the surface process limits the rate.

PRF is then typically calculated using the following formula [93, 104, 105]:

$$\mathrm{PRF} = \frac{P_{m,\mathrm{uncoated}}}{P_{m,\mathrm{coated}}} \tag{2.8}$$

where PRF is the permeation reduction factor, $P_{m,\mathrm{uncoated}}$ and $P_{m,\mathrm{coated}}$ are the hydrogen permeabilities of the uncoated and coated membranes, respectively, expressed as the number of hydrogen molecules per unit area and per unit time, in mol$/(\mathrm{m}\cdot\mathrm{s}\cdot\mathrm{Pa}^n)$.

PRF can also be calculated using the hydrogen permeation flux [104]:

$$\mathrm{PRF} = \frac{J_{\mathrm{uncoated}}}{J_{\mathrm{coated}}} \tag{2.9}$$

where J_{uncoated} and J_{coated} are the hydrogen permeation fluxes of the uncoated and coated membranes, respectively, expressed in mol$/(\mathrm{m}^2\cdot\mathrm{s})$.

He et al. [79] used the gas-phase permeation technique to investigate the rate-limiting step in deuterium permeation through alumina coatings. Their study highlighted how the pressure exponent n varied with temperature to indicate the controlling process of permeation, as can be seen in figure 2.25. For the 700°C annealed coating, n values between 0.75 and 0.78 suggested that both surface processes and hydrogen diffusion influenced the permeation rate. In contrast, the 900°C annealed coating showed a decrease in n from 0.71 at 600°C to 0.52 at 650°C, indicating a transition to a diffusion-limited regime. This change pointed to structural damage or microstructural changes in the 900°C coating that affected its hydrogen permeability, which was confirmed by SEM analysis of the coating surface.

In addition to gas-phase permeation methods using mass spectrometry, a modified version of the traditional DS setup can be used for hydrogen permeation studies. As can be seen in figure 2.26, this adaptation involves replacing the typical hydrogen charging side with an autoclave that holds high-pressure hydrogen at varying levels [106]. The measurement side employs a three-electrode system within a cell containing 0.1 M NaOH solution. This modification allows for hydrogen permeation testing under high-pressure gaseous conditions, providing a more realistic simulation of actual environments compared to the conventional liquid-phase charging in standard DS setups.

Figure 2.27 illustrates the hydrogen diffusion process in gaseous media, which closely resembles that of aqueous hydrogen diffusion. This process unfolds as follows [96, 107, 108, 109]:

The initial stage begins when gaseous hydrogen comes into contact with the metal surface, resulting in physiosorption. During this phase, no chemical bonds are formed between the

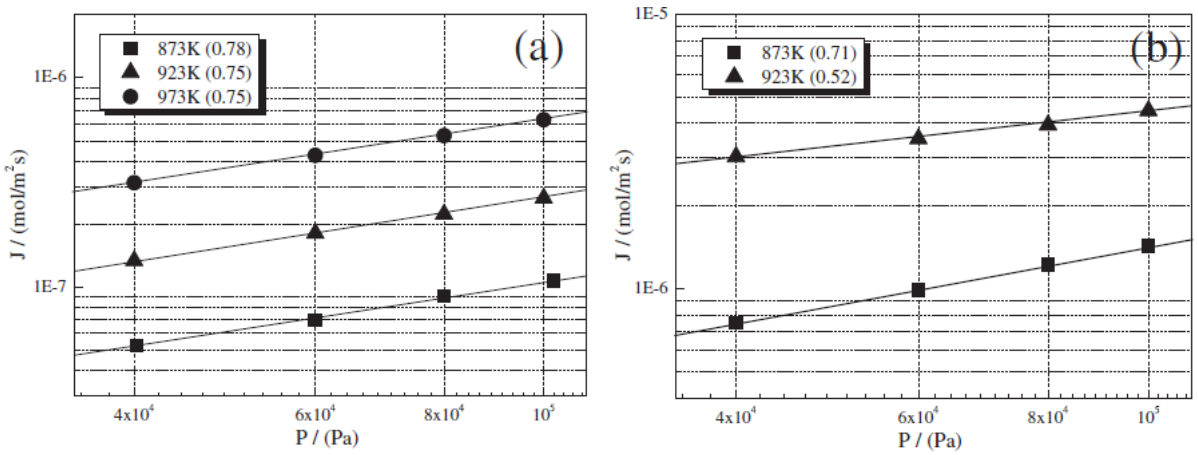

Figure 2.25: Steady state hydrogen permeation flux as a function of pressure at different temperatures: (a) 700°C annealed coating; (b) 900°C annealed coating. Number in parentheses represents the pressure exponent n [79].

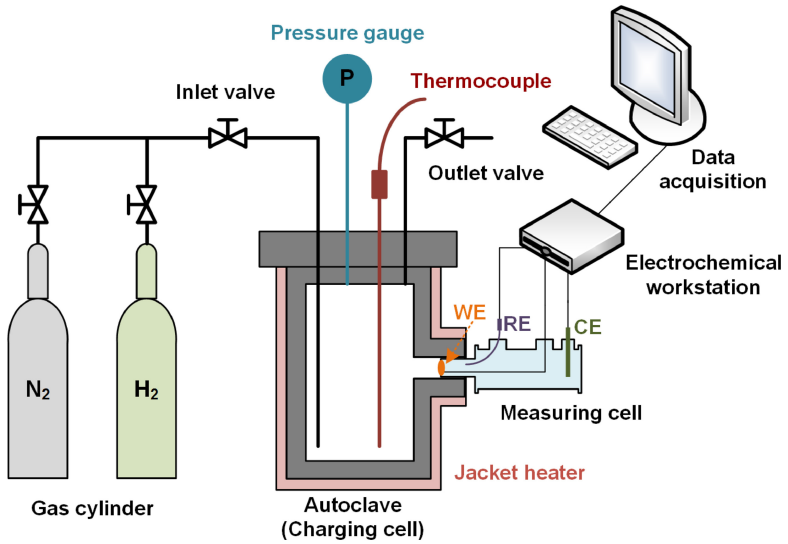

Figure 2.26: Schematic of a high-pressure gaseous hydrogen permeation test system [106].

hydrogen and metal, making it a weaker form of adsorption. Hence, the adsorption process is reversible.

$$H_2 + M \rightarrow H_2M \tag{2.10}$$

Following physiosorption, the H_2M and the metal surface form chemical bonds, marking an irreversible chemisorption process.

$$H_2M + M \rightarrow 2MH_{ad} \tag{2.11}$$

Subsequent to the chemisorption phase, the adsorbed hydrogen (MH_{ad}) is absorbed into the subsurface of the metal, resulting in the formation of absorbed hydrogen (MH_{ab}).

$$MH_{ad} \leftrightarrow MH_{ab} \tag{2.12}$$

Simultaneously, the adsorbed hydrogen can also recombine to generate molecular hydrogen (H_2).

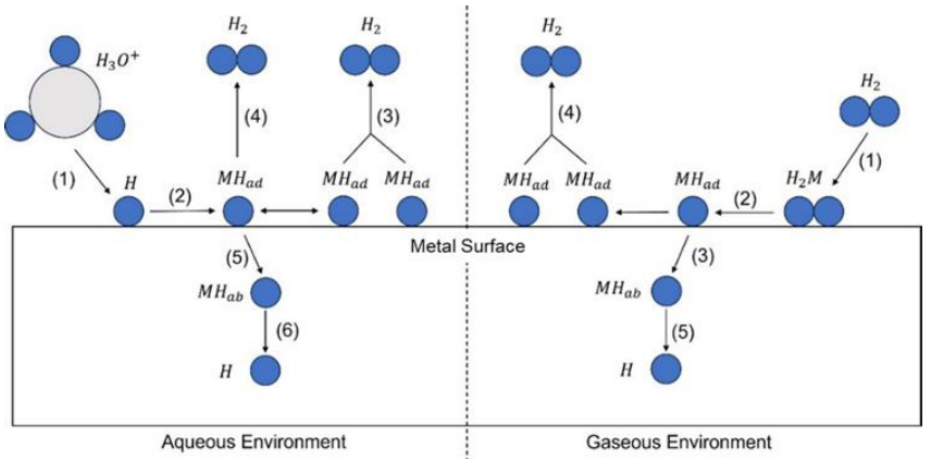

Figure 2.27: Possible ways of hydrogen transport and interaction in steel [109].

$$2M\mathrm{H}_{\mathrm{ad}} \rightarrow 2M + \mathrm{H}_2 \tag{2.13}$$

The absorbed hydrogen ($M\mathrm{H}_{\mathrm{ab}}$) undergoes a desorption process, transforming into atomic hydrogen dissolved within the metal.

$$M\mathrm{H}_{\mathrm{ab}} \rightarrow M + H \tag{2.14}$$

While gaseous hydrogen charging offers improved simulation of in-situ service conditions, the presence of surface oxide layers significantly impacts the reliability of permeation measurements at lower gas pressures and experimental temperatures. These oxide layers, whether naturally formed or applied, can obstruct hydrogen entry by inhibiting surface dissociation and reducing hydrogen flux. Research has demonstrated that even thin oxide films, such as those a few nanometres thick, can drastically impede hydrogen permeation, especially at low gas pressures and room temperature. Strategies such as applying Pd coatings to the entry side have been shown to mitigate these effects by facilitating hydrogen dissociation and improving flux consistency. Ensuring stable surface conditions and addressing the challenges posed by oxide layers are critical for obtaining accurate and reliable gas-phase permeation data.

To summarize, this section on experimental techniques provides an overview of methods used to evaluate hydrogen permeation and interaction within steel, each offering unique insights. Techniques like Thermal Desorption Spectroscopy (TDS) analyse hydrogen trapping by tracking hydrogen release, while Electrochemical Impedance Spectroscopy (EIS) assesses hydrogen ion migration and the effectiveness of surface layers. The Hydrogen Microprint Technique (HMT) visually maps hydrogen pathways, offering qualitative distribution data, and the Devanathan-Stachurski (DS) cell allows real-time monitoring of hydrogen diffusion through a membrane. Gas-phase permeation setups, which simulate in-situ conditions, measure hydrogen flow under differential pressure. Together, these methods underscore the need for a multi-technique approach to comprehensively understand hydrogen permeation behaviour in steel, especially in the presence of oxide barriers.

2.4. Summary of Literature

Steel surfaces tend to form various types of surface oxide layers based on the exposure conditions. The initial portion of this literature review extensively addressed the formation and characteristics of these oxide layers on steel surfaces, such as native, corrosion-induced, and high-temperature oxide layers. Key factors influencing these oxide layers include environmental exposure, temperature, alloying elements, and mechanical processing. The oxide layer's structure and properties vary significantly depending on these conditions, subsequently affecting its hydrogen permeation behaviour. For instance, different compositions and thicknesses result from factors like alloy composition and processing history, each impacting the steel's resistance to hydrogen ingress in specific ways. This literature review then examines key factors influencing hydrogen permeation behaviour in oxide layers on steel substrates, particularly those relevant for hydrogen transportation applications. As the transition towards renewable energy sources intensifies, so does the need for materials capable of safely transporting hydrogen. Pipeline steels, such as X65, serve as essential infrastructure for this purpose, yet face challenges related to hydrogen embrittlement (HE). This study has identified and analysed various factors that can either mitigate or exacerbate hydrogen permeation in oxide-coated steels.

One primary insight is the role of oxide layer characteristics—including thickness, composition, crystallinity, and compactness—in controlling hydrogen permeation. Thicker oxide layers can theoretically improve resistance by extending the diffusion path; however, this benefit is limited by the layer's compactness and structural integrity. If the oxide is porous or contains defects, increased thickness may paradoxically reduce its effectiveness as a barrier. Composition also plays a significant role; Cr-rich oxides, for instance, were observed to provide stronger permeation resistance than Fe-rich oxides, primarily due to their inherent density and stability.

This review also evaluated experimental techniques such as Thermal Desorption Spectroscopy (TDS), Electrochemical Impedance Spectroscopy (EIS), and the Devanathan-Stachurski (DS) cell, analysing each technique's capability to measure hydrogen permeation accurately. Results from these experiments emphasized that oxide structure and surface conditions must remain stable to obtain consistent permeation measurements. A comprehensive evaluation of hydrogen permeation resistance, however, requires a combination of techniques to capture the full range of hydrogen interactions with the oxide layers and underlying steel.

In summary, this literature review highlights that achieving optimal hydrogen permeation resistance in steel depends on a combination of key oxide layer parameters, including thickness, compactness, crystallinity, and chemical composition. Compactness was identified as the most critical parameter, followed by both thickness and chemical composition. Identifying these critical characteristics allows for a better understanding of how oxide layers can naturally mitigate hydrogen ingress in pipeline steels. By focusing on these parameters, it becomes possible to enhance the durability and safety of hydrogen transport infrastructure, supporting the broader goals of energy sustainability and infrastructure reliability.

2.5. Thesis Focus and Research Approach

The present study aims to investigate the characteristics of surface oxide layers formed on X65 pipeline steel and compare their hydrogen permeation behaviour with respect to steel without oxide layers. This comparison seeks to identify the key characteristics of the oxide layer that influence the hydrogen permeation behaviour. Additionally, the influence of the selected hydrogen charging method on the characteristics of both the oxide layer and the bare steel is investigated. The main research questions for this thesis are therefore as follows:

- **Research Question 1**: *What are the characteristics of the surface oxide layer present on X65 steel?*
- **Research Question 2**: *How does the surface oxide layer present on X65 steel influence its hydrogen permeation behaviour with respect to the bare steel?*
- **Research Question 3**: *What is the influence of hydrogen charging on the electrochemical response of both the oxide layer and the bare steel?*

These questions will be answered using a combination of different experiments, both to investigate the oxide layer characteristics and hydrogen permeation behaviour of the oxide layer with respect to the bare steel. For this purpose, characterization techniques such as optical microscopy, scanning electron microscopy, Raman spectroscopy, as well as electrochemical methods have been employed.

This thesis is divided into 7 main chapters:

- **Chapter 2**: Provides an insight into the formation and properties of surface oxide layers on steel, the nature of hydrogen-oxide layer interaction on steel, and the various experimental methods used for investigating hydrogen permeation in steel.
- **Chapter 3**: Discusses the materials and experimental methods used in the study.
- **Chapter 4**: Presents the results obtained from the experimental methods.
- **Chapter 5**: Discusses the results and analyses what they mean with respect to the research questions.
- **Chapter 6**: Provides conclusions based on the findings of this study.
- **Chapter 7**: Offers recommendations for future research related to this study.

3

Materials and Methodology

This chapter details the materials and experimental approach used in the study. First, the oxide layer characterization on the X65 pipeline steel is presented. Both the hydrogen/oxide layer interaction on the steel surface and the hydrogen/steel interaction were investigated using Cyclic Voltammetry (CV), Electrochemical Impedance Spectroscopy (EIS), and Devanathan-Stachurski (DS) permeation cell experiments. Additionally, the oxide layer on the steel surface was characterized using Optical Microscopy (OM), Scanning Electron Microscopy (SEM), and Raman Spectroscopy. Choosing the appropriate experimental methodologies was essential to effectively address the research scope. Therefore, the methodologies used in this study were informed by critical experimental approaches highlighted throughout the literature review.

3.1. Material and Composition

The material used in this research project was API 5L X65 pipeline steel, provided by Element Materials Technology in the form of a 500 mm × 100 mm × 20 mm section of pipeline. Both the inner and outer surfaces of the pipeline material were covered with an oxide layer, indicative of its exposure to environmental and operational conditions. The chemical composition of the steel (according to API 5L specifications [3]) is provided in Table 3.1.

Grade	**C (% max)**	**Mn (% max)**	**P (% max)**	**S (% max)**	**V (% max)**	**Nb (% max)**	**Ti (% max)**
X65 (Seamless)	0.28[e]	1.45[b]	0.030	0.030	–	0.09[d]	0.06[d]
X65 (Welded)	0.26[e]	1.45[b]	0.030	0.030	–	0.09[d]	0.06[d]

Table 3.1: Chemical composition of X65 steel for seamless and welded pipes (PSL 1) with $t \leq 25.0$ mm. Superscripts provide additional notes on specific conditions. Modified from [3].

[a] Cu ≤ 0.50 %; Ni ≤ 0.50 %; Cr ≤ 0.50 %; and Mo ≤ 0.15 %.
[b] For each reduction of 0.01 % below the specified maximum concentration for carbon, an increase of 0.05 % above the specified maximum concentration for Mn is permissible, up to a maximum of 1.65 % for grades ≥ L245 or B, but ≤ L360 or X52; up to a maximum of 1.75 % for grades > L360 or X52, but < L485 or X70; and up to a maximum of 2.00 % for Grade L485 or X70.
[c] Unless otherwise agreed, Nb + V ≤ 0.06 %.
[d] Nb + V + Ti ≤ 0.15 %.
[e] Unless otherwise agreed.
[f] Unless otherwise agreed, Nb + V + Ti ≤ 0.15 %.
[g] No deliberate addition of B is permitted, and the residual B ≤ 0.001 %.

3.2. Electrochemical Experiments

Sample Preparation

The samples utilized for the electrochemical experiments were cut to dimensions of 30 mm x 30 mm x 1 mm using EDM machining. For the steel samples with an oxide layer (henceforth referred to as X65 Oxide), only one surface was ground using 180 to 2000 grit damp SiC paper, followed by polishing with 3 μm and 1 μm diamond suspensions, rinsing with isopropanol, and drying with compressed air. For the bare steel samples (henceforth referred to as X65 Bare), both sides were ground and polished using the same procedure. Between experiments, the samples were stored in a vacuum desiccator maintained at 21°C and 35% relative humidity (RH). In addition, XPS analysis of the bare steel surfaces was performed after three different exposure times to investigate the thickness and composition of the native oxide layer grown on the samples under storage conditions.

The thickness of the bare steel sample tested was measured at five different points to ensure consistency and accuracy. The measurements obtained were 0.89 mm, 0.90 mm, 0.90 mm, 0.91 mm, and 0.92 mm. The calculated average thickness of the sample was 0.90 mm, with a standard deviation of ±0.01 mm. The thickness of two oxide samples was measured to evaluate variability across different specimens. The thickness measurements of the first oxide sample were 1.39 mm, 1.46 mm, 1.42 mm, 1.52 mm, and 1.55 mm. The calculated average thickness of the sample was 1.47 mm, with a standard deviation of ±0.07 mm. Comparatively, the second oxide sample had thickness measurements of 1.03 mm, 1.04 mm, 1.13 mm, 1.14 mm, and 1.27 mm. The calculated average thickness of this sample was 1.12 mm, with a standard deviation of ±0.09 mm.

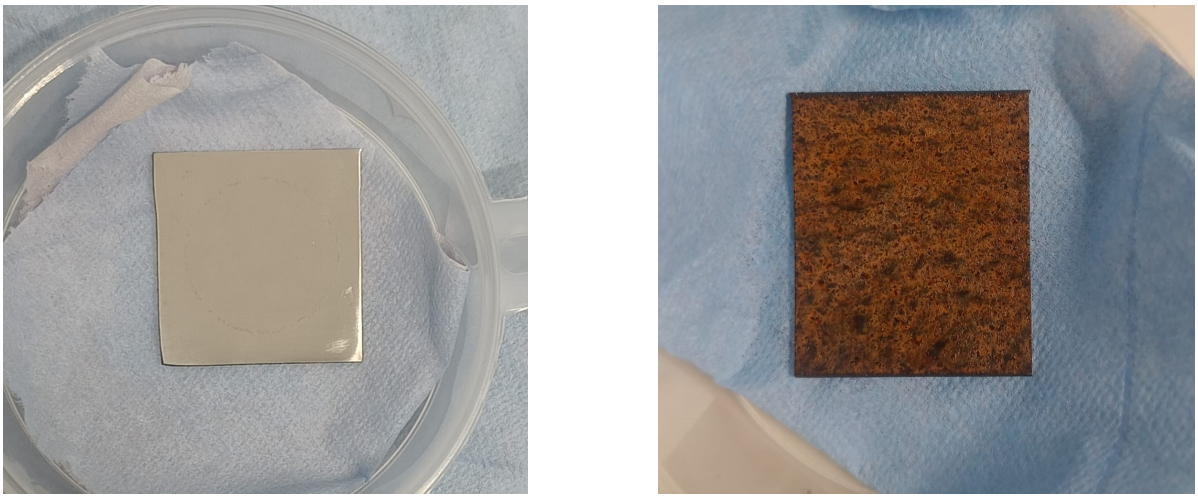

(a) X65 Bare steel sample.

(b) As-received X65 steel sample with oxide layer.

Figure 3.1: Comparison of the X65 steel sample conditions: bare steel (left) and as-received oxide layer (right).

3.2.1. DS Permeation Cell Setup

In this experimental setup of a Devanathan-Stachurski (DS) cell, two electrochemical cells were arranged to investigate hydrogen permeation through the X65 steel samples. The charging cell contained an electrolyte of 0.1 M NaOH with 3 g/L ammonium thiocyanate (NH_4SCN) added as a hydrogen recombination poison and to enhance atomic hydrogen entry [110, 111]. Meanwhile, the detection cell contained 0.1 M NaOH as the electrolyte, creating a controlled environment for detecting hydrogen oxidation. Platinum (Pt) counter electrodes and Hg/HgO

reference electrodes were used in both cells to maintain precise electrochemical control. The X65 steel sample was positioned between the two cells, with rubber O-rings providing a sealed boundary on either side to isolate the exposed area, which was set at 2.54 cm^2.

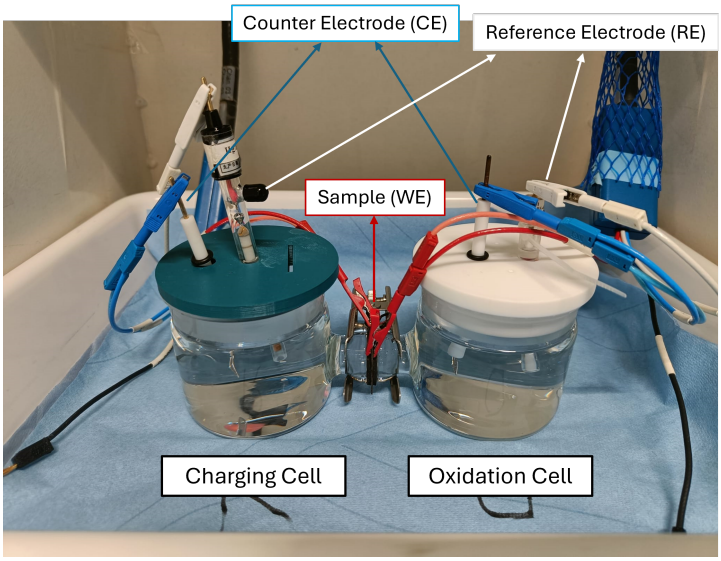

(a) Electrochemical permeation setup used for the experiments.

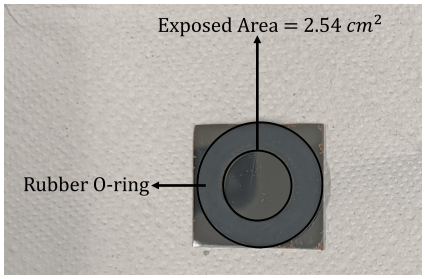

(b) Exposed area of the samples used for electrochemical experiments.

Figure 3.2: Electrochemical permeation setup (left) and exposed sample area (right).

The hydrogen permeation current was continuously measured on the detection side of the sample throughout the experiment. This current corresponds to the oxidation of hydrogen atoms that permeate through the steel, enabling evaluation of hydrogen transport behaviour during the preconditioning, charging, and discharging phases. On the entry side, only the charging current was monitored to confirm and control hydrogen generation during the charging step.

In this experiment, the X65 Oxide sample was arranged so that the side with the surface oxide layer faced the charging cell, while the opposite side, directed toward the detection cell, was sputter-coated with a 50-70 nm palladium (Pd) layer to facilitate hydrogen oxidation. The procedure for Pd layer deposition is explained in detail in Table B.1 of Appendix B. To begin, a potential of +400 mV (vs. Hg/HgO) was applied to the detection side of the samples without any charging potential/current. This initial setup helped establish a stable background current of 0.1-0.5 μA/cm^2. Once this baseline current was reached, the +400 mV potential was maintained continuously throughout the experiment, allowing for the steady oxidation of hydrogen permeating through the bare steel and the oxide/steel system.

Hydrogen charging was initiated after stabilization of the background current. Two distinct sets of experiments were performed to evaluate the effect of charging conditions on hydrogen permeation:

Set 1: Galvanostatic Charging - A constant cathodic current density of 5.9 mA/cm^2 was applied using a standard D-S permeation setup (Figure 3.2a). This setup did not include a reference electrode in the charging cell. Galvanostatic charging was performed for 6 hours for the X65 Bare sample and 43 hours for the X65 Oxide sample to increase the likelihood of achieving steady-state conditions. The applied current density was chosen to ensure sufficient hydrogen generation at the charging side to permeate through the steel.

Set 2: Potentiostatic Charging - A constant cathodic potential of -1.2 V (vs. Hg/HgO) was

applied to the charging side to initiate hydrogen generation on the entry surface. A reference electrode was included in the charging cell to ensure precise control and monitoring of the charging potential. The aforementioned cathodic potential was selected based on two considerations: (1) the potential corresponding to the hydrogen evolution reaction (HER) peak identified in the CV scan for the X65 Bare sample, and (2) the region of interest in the iron Pourbaix diagram (Figure 3.3), ensuring operation within the stability domain for hydrogen evolution. It must be noted that the Pourbaix diagram values are approximate and should be interpreted with a degree of flexibility.

Preconditioning, charging, and discharging: Throughout all phases of the experiments, the permeation current measured on the detection side reflects the oxidation of hydrogen atoms that successfully diffuse through the sample. This current serves as a direct indicator of hydrogen transport behaviour and enables comparison of the effects of different charging conditions on hydrogen permeation. On the entry side, the charging current was used to ensure consistent hydrogen generation during the charging step.

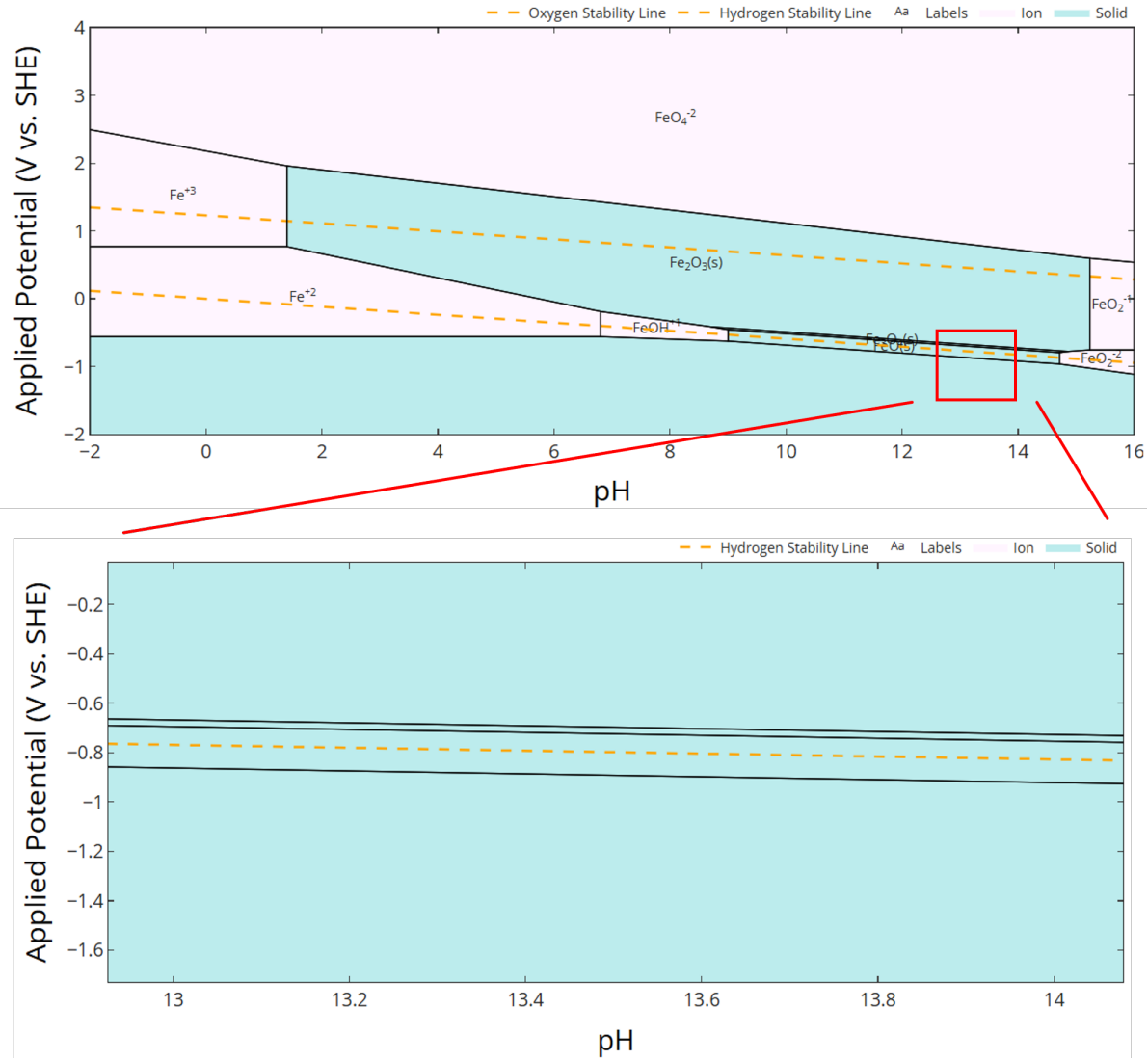

Figure 3.3: Pourbaix diagram of iron at $25^{o}C$. The red rectangle indicates the pH range of the electrolyte used in this study and the lower dashed orange line represent the stability region of water, below which hydrogen evolution occurs. Generated using The Materials Project [112, 113, 114, 115].

3.2.2. Electrochemical Test Setup

The electrochemical tests were conducted using a Biologic VSP-300 potentiostat and the EC-Lab V11.43 software. The experimental setup consisted of a bottom-mounted, three-electrode cell with an Ag/AgCl reference electrode (saturated KCl) filled with 3.5M KCl, henceforth referred to as SSC_{sat} in this study. To minimize the impact of contamination, the filling solution was replaced regularly. A platinum wire mesh was used as the counter electrode, and the material surface under investigation functioned as the working electrode. The electrolyte used was a 0.1 M NaOH solution containing 3 g/L of ammonium thiocyanate (NH_4SCN), which was freshly replaced before each test. The pH of this solution was maintained in the range of 13.0–13.5. Before beginning the electrochemical testing, the setup was enclosed in a Faraday cage to protect it from external electromagnetic interference. All experiments were conducted at room temperature.

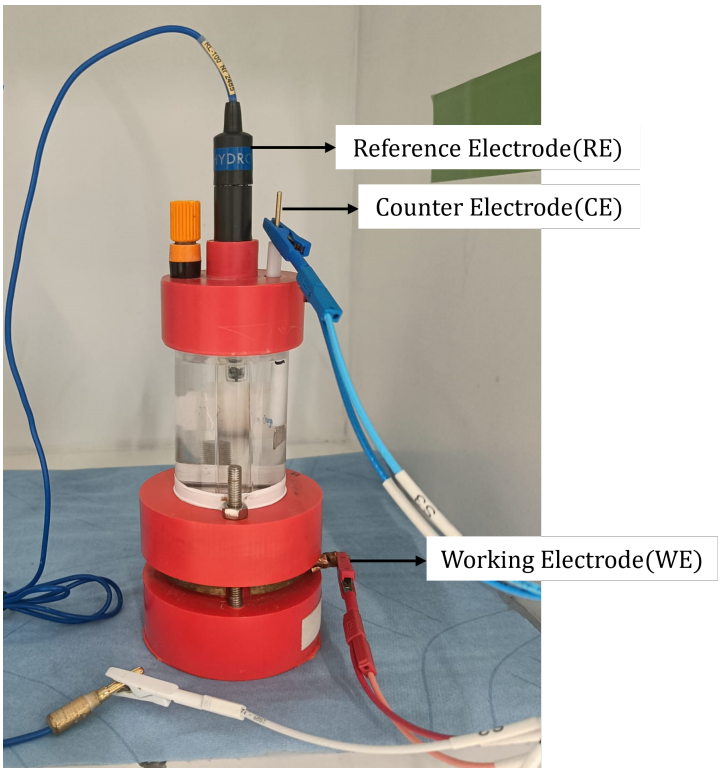

Figure 3.4: Picture of the actual three-electrode setup used for the electrochemical experiments. The sample is bottom mounted and clamped between the two bottom plates, with a circular area of 2.54 cm^2 being exposed to the electrolyte.

3.2.3. Electrochemical Impedance Spectroscopy

Electrochemical Impedance Spectroscopy (EIS) is an electrochemical technique widely used to investigate the electrochemical properties of materials, especially in corrosion studies. EIS works by applying a small alternating current (AC) signal to a sample and measuring the resulting voltage response over a range of frequencies. The impedance, or resistance to the flow of electrons, is then analysed as a function of frequency. This method provides valuable insights into the resistive and capacitive behaviour of surface oxide layers, electrolyte interactions, and the overall corrosion mechanisms. EIS is particularly effective at distinguishing between different electrochemical processes occurring at various time scales, such as charge transfer at the metal-oxide interface and diffusion of ions through the oxide layer. EIS data can

be evaluated by fitting the data to an equivalent electrical circuit. The physical components of the metal/electrolyte interface should be described by the electrical circuit elements.

In this paper, EIS is used to investigate the effect of cathodic hydrogen charging on the electrochemical response of the X65 Bare and X65 Oxide samples. By evaluating the electrochemical behaviour before and after cathodic hydrogen charging, the study aims to understand how hydrogen ingress impacts the bare steel and the oxide layer, including its ability to prevent hydrogen permeation. This is particularly relevant because hydrogen charging can degrade oxide layers, compromising their stability and potentially increasing their susceptibility to hydrogen embrittlement. EIS provides valuable insights into changes in the resistive and capacitive properties of both the bare steel and the oxide layer, enabling an assessment of their stability and integrity under hydrogen exposure. This evaluation is critical for understanding the long-term durability of steel in hydrogen-rich environments.

The electrochemical procedure in Table 3.2 was carried out for both the X65 Bare and the X65 Oxide samples before and after hydrogen permeation testing. For each case, the measurements were conducted with the samples at OCP to evaluate the active electrochemical responses of the materials under their initial conditions and after hydrogen exposure. This provided a comparative analysis of the electrochemical behaviour of the bare steel and oxide layer, allowing the investigation of changes induced by hydrogen charging. The experimental EIS data were fitted to corresponding equivalent electrical circuits using the ZView version 4.0i software, enabling the interpretation of key resistive and capacitive properties of the bare surface and oxide layer.

3.2.4. Cyclic Voltammetry

Cyclic Voltammetry (CV) is a widely used electrochemical technique for studying the redox behaviour of materials and the electrochemical reactions occurring at the electrode surface. In CV, the potential applied to the electrode is swept linearly back and forth between two limits, while the resulting current is measured. The plot of current versus potential, called a voltammogram, provides information about the oxidation and reduction processes, reaction kinetics, and electrochemical stability of the material. CV is especially useful for analysing surface reactions, electroactive species, and the formation or dissolution of surface layers, making it highly relevant for characterizing oxide layers.

In this thesis, CV is utilized to compare the electrochemical response of both sets of X65 steel samples: one with an oxide layer and another with no oxide layer (referred to as the bare steel), both before and after cathodic hydrogen charging. By analysing the voltammograms for both conditions, the study aims to understand how hydrogen charging affects the surface reactions taking place on the steel surface in the presence and absence of the oxide layer. This comparison helps to reveal how the oxide layer and the hydrogen charging influence the redox reactions occurring on the steel surface.

No.	Step	Relevant Parameters
1	OCP	Duration: 2 hours Electrolyte: 0.1 M NaOH + 3 g/L NH_4SCN
2	EIS	Frequency Range: 1 MHz - 10 mHz Voltage Amplitude: 10 mV Number of Points per Decade (N_d): 10 Electrolyte: 0.1 M NaOH + 3 g/L NH_4SCN
3	CV	Initial Potential: -1.740 V vs. SSC_{sat} Potential Range: -1.740 V to 0.160 V vs. SSC_{sat} Final Potential: -1.740 V vs. SSC_{sat} Scan Rate: 2.5 mV/s Number of Scans: 6 Electrolyte: 0.1 M NaOH + 3 g/L NH_4SCN

Table 3.2: Electrochemical Test Parameters for OCP, EIS, and CV.

3.3. Raman Spectroscopy

Raman spectroscopy is a non-destructive vibrational spectroscopy technique used to study molecular vibrations and structures through the inelastic scattering of light. When a laser interacts with a material, most of the light scatters elastically (Rayleigh scattering), but a small fraction scatters inelastically (Raman scattering), providing information about the vibrational states of the molecules. The energy difference between the incident and scattered light, known as the Raman shift, is characteristic of the molecular bonds and structure of the material. This makes Raman spectroscopy ideal for identifying specific compounds based on their unique vibrational ”fingerprints.”

When applied to the study of surface oxide layers on steel, Raman spectroscopy can differentiate between various iron oxide and oxyhydroxide phases like haematite (α-Fe_2O_3), magnetite (Fe_3O_4), maghemite (γ-Fe_2O_3), and goethite (α-FeOOH). Each of these oxides has distinct vibrational modes, which manifest as specific peaks in the Raman spectrum. By analysing the peak positions, intensities, and shapes, the composition of the oxide layer can be determined. Raman’s high chemical specificity allows for the identification of mixed layers, where multiple oxides coexist on the surface.

In this thesis, Raman spectroscopy is employed to characterize the oxide layer present on the surface of the X65 steel samples. The technique is used to identify the specific phases of iron oxides and oxyhydroxides formed on the steel surface, such as haematite, magnetite, and goethite, based on their unique Raman spectral signatures. The surface composition is analysed by examining the Raman shifts and intensities, allowing for the identification of the dominant oxides and any mixed phases. Additionally, the depth profile of the oxide layer is characterized by examining a cross-section of the oxide layer on the steel samples. This cross-sectional analysis attempts to provide insight into how the oxide phases vary with depth, revealing the layered structure of the oxide layer and the distribution of different oxides from the surface to the oxide/steel interface. The Raman spectroscopy apparatus and experimental configuration used for these analyses are detailed in Table 3.3.

Parameter	Details
Raman System	WITec Alpha 300R
Laser Type	Nd:YAG
Laser Wavelength	532 nm
Laser Power	0.5 mW (to prevent sample damage)
Objective Magnification	50x
Working Distance	9.1 mm
Lateral Resolution	500 nm
Depth Resolution	1 µm
Grating	600 grooves/cm^2
Spectral Resolution	2 cm^{-1} Raman shift
Integration Time	5 seconds
Number of Accumulations	10

Table 3.3: Details of the Raman spectroscopy apparatus and experimental configuration.

4

Experimental Results

4.1. Native Oxide Layer Characterization - X65 Bare Sample

XPS analysis was performed to evaluate the thickness and composition of the native oxide layer formed on the X65 Bare steel surface when exposed to the aforementioned storage conditions. Analysis was performed using a PHI-5400 ESCA equipped with an Al Kα monochromatic X-ray source ($h\nu = 1486.6$ eV). The analysis began with the acquisition of a wide-range survey spectrum to identify the elements present on the surface and to confirm the absence of significant contaminants. These survey spectra were obtained with a pass energy of 89.45 eV and covered a binding energy range of 0 eV to 1100 eV.

High-resolution scans were subsequently performed for the Fe 2p, O 1s, and C 1s regions, with a pass energy of 71.55 eV to enable detailed peak deconvolution. The binding energy range was calibrated to the adventitious C 1s peak at 284.8 eV.

The samples were prepared in as-received conditions, with no additional cleaning performed prior to analysis. There was a time delay of approximately 15 minutes between sample transfer from storage conditions to the XPS vacuum chamber, during which minimal environmental exposure occurred. The vacuum chamber pressure during analysis was maintained at $\sim 10^{-8}$ mbar.

Peak fitting and deconvolution of the spectra were performed using Gaussian-Lorentzian line shapes and the Shirley background subtraction method. As can be seen in Table 4.1, the Fe 2p spectra were resolved into metallic Fe (Fe^0), Fe^{2+}, and Fe^{3+}, while the O 1s spectra identified lattice oxygen (O^{2-}_{lattice}) and hydroxyl species (OH^-_{lattice} and OH^-_{ads}). The C 1s spectra provided a reference for energy calibration and revealed surface contamination from adventitious carbon.

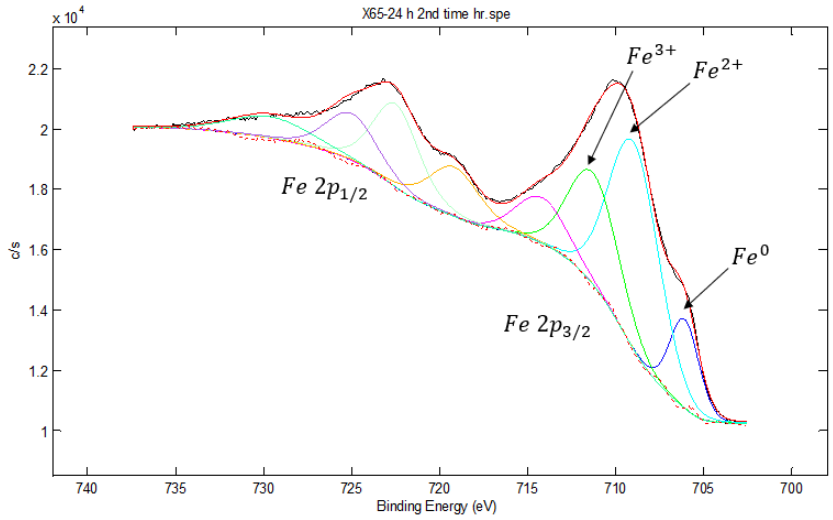

(a) High-resolution Fe $2p_{3/2}$ spectra for the X65 Bare sample after 24 hours of exposure in storage conditions.

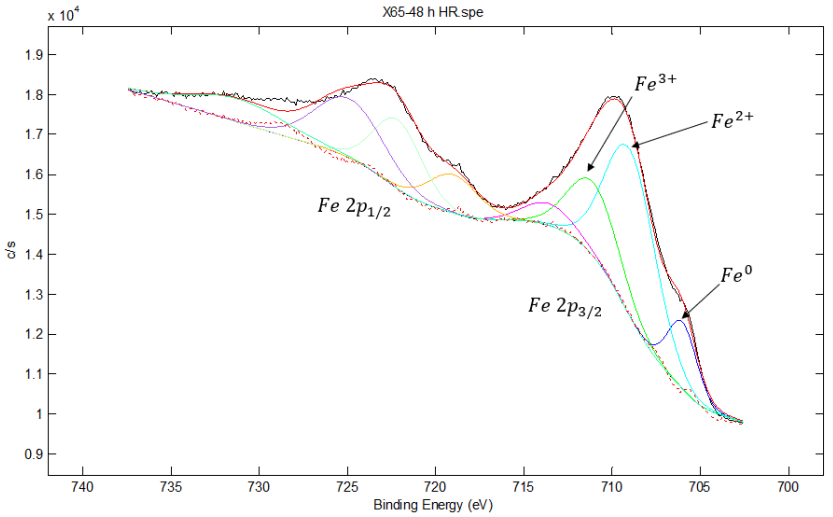

(b) High-resolution Fe $2p_{3/2}$ spectra for the X65 Bare sample after 48 hours of exposure in storage conditions.

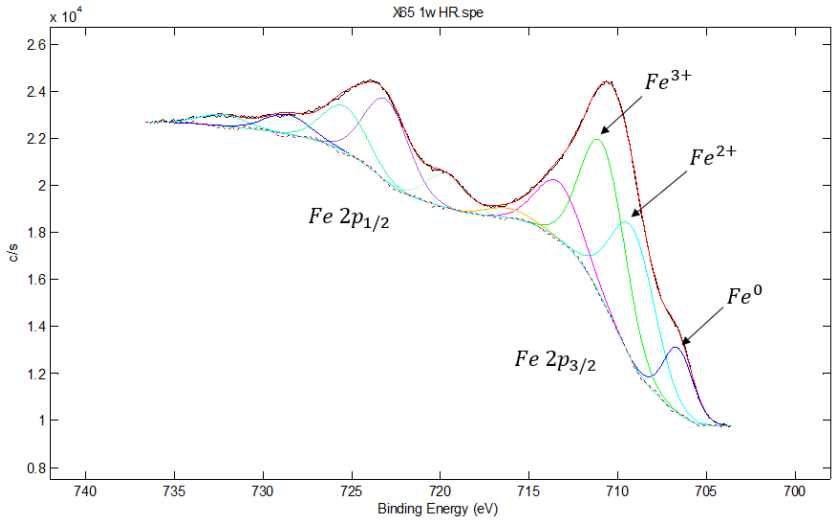

(c) High-resolution Fe $2p_{3/2}$ spectra for the X65 Bare sample after 168 hours (1 week) of exposure in storage conditions.

Figure 4.1: Deconvoluted high-resolution Fe $2p_{3/2}$ XPS spectra for X65 Bare samples after exposure to storage conditions for (a) 24 hours, (b) 48 hours, and (c) 168 hours (1 week).

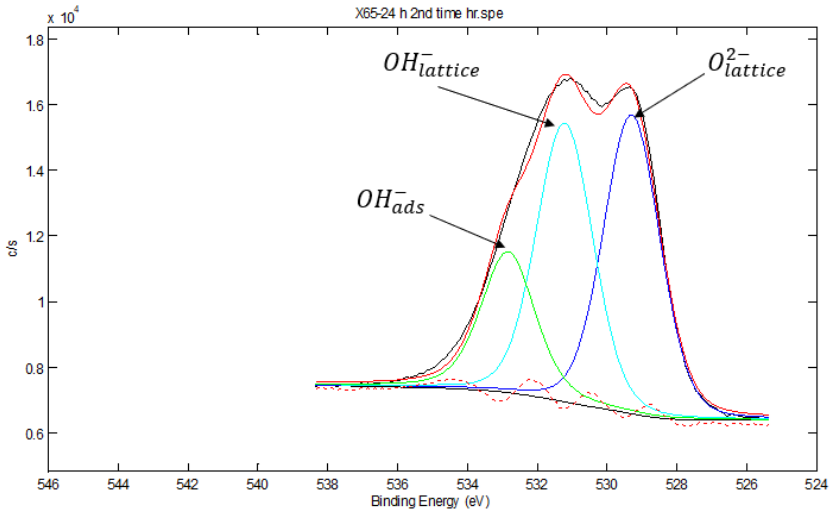

(a) High-resolution O 1s XPS spectrum for the X65 oxide sample after 24 hours of exposure in storage conditions.

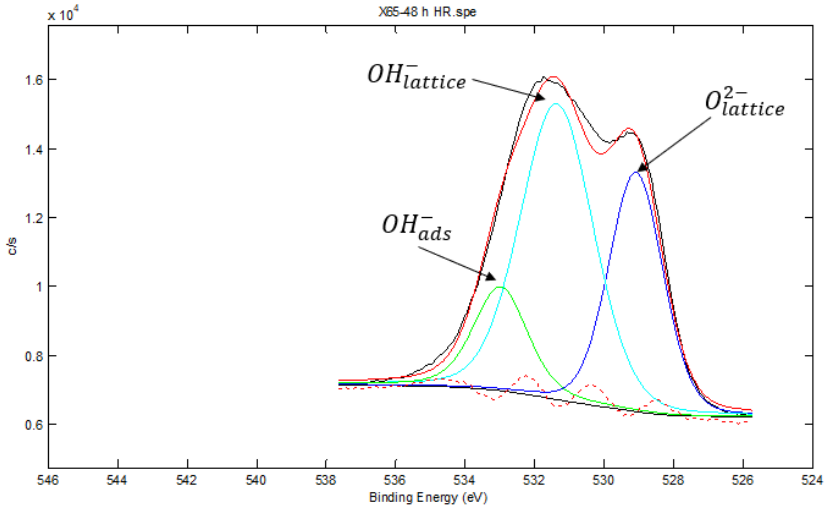

(b) High-resolution O 1s XPS spectrum for the X65 oxide sample after 24 hours of exposure in storage conditions.

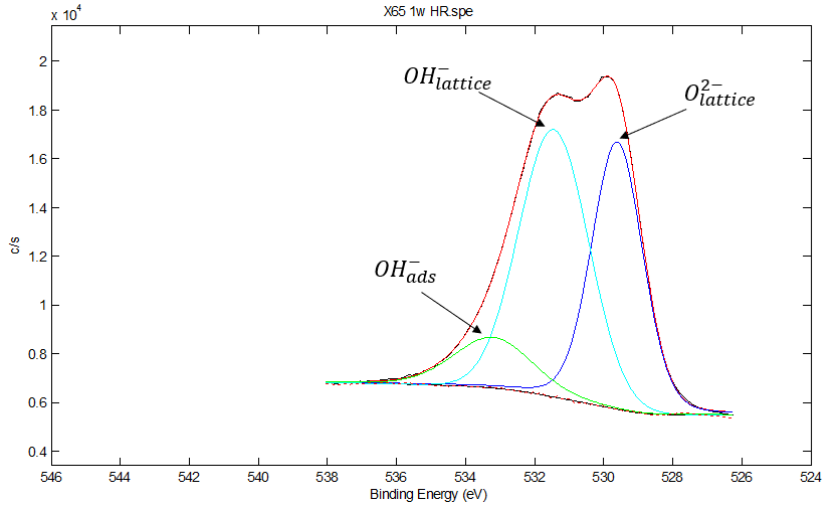

(c) High-resolution O 1s XPS spectrum for the X65 oxide sample after 24 hours of exposure in storage conditions.

Figure 4.2: Deconvoluted high-resolution O 1s XPS spectra for X65 oxide samples after exposure to storage conditions for (a) 24 hours, (b) 48 hours, and (c) 168 hours (1 week).

Peak	Sub-peak	Characteristics	Exposure time in storage conditions		
			24 hours	48 hours	168 hours
Fe $2p_{3/2}$	Fe^0	BE [FWHM], eV	706.1 [1.98]	706.0 [1.98]	706.6 [1.98]
		Area (%)	14.1	12.5	13.2
	Fe^{2+}	BE [FWHM], eV	709.0 [3.36]	709.0 [3.36]	709.1 [2.98]
		Area (%)	55.8	59.6	40.1
	Fe^{3+}	BE [FWHM], eV	711.3 [3.36]	711.0 [3.36]	710.8 [2.98]
		Area (%)	30.1	26.3	46.7
O $1s$	O^{2-}_{lattice}	BE [FWHM], eV	529.3 [1.91]	529.1 [1.84]	529.6 [1.74]
		Area (%)	35.4	32.0	39.0
	OH^-_{lattice}	BE [FWHM], eV	531.2 [1.91]	531.4 [2.48]	531.4 [2.38]
		Area (%)	48.5	52.9	49.3
	OH^-_{ads}	BE [FWHM], eV	532.8 [1.83]	532.9 [1.83]	533.2 [2.69]
		Area (%)	16.1	15.1	11.5

Table 4.1: Binding energies, FWHM values, and relative peak areas obtained from deconvolution of the high-resolution Fe $2p_{3/2}$ and O $1s$ spectra for native oxide films after different exposure times in storage conditions.

The high-resolution Fe 2p and O 1s XPS spectra obtained for the X65 Bare samples after 24 hours, 48 hours, and 168 hours of exposure in storage conditions are shown in Figures 4.1 and 4.2, respectively. The deconvolution of the Fe 2p 3/2 spectra indicates contributions from Fe^0, Fe^{2+}, and Fe^{3+}, while the O 1s spectrum consists of three distinct sub-peaks corresponding to lattice oxygen (O^{2-}_{lattice}), lattice hydroxyls (OH^-_{lattice}), and adsorbed hydroxyls (OH^-_{ads}).

The identification of these peaks and the rationale for determining the oxide composition are based on the XPS analysis of native oxide layers on carbon steel conducted by Chan-Rosado and Pech-Canul [17]. According to their work, the presence of O^{2-}_{lattice} is indicative of iron oxides such as Fe_2O_3 and Fe_3O_4, while OH^-_{lattice} is associated with iron oxyhydroxides, predominantly FeOOH. Thermodynamic considerations suggest that FeO is unlikely to be present due to its instability under ambient conditions; it is readily oxidized to Fe_3O_4 at temperatures below 570°C. The Fe_3O_4 phase is typically associated with the inner oxide layer formed during oxidation in ambient air.

Based on this interpretation, the native oxide film on X65 Bare samples likely consists of a bilayer structure with an inner Fe_3O_4 layer and an outer FeOOH layer. The adsorbed hydroxyl peak (OH^-_{ads}) observed in the O 1s spectra is attributed to the dissociative adsorption of water molecules on the oxide surface and appears to be relatively stable under the studied conditions. These results align with previous studies on the oxidation of iron in ambient air and provide a framework for understanding the composition of native oxide films under controlled humidity storage conditions.

An estimation of the native oxide layer thickness was made using the Strohmeier equation [18], which utilizes the intensities of the Fe $2p_{3/2}$ photoelectron peaks of the metal and oxide:

$$d = \lambda_{ox} \cos\theta \ln\left(1 + (N_m \lambda_m I_{ox} / N_{ox} \lambda_{ox} I_m)\right) \tag{4.1}$$

As a first approximation, it is considered that the steel is covered by an oxide layer comprising a mixture of FeOOH and Fe_3O_4. Here, $\lambda_{ox} = 15.8\,\text{Å}$ and $\lambda_m = 12.4\,\text{Å}$ are attenuation lengths of photoelectrons emitted by the Fe $2p_{3/2}$ core level in the oxide and in the bulk metal, respectively. θ is the takeoff angle of photoelectrons w.r.t. the normal, $N_m = 0.141\,\text{mol/cm}^3$ and $N_{ox} = 0.064\,\text{mol/cm}^3$ represent the atomic densities of iron in the metal and in the oxide, respectively. I_m and I_{ox} represent the intensities of the Fe $2p_{3/2}$ photoelectron peaks of the metal (the peak area of Fe(0)) and the oxide (sum of the peak areas of Fe(III) and Fe(II)), respectively. Values of λ and N were taken from existing literature [19, 20].

Exposure Time	I_m	I_{ox}	Oxide Thickness (nm)
24h	3634	22205	3.66
48h	6397	38926	4.14
168h	5948	39079	3.97

Table 4.2: Calculated native oxide thicknesses for X65 Bare samples stored for 24h, 48h, and 168h using XPS Fe spectra.

The findings presented in Table 4.2 demonstrate that XPS analysis reveals the growth of a native oxide layer with a thickness in the range of 3–4 nm on the surface of the X65 Bare sample under the specified storage conditions. It should be noted that the 15-minute delay between transferring the samples from storage conditions to the XPS vacuum chamber may have allowed additional surface reactions with the atmosphere, influencing the measured oxide thickness.

The observed differences in oxide thickness across the three exposure times (24h, 48h, and 168h) may be attributed to variations in peak fitting during the spectral deconvolution process, as small changes in the peak intensities or fitting parameters can influence the calculated values. Other potential contributors to these differences include sample preparation variability, localized heterogeneity in the oxide layer, or slight inconsistencies in storage conditions. These findings highlight the importance of careful control and consideration of experimental conditions when analyzing surface oxide properties via XPS.

4.2. As-Received Oxide Layer Characterization - X65 Oxide Sample

To understand the role of the as-received surface oxide in mitigating hydrogen ingress, detailed characterization of their morphology, composition, and structure was performed. The techniques employed include optical microscopy, scanning electron microscopy with energy-dispersive X-ray spectroscopy (SEM-EDS), and Raman spectroscopy. These methods provided insights into the oxide layer's thickness, elemental distribution, and crystalline phases.

Optical micrographs were obtained at 500x magnification using the VHX-7000N Keyence digital microscope to estimate the thickness of the surface oxide layer on the X65 pipeline material. Thickness measurements were made from a cross-section of the oxide layer at three different locations, with five measurements conducted at each location and subsequently averaged. This approach ensured accurate and representative thickness estimation across the sampled areas of the oxide layer on X65 steel. Table 4.3 provides the average values of the oxide layer thickness at each location, along with the overall calculated average.

The thickness of the oxide layer on the X65 steel showed notable variation across three mea-

sured locations on the same layer (see Figure 4.3). The greatest thickness was observed at location 1, measuring $63.8 \pm 9.7\,\mu m$, followed by location 2 at $36.4 \pm 5.9\,\mu m$, and location 3 at $27.9 \pm 2.1\,\mu m$. The overall average thickness in all of these locations was calculated as $42.7 \pm 5.9\,\mu m$, which highlights the variability in the thickness of the oxide layer across the X65 steel surface.

Location	Average ± Std Dev (µm)
Location 1	63.8 ± 9.7
Location 2	36.4 ± 5.9
Location 3	27.9 ± 2.1
Overall Average	**42.7 ± 5.9**

Table 4.3: Average thickness measurements at different locations, with standard deviations included.

SEM images were captured with a JEOL JSM-IT100 InTouchScope™ Scanning Electron Microscope at an accelerating voltage of 20 kV to observe the cross-section of the oxide layer on the sample. Energy-dispersive X-ray spectroscopy (EDS) analysis was also conducted at various points across the thickness of the oxide layer, as can be seen in Figure 4.5. This allowed for a detailed elemental characterization at different depths within the oxide layer, providing information on the distribution of elements such as oxygen, carbon, manganese, and iron. The variation in elemental composition across different depths helps to understand the structure and composition of the oxide layer.

The elemental analysis reveals that iron (Fe) is the dominant component throughout the oxide layer, with a significant presence of oxygen (O) indicating oxide formation. Carbon (C) was also detected, possibly as a result of impurities during sample preparation and also the signal from the conductive resin in which the samples were embedded. Minor amounts of manganese (Mn) were also detected, which is likely due to signals being detected from the steel. As can be seen in Table 4.4, the composition varies slightly at each point analysed, suggesting that the oxide layer has a complex and layered structure. However, further confirmation of this hypothesis is required, which was attempted using the elemental mapping in the next section.

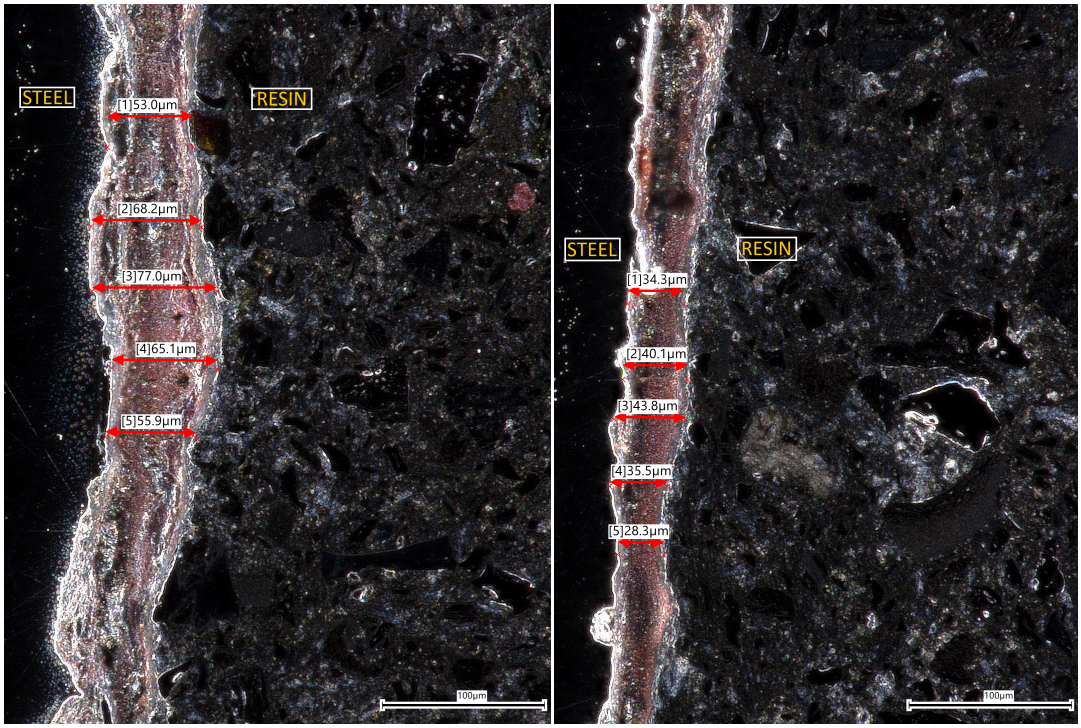

(a) Location 1 - thickness measurement.

(b) Location 2 - thickness measurement.

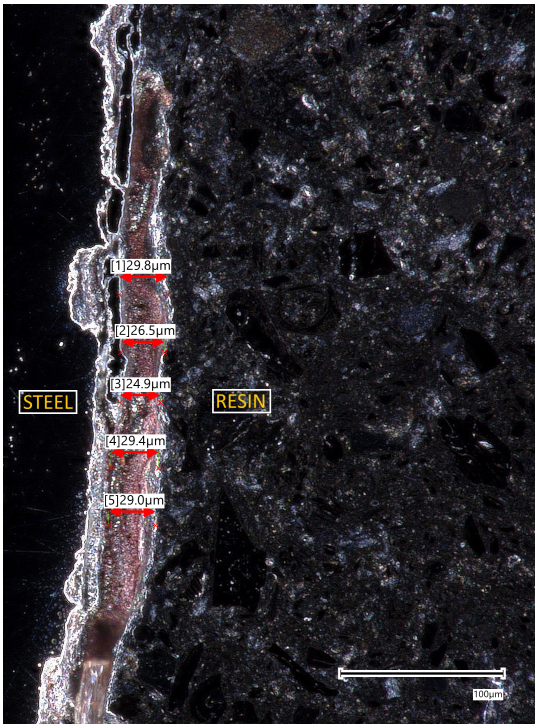

(c) Location 3 - thickness measurement.

Figure 4.3: Surface oxide layer thickness measurements on X65 steel at three different locations.

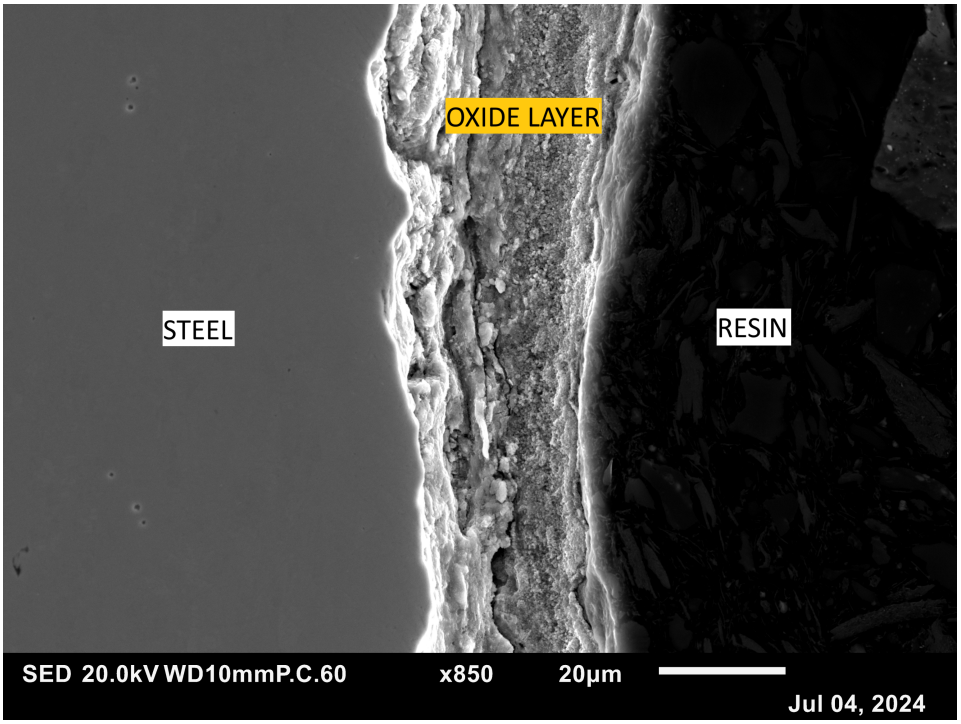

Figure 4.4: SEM image showing the cross-section of the oxide layer. The image captures the structure and morphology of the oxide layer at a 850x magnification, with a scale bar indicating 20 µm.

Element	Point 1 (004[Fe])		Point 2 (005[Fe])		Point 3 (006[Fe])	
	Mass %	Atom %	Mass %	Atom %	Mass %	Atom %
C	6.22	15.79	4.85	12.93	3.13	9.01
O	24.22	46.19	22.81	45.62	20.06	43.40
Mn	1.06	0.59	1.02	0.59	-	-
Fe	68.51	37.43	71.32	40.86	76.81	47.60

Table 4.4: Elemental composition (mass % and atom %) at various points within the oxide layer as determined by EDS analysis.

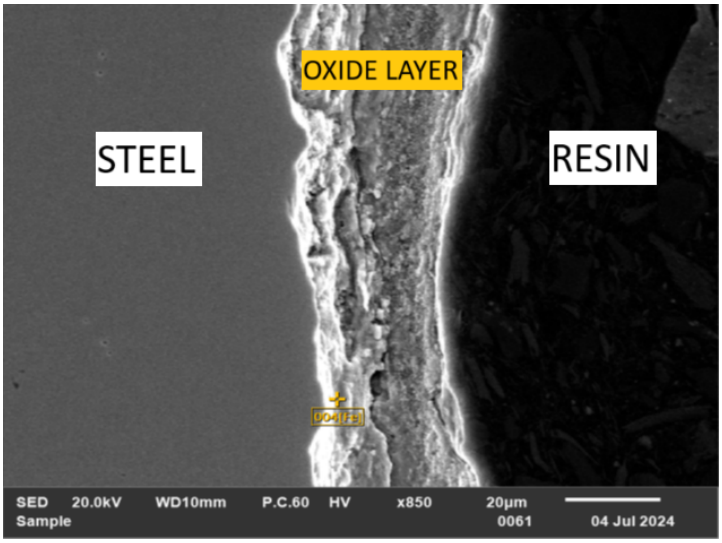

(a) SEM image of the oxide layer cross-section, with EDS analysis done at point 1 (labelled 004[Fe]).

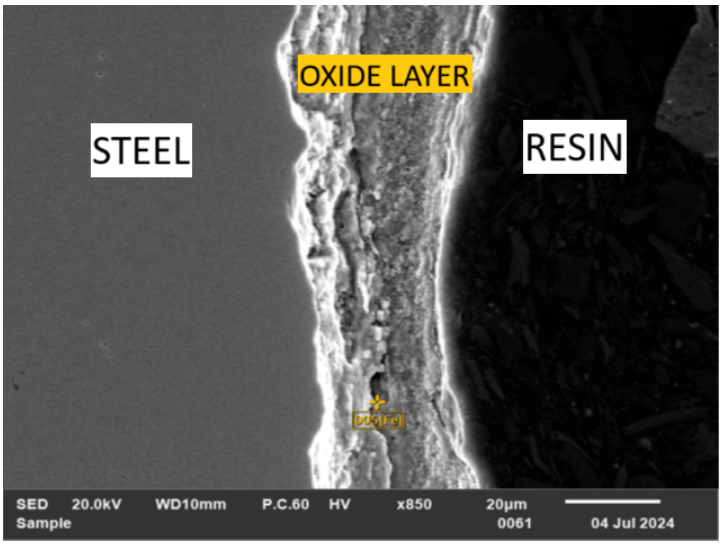

(b) SEM image of the oxide layer cross-section, with EDS analysis done at point 2 (labelled 005[Fe]).

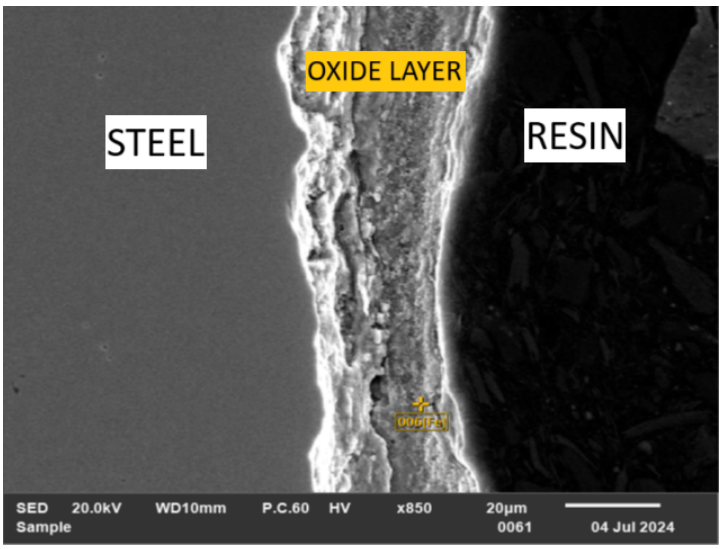

(c) SEM image of the oxide layer cross-section, with EDS analysis done at point 3 (labelled 006[Fe]).

Figure 4.5: SEM images of the cross-section of the oxide layer, with labelled points where EDS analysis was conducted.

The EDS mapping analysis of the cross-section of the oxide layer, as shown in Figure 4.6, reveals a uniform distribution of the detected elements across its thickness. Key elements, including iron (Fe), oxygen (O), and carbon (C), are consistently present throughout the thickness of the oxide layer with no observable gradient in their concentrations. This homogeneity in elemental distribution suggests that the oxide layer is compositionally uniform from the surface to the substrate, with no significant segregation or enrichment of elements at specific depths.

The uniform elemental distribution observed in the EDS mapping suggests that the oxide layer formed through a relatively homogeneous oxidation process, without distinct regions of varying elemental concentrations that are sometimes characteristic of oxides formed under highly variable environmental conditions. Raman spectroscopy, performed after EDS mapping, can provide further insights into the composition and structural characteristics of the oxide layer to validate this observation.

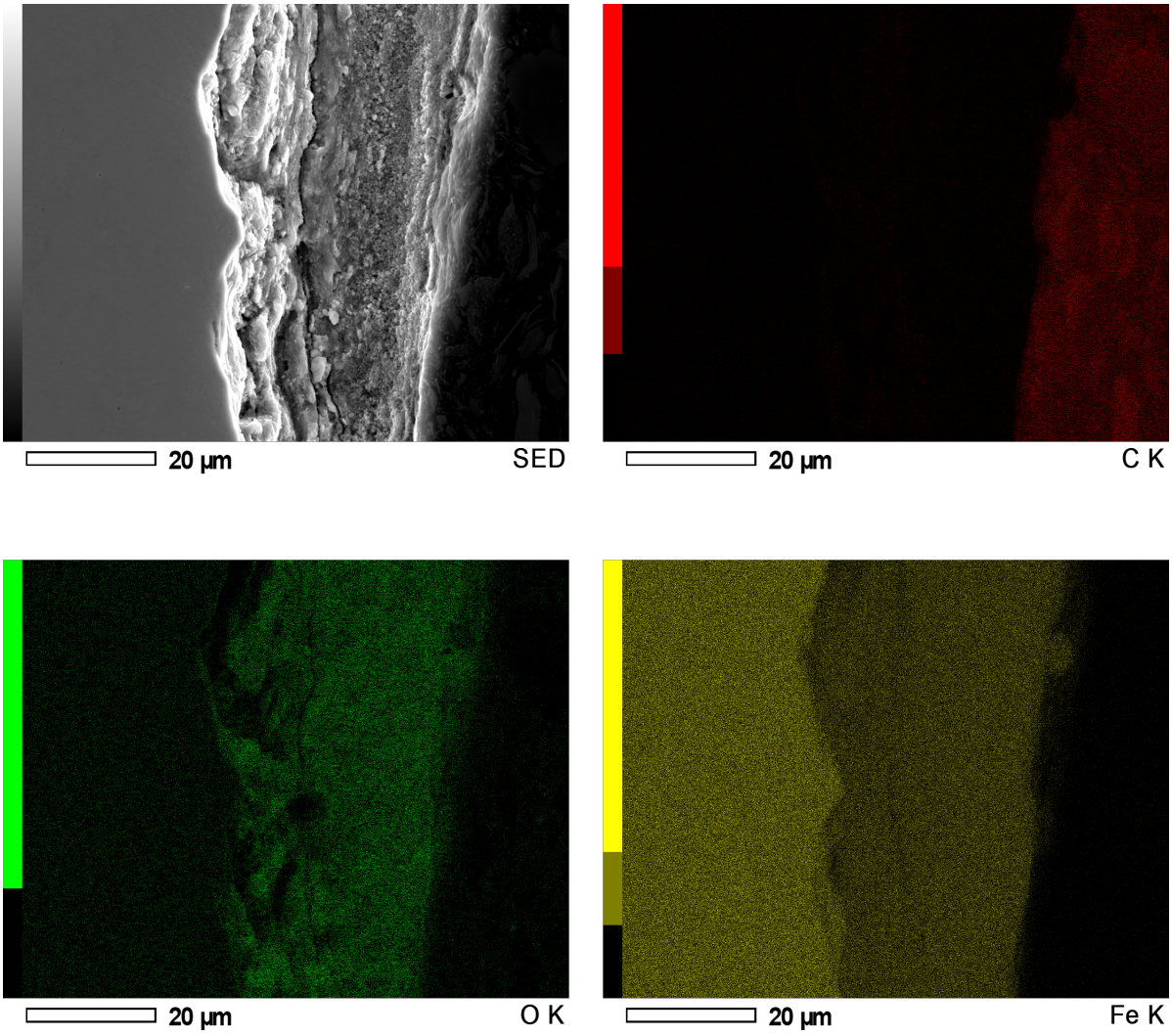

Figure 4.6: SEM image and EDS elemental mapping of the cross-section of the oxide layer. The elemental maps for key elements (such as Fe, O, C) are shown, with colours indicating the distribution of each element across the oxide layer thickness. Scale bars are included in each map for reference.

Element	Mass (%)	Atom (%)
C	18.76	43.77
O	12.39	21.69
Fe	68.85	34.54
Total	**100.00**	**100.00**

Table 4.5: Elemental composition with mass percentage and atomic percentage.

In order to investigate the chemical composition of the oxide layer, Raman spectroscopy was also performed at two different cross-sectional locations within the oxide layer. One of the locations for the cross-sectional Raman spectra investigation is presented here, with the other location's findings presented in Figures A.1 and A.2 in Appendix A. The Raman spectroscopy findings presented in Table 4.6 reveal that the oxide layer on the analysed samples is a mixture of haematite (α-Fe_2O_3) and magnetite (Fe_3O_4) / maghemite (γ-Fe_2O_3). As shown in Figure 4.7, all sampled points exhibit characteristic haematite peaks at 226 cm^{-1}, 291 cm^{-1}, 407 cm^{-1}, 411 cm^{-1}, and 1311–1320 cm^{-1}, consistent with literature on iron oxides [116, 117, 118]. The presence of haematite (α-Fe_2O_3) throughout the sampled points confirms it as a major component of the oxide layer.

In addition to haematite, the oxide layer contains magnetite (Fe_3O_4) and/or maghemite (γ-Fe_2O_3), as indicated by the peaks at 655 cm^{-1}, 659 cm^{-1}, and 663 cm^{-1}. These peaks are specifically associated with magnetite or its closely related variant maghemite [116, 118, 119], suggesting that the oxide layer is not purely haematite but rather a mixed iron oxide composition. The consistent identification of these peaks across multiple points supports the conclusion that the oxide layer is a mixture of both haematite (α-Fe_2O_3) and magnetite/maghemite (Fe_3O_4/γ-Fe_2O_3) phases. This mixture could result from specific oxidation conditions, where both stable and metastable forms of iron oxide co-exist on the surface.

Wüstite (FeO) is difficult to identify using Raman spectroscopy due to its thermodynamic instability below 570 °C and its tendency to decompose into magnetite (Fe_3O_4) and metallic iron (α-Fe) [116, 118, 119]. This transformation is governed by the disproportionation reaction:

$$4\text{FeO} \rightarrow \alpha\text{-Fe} + \text{Fe}_3\text{O}_4$$

In addition to its instability, the characteristic Raman peaks of wüstite overlap with those of magnetite, further complicating its unambiguous identification. These overlapping features make it difficult to distinguish between the two phases without supplementary analytical methods, such as X-ray diffraction (XRD) or electron microscopy. The presence of wüstite in the oxide layer typically suggests high-temperature exposure, but its detection in ambient conditions is rare due to its rapid transformation into more stable iron oxides or metallic phases. As a result, careful interpretation of Raman spectra is required when attempting to identify wüstite in complex oxide systems.

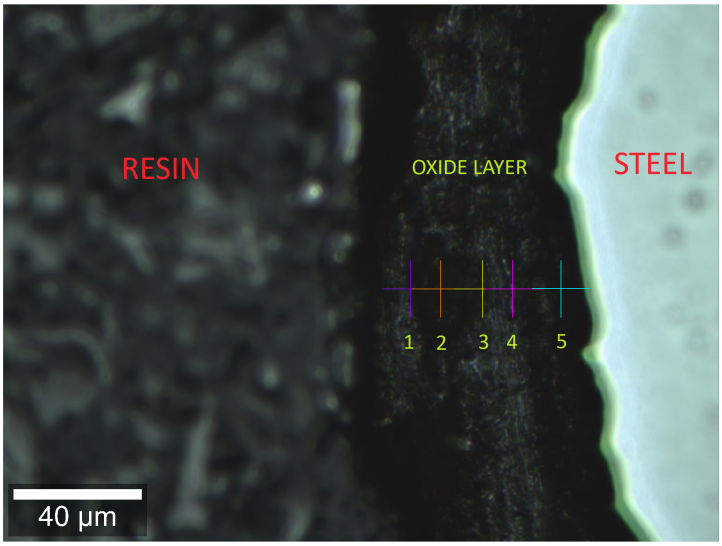

Figure 4.7: Optical micrograph showing the cross-section of the oxide layer, with marked locations (1, 2, 3, 4, and 5) indicating depth-wise locations within the oxide layer where Raman spectra were captured.

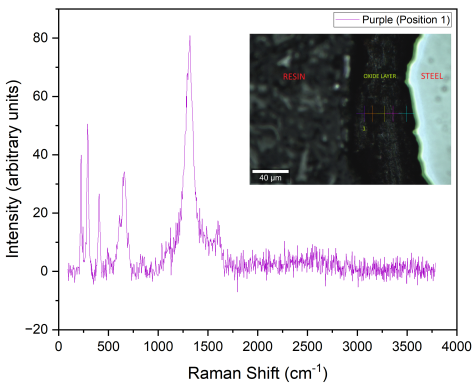

(a) Raman spectrum at location 1.

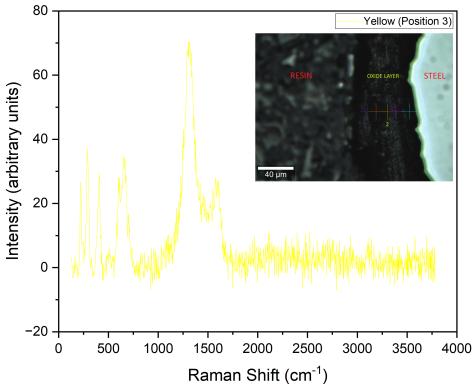

(b) Raman spectrum at location 3.

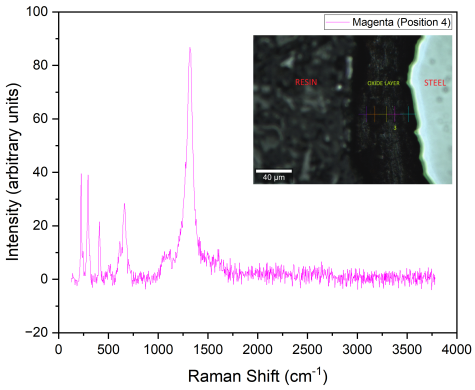

(c) Raman spectrum at location 4.

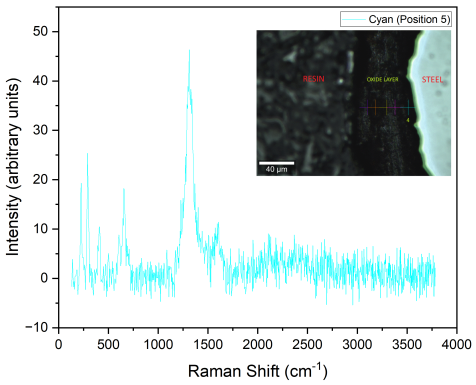

(d) Raman spectrum at location 5.

Figure 4.8: Raman spectra at the various locations (1, 3, 4, and 5) within the oxide layer cross-section, with the corresponding microscopic image inset. The spectrum at point 2 (orange) is not presented due to excessive noise in the signal, which made peak identification difficult.

Location	Peak Positions (cm^{-1})	Compound(s)	Sources
1 (Purple)	226	α-Fe_2O_3	[116, 117, 119]
	291	α-Fe_2O_3	[116, 118]
	407	α-Fe_2O_3	[116, 117]
	659	Fe_3O_4 / γ-Fe_2O_3	[116, 118, 119]
	1319	α-Fe_2O_3	[116, 118]
3 (Yellow)	221	α-Fe_2O_3	[116, 117, 119]
	287	α-Fe_2O_3	[116, 118]
	411	α-Fe_2O_3	[116, 117]
	610	α-Fe_2O_3 / γ-Fe_2O_3	[116, 119]
	659	Fe_3O_4 / γ-Fe_2O_3	[116, 118, 119]
	1311	α-Fe_2O_3	[116, 118]
4 (Magenta)	226	α-Fe_2O_3	[116, 117, 119]
	296	α-Fe_2O_3	[116, 118]
	411	α-Fe_2O_3	[116, 117]
	663	Fe_3O_4 / γ-Fe_2O_3	[116, 118, 119]
	1320	α-Fe_2O_3	[116, 118]
5 (Cyan)	226	α-Fe_2O_3	[116, 117, 119]
	291	α-Fe_2O_3	[116, 118]
	407	α-Fe_2O_3	[116, 117]
	655	Fe_3O_4 / γ-Fe_2O_3	[116, 118, 119]
	1311	α-Fe_2O_3	[116, 118]

Table 4.6: Comprehensive table of Raman peaks associated with various iron oxides, showing peak positions at all locations, corresponding chemical formulas, and sources [116, 117, 118, 119].

Raman spectral mapping was also conducted to investigate the sub-structuring of the oxide layer, as shown in Figure 4.9. This approach aimed to provide spatially resolved insights into the compositional distribution across different regions of the oxide layer. However, as can be seen in Figure 4.10, the resulting spectra were significantly noisy, making it challenging to identify distinct peaks and infer meaningful compositional information. The excessive noise in the signal is likely due to the limited Raman activity of the oxide layer in certain regions or interference from the underlying substrate. Consequently, the analysis could not reliably confirm variations in the substructure of the oxide layer through this method.

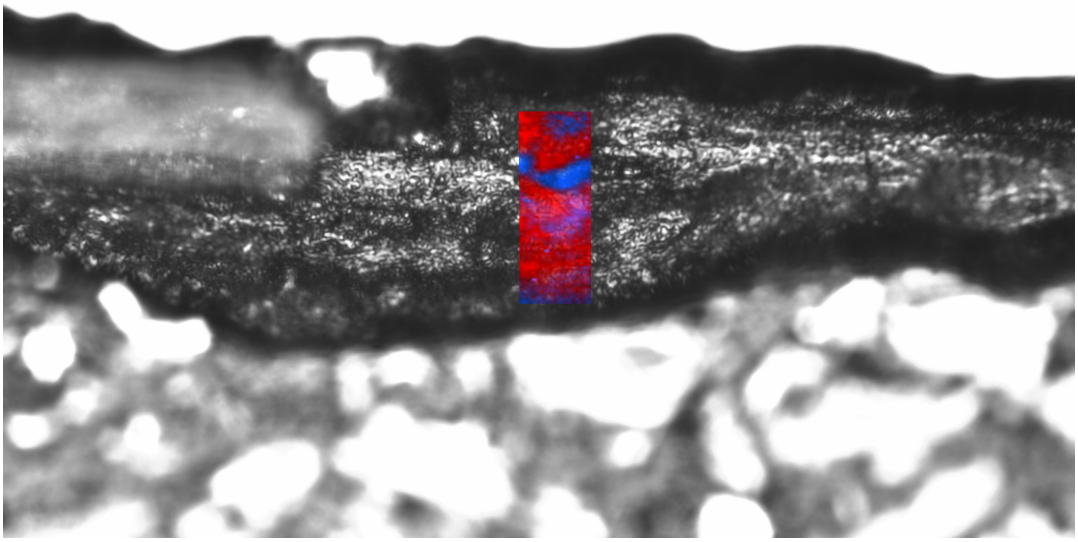

Figure 4.9: Optical image overlay showing the region of the oxide layer selected for Raman spectral mapping.

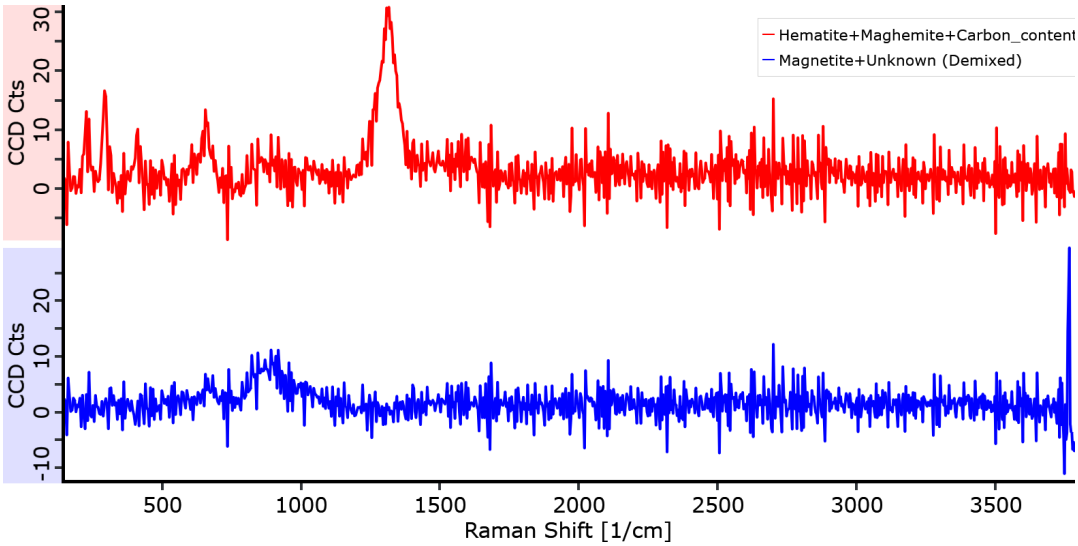

Figure 4.10: Raman spectra obtained during spectral mapping of the oxide layer interface. The high noise levels rendered peak identification difficult.

In addition to the spectra obtained from the cross-section of the oxide layer, Raman spectroscopy was also performed at three locations on the uncharged oxide layer surface (as shown in Figure 4.11). As can be seen in Figure 4.12, the peaks overlap at all the positions scanned, indicating a uniform surface composition across the sampled locations. Based on the Raman peaks identified in Table 4.7, the surface of the uncharged oxide layer consists of

a complex mixture of oxides and oxyhydroxides. The main oxides detected include haematite (α-Fe_2O_3) and magnetite (Fe_3O_4) or its closely related form, maghemite (γ-Fe_2O_3). Furthermore, the presence of peaks associated with oxyhydroxides, such as goethite (α-FeOOH) and lepidocrocite (γ-FeOOH), indicates that the surface composition includes hydroxylated phases.

Compared to the Raman spectra obtained from the cross-section of the oxide layer, surface analysis reveals additional oxyhydroxides (as shown in Figure 4.12). This discrepancy could be attributed to atmospheric exposure, where oxides on the outermost layer may undergo further oxidation, forming oxyhydroxides such as goethite and lepidocrocite. This transformation is likely the result of the interaction of moisture and oxygen in the air with the surface, promoting the gradual conversion of iron oxides to iron oxyhydroxides [120]. Consequently, the surface of the uncharged oxide layer may exhibit chemical characteristics different from those of the interior, potentially influencing its stability and behaviour under atmospheric conditions.

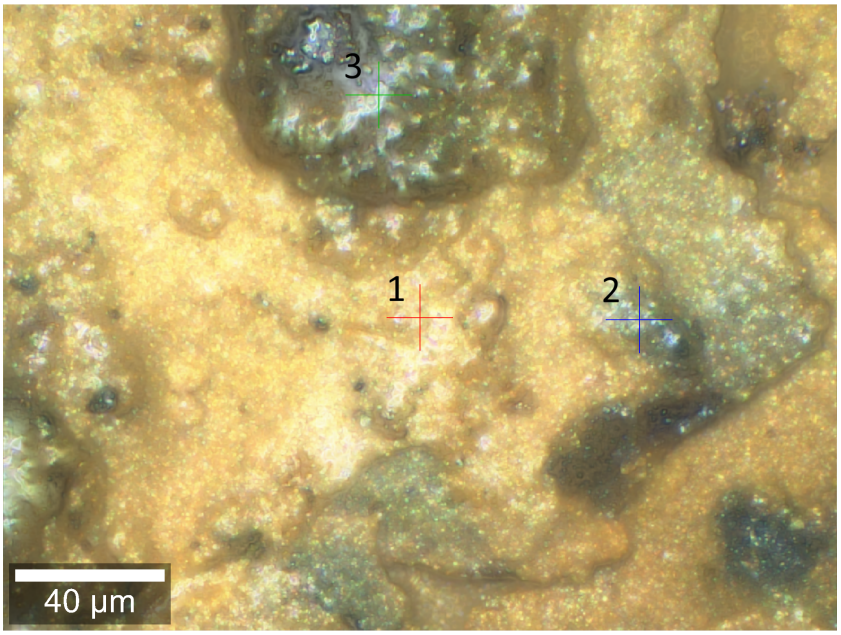

Figure 4.11: Optical micrograph showing the surface of the uncharged oxide layer, with marked locations (1, 2, and 3) indicating where Raman spectra were captured.

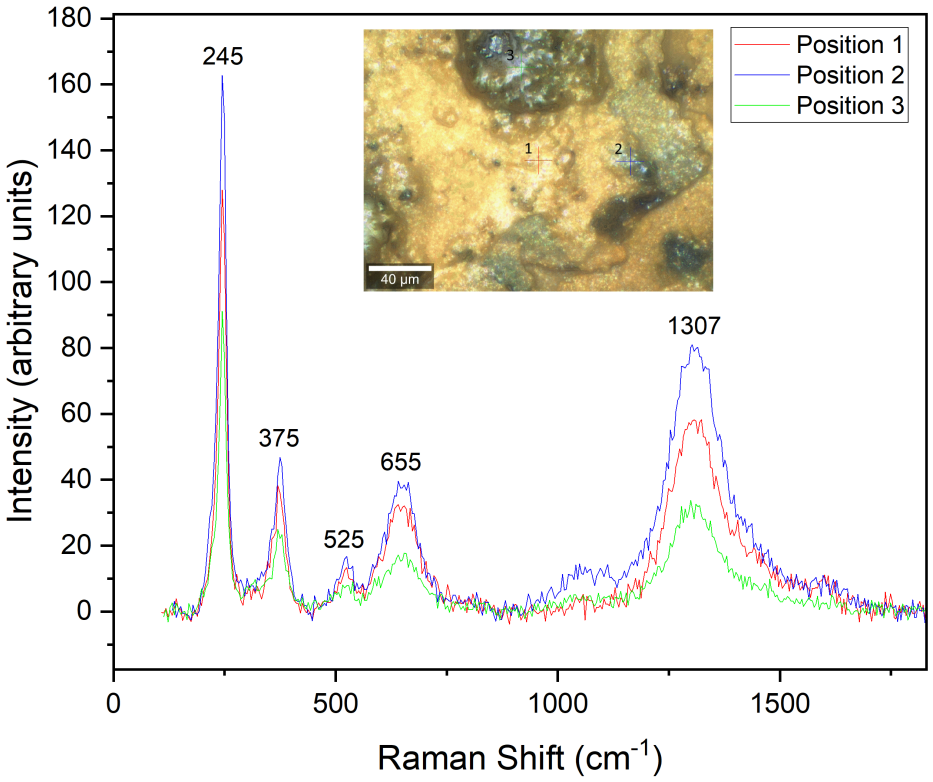

Figure 4.12: Raman spectra showing peaks at different positions, with the corresponding microscopic image inset.

Peak Positions (cm^{-1})	Compound(s)	Sources
245	α-Fe_2O_3	[116, 118]
375	α-FeOOH	[116, 119]
525	α-FeOOH / γ-FeOOH	[116, 119]
655	Fe_3O_4 / γ-Fe_2O_3	[116, 118, 119]
1307	α-Fe_2O_3	[116, 118]

Table 4.7: Raman peaks identified in the oxide layer, showing possible compounds and the sources used for identification [116, 118, 119].

4.3. Hydrogen Permeation Tests - DS Setup

The results of hydrogen permeation tests conducted under both galvanostatic (constant current) and potentiostatic (constant potential) charging conditions are presented in this section. The diffusion characteristics and barrier properties of the X65 Bare and Oxide samples are specifically evaluated based on the potentiostatic charging experiments, offering a more controlled insight into hydrogen transport behaviour.

4.3.1. Constant Current Charging - X65 Bare Sample

Figure 4.13 shows the permeation current density vs. time plot for the X65 Bare sample under constant current charging of $5.9\,\text{mA/cm}^2$. Preconditioning was performed for 18.5 hours to attain a stable background current of $0.2\,\mu\text{A/cm}^2$. During the charging step (18.5–24.5 hours), the current density rises sharply, peaking at approximately $1.2\,\mu\text{A/cm}^2$. This increase corresponds to hydrogen atoms generated on the charging side permeating through the bare steel and oxidizing on the detection side. Without an oxide barrier, hydrogen readily permeates the sample, resulting in a significant and rapid rise in current density. The potential vs. time curve during charging (as shown in Figure C.1 of Appendix C) reveals oscillations and a gradual reduction in potential, which is due to hydrogen bubble formation and coalescence on the bare steel surface. However, since this potential is not measured with respect to a reference electrode, it is not relevant to the focus of this study.

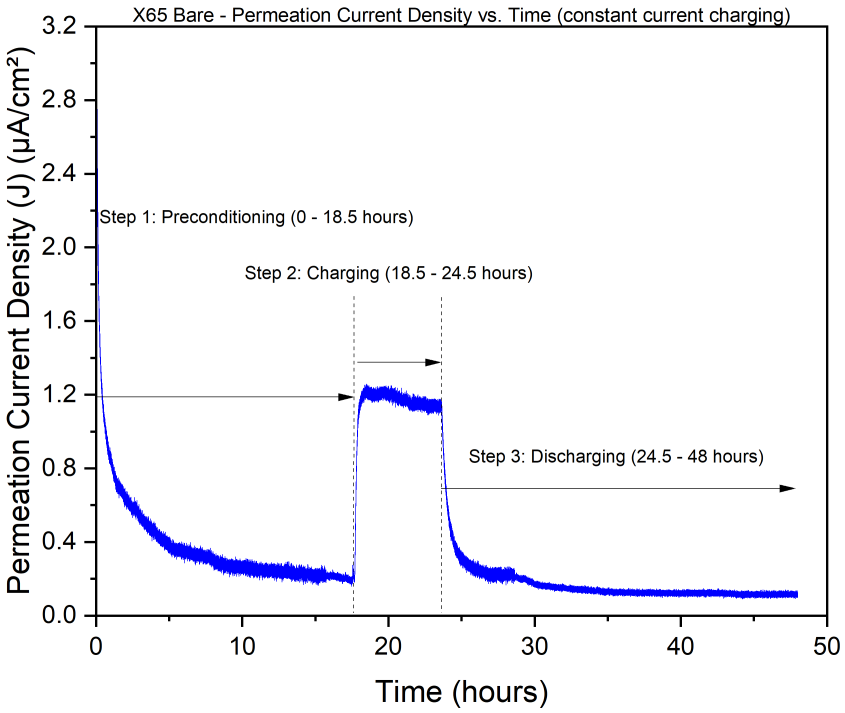

Figure 4.13: Permeation current density (J) versus time plot for the X65 bare steel sample under constant current charging of $5.9\,\text{mA/cm}^2$, showing the preconditioning (0–18.5 hours), hydrogen charging (18.5–24.5 hours), and discharging (24.5–48 hours) steps.

In the discharging step (24.5–48 hours), the current density decreases gradually as the hydro-

gen supply is cut off, ultimately reaching a baseline value of approximately $0.1\,\mu$A/cm^2. This residual current suggests that most of the permeated hydrogen has been oxidized. Additionally, anodic oxide layer growth is evident from a lower discharging current compared to the preconditioning baseline.

4.3.2. Constant Current Charging - X65 Oxide Sample

Figure 4.15 illustrates the permeation current density vs. time plot for the X65 Oxide sample under constant current charging. Although preconditioning was performed for 18.5 hours to stabilize the background current at $0.1\,\mu$A/cm^2, this step is not shown in the figure for brevity. During the charging step (0–43 hours), the current density increases steadily, reaching a peak of approximately $10\,\mu$A/cm^2 at the end of the charging period. This gradual rise reflects the slower hydrogen diffusion through the oxide layer, as the hydrogen atoms generated on the charging side permeate through the porous oxide layer and oxidize on the detection side. The potential vs. time curve during this step (Figure C.2 in Appendix C) shows a gradual decrease in the charging potential over time. However, since this potential is not measured with respect to a reference electrode, it is not directly relevant to the focus of this study.

In the discharging step (43–72 hours), the permeation current density exhibits erratic behaviour, characterized by fluctuations rather than a smooth decline. This irregular response is likely due to a delay in the detection of hydrogen atoms at the exit surface, indicative of the oxide layer's lower hydrogen diffusion coefficient compared to bare steel. The porous structure and the complex oxide/steel interface contribute to this delayed release, impeding hydrogen transport and causing the observed fluctuations in current density. This behaviour further underscores the oxide layer's role as a semi-permeable barrier, which slows down but does not entirely prevent hydrogen permeation.

However, the use of high charging currents in this test likely caused damage to the oxide layer or reduced surface oxyhydroxides such as goethite/lepidocrocite to lower valence oxides such as magnetite, leading to alterations in surface structure (see Figure 4.14). This damage may have contributed to the changes observed in the charging and discharging behaviour. Consequently, constant current charging was deemed less reliable for studying hydrogen permeation and was replaced by potential-controlled charging in subsequent experiments to minimize surface modification during hydrogen entry.

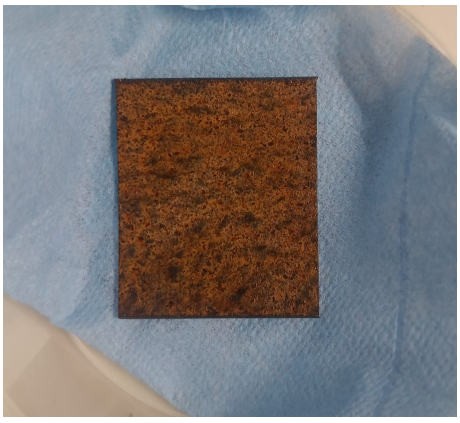

(a) X65 Oxide sample surface in uncharged condition.

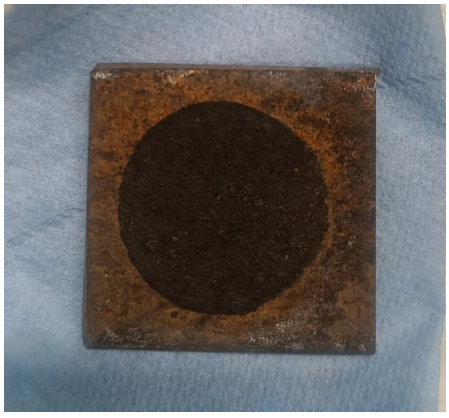

(b) X65 Oxide sample surface post-hydrogen charging.

Figure 4.14: Comparison of the X65 oxide sample conditions: (a) post-hydrogen charging and (b) uncharged condition.

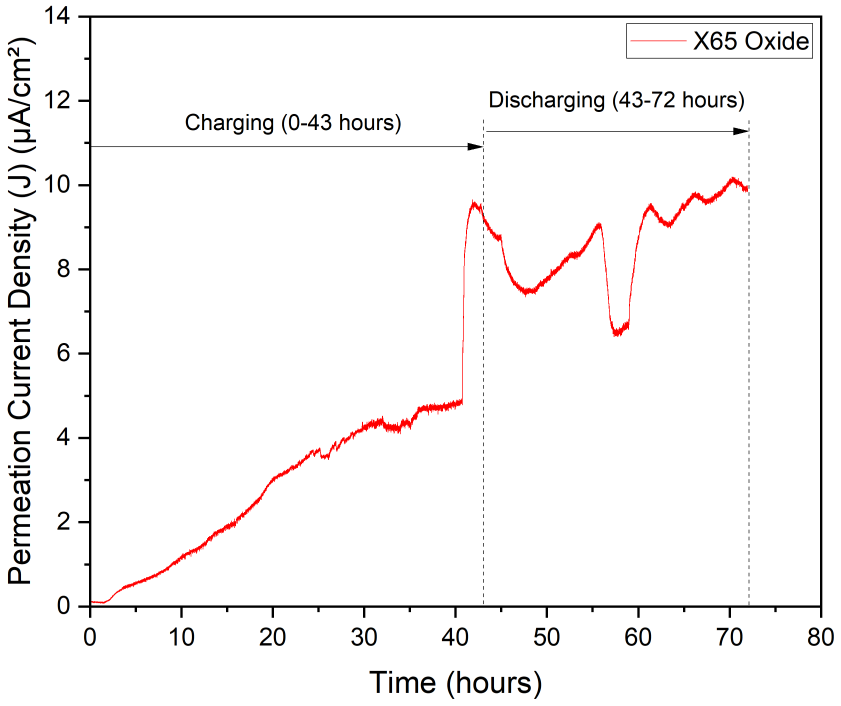

Figure 4.15: Permeation current density (J) versus time plot for the X65 Oxide sample under constant current charging, showing the charging (0–43 hours) and discharging (43–72 hours) steps.

4.3.3. Constant Potential Charging - X65 Bare Sample

Figure 4.16 illustrates the permeation current density vs. time plot for the X65 Bare sample under constant potential charging. In the initial preconditioning step (0–21 hours), the current density gradually decreases to around $0.45\ \mu$A/cm^2, indicating that the polished surface of the bare metal reaches a stable background current in the absence of active hydrogen charging. Variations in the background current density values can be attributed to differences in the thickness of the Pd layers deposited on the detection side of the samples, which in turn affect the hydrogen content within the layers.

During the charging step (21–24 hours), the oxidation current density rises sharply, reaching a peak value of approximately $2.6\ \mu$A/cm^2. This increase is attributed to the permeation of hydrogen atoms generated on the charging side, which cross through the sample and oxidize on the detection side. A gradual reduction in the permeation current density during the charging step is likely due to the growth of an anodic oxide layer on the detection side, which interferes with hydrogen oxidation and leads to incomplete hydrogen oxidation.

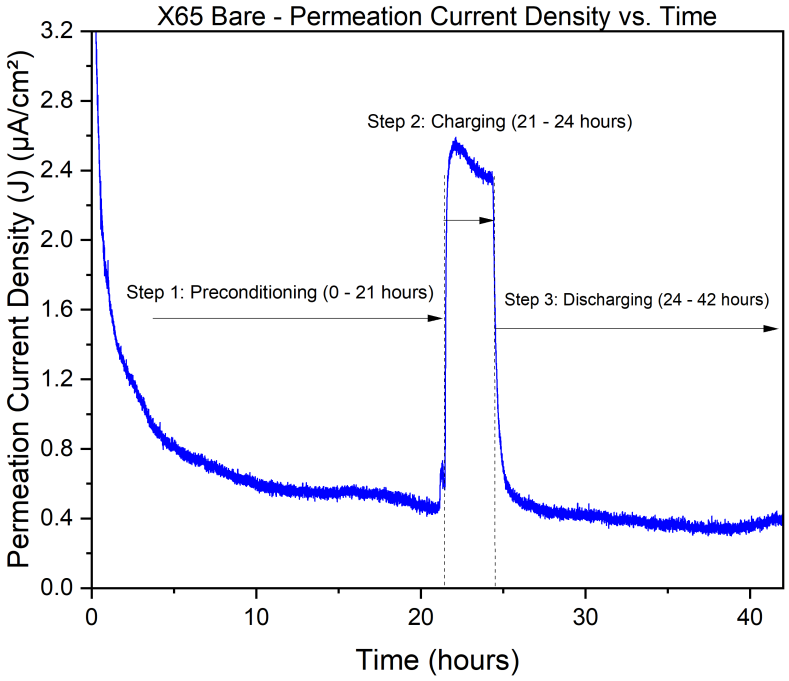

Figure 4.16: Permeation current density (J) versus time plot for the X65 Bare sample, showing the preconditioning (0–21 hours), hydrogen charging (21–24 hours), and discharging (24–42 hours) steps.

In the discharging step (24–42 hours), the current density decreases as the hydrogen supply is removed, ultimately reaching a stable value of around $0.4\,\mu$A/cm^2 after 14 hours. This final current density suggests minimal ongoing oxidation, as the system returns toward baseline conditions.

4.3.4. Constant Potential Charging - X65 Oxide Sample

Figure 4.18 illustrates the permeation current density vs. time plot for the X65 Oxide sample under constant potential charging. In the initial preconditioning step (0–18.5 hours), the current density decreases to around $0.1\,\mu$A/cm^2, indicating the stabilization of the oxide-covered surface.

During the charging step (18.5–21.5 hours), the permeation current density rises sharply, peaking at approximately $1.2\,\mu$A/cm^2. The presence of the oxide layer retards hydrogen permeation, leading to a lower value of peak permeation current density compared to the bare steel. In the discharging step (21.5–42 hours), the current density decreases but stabilizes at around $1.0\,\mu$A/cm^2. Optimization of D-S conditions will be necessary to ensure oxide layer damage is caused by hydrogen ingress alone and not by the applied charging parameters.

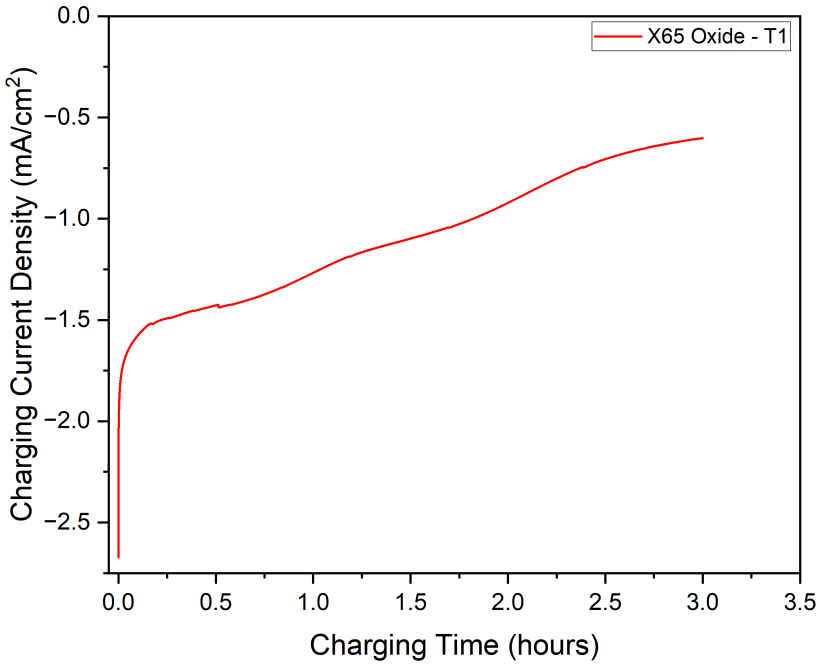

Figure 4.17: Charging current density vs. charging time for the X65 Oxide sample.

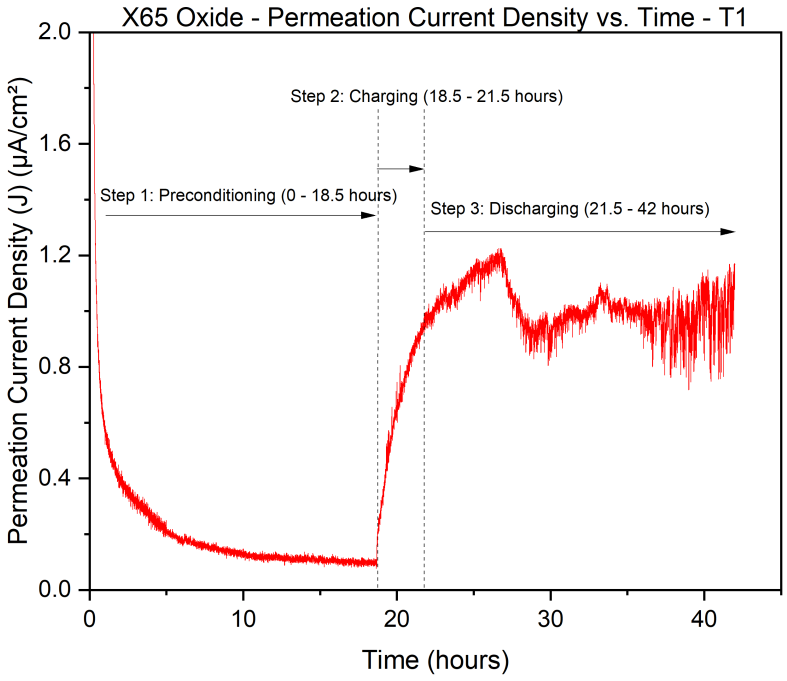

Figure 4.18: Permeation current density (J) versus time plot for the X65 Oxide sample, showing the preconditioning (0–18.5 hours), hydrogen charging (18.5–21.5 hours), and discharging (21.5–42 hours) steps.

To gain further insights into hydrogen permeation behaviour during the charging and discharging steps, a second iteration of constant potential charging was performed for the X65 Oxide sample. In this iteration, the charging duration was extended to 12 hours and the discharging period was lengthened to 45 hours, compared to the previous experiment. The permeation behaviour observed during this iteration is illustrated in Figure 4.20, while the charging current density vs. time behaviour is shown in Figure 4.19.

During the preconditioning step (0–15 hours), the permeation current density decreases and stabilizes at approximately $0.1\,\mu$A/cm^2, indicating stable surface conditions on the detection-side surface. This stabilization reflects minimal activity as the detection surface equilibrates in the electrolyte.

Figure 4.19 shows that during the charging phase (15–27 hours), the charging current density does not stabilize but instead gradually increases. The permeation current density during this charging step increases sharply, peaking at approximately $3.0\,\mu$A/cm^2, as hydrogen atoms diffuse through the steel substrate and are oxidized at the detection-side surface. The observed behaviour indicates a delay in hydrogen permeation, as the presence of the oxide layer on the entry surface influences the permeation rate.

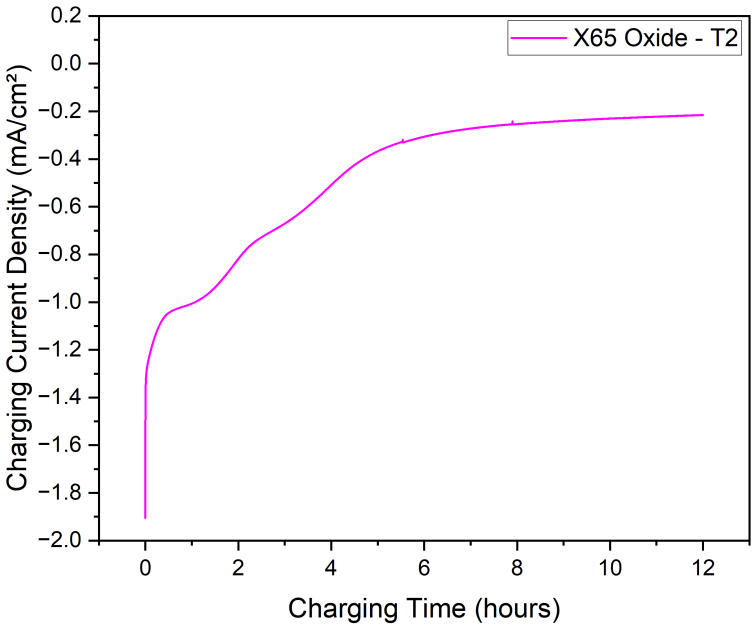

Figure 4.19: Charging current density vs. charging time for the X65 Oxide sample under potentiostatic charging.

In the discharging step (27–72 hours), the permeation current density initially rises post-charging before gradually decreasing and stabilizing at approximately $2.2\,\mu$A/cm^2. This elevated baseline compared to the preconditioning step reflects continued hydrogen release over the extended discharging period. Fluctuations in the current density during this step highlight variability in hydrogen transport or desorption rates. These results indicate that while the oxide layer delays hydrogen permeation, it does not prevent it entirely, likely due to its porous nature.

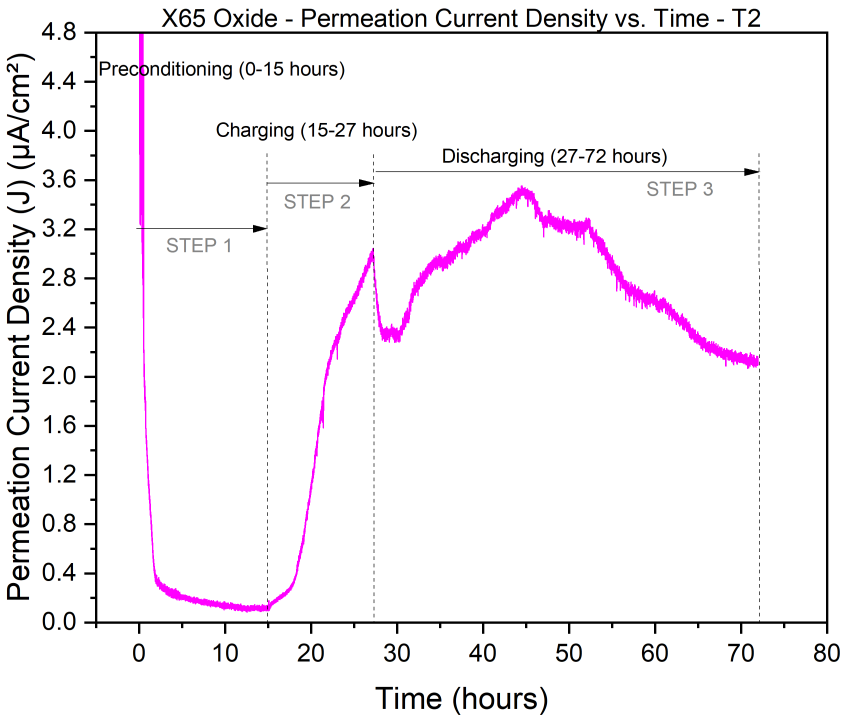

Figure 4.20: Permeation current density (J) vs. time plot for the X65 Oxide sample, showing the preconditioning (0–15 hours), hydrogen charging (15–27 hours), and discharging (27–72 hours) steps.

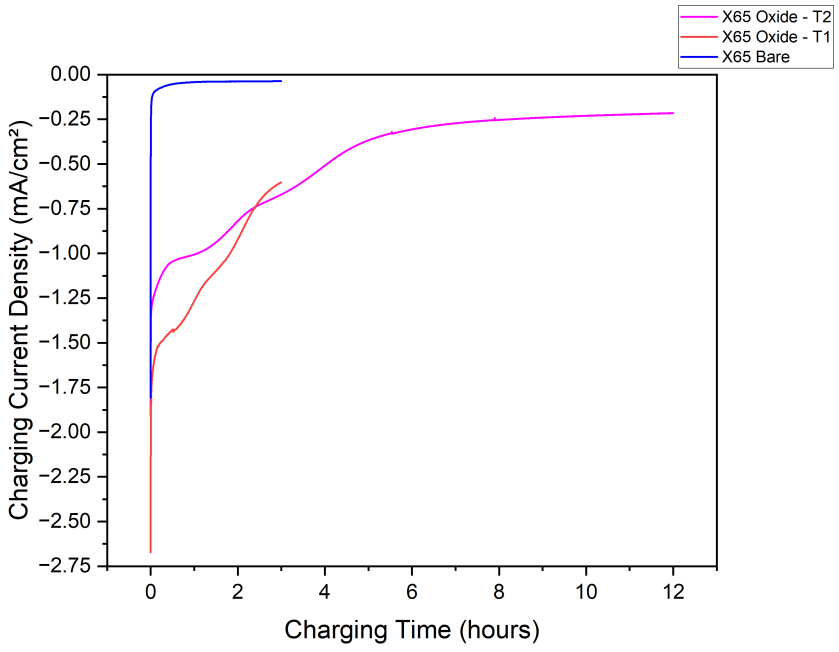

Figure 4.21: Charging current density (mA/cm^2) vs. charging time (hours) for X65 Bare and Oxide samples (Tests 1 and 2). The oxide samples exhibit higher hydrogen absorption, as indicated by the greater area under the curve compared to the bare sample.

A comparison of the charging current density profiles of the X65 Bare and Oxide samples are shown in Figure 4.21. The plot demonstrates distinct behaviours for the oxide-covered and bare samples during hydrogen charging. The oxide-covered samples (T1 and T2) exhibit significantly larger areas under the curve compared to the bare sample, indicating higher hydrogen absorption by the oxide layers.

4.3.5. Estimation of Hydrogen Diffusion Coefficient for Bare Steel/Oxide Layer

In order to estimate the diffusion coefficient of hydrogen in the oxide layer and the bare steel, a modification of the time-lag method [111, 121] is employed in order to take into account the two-layer diffusion model of our system, and the key formulas utilized are as follows:

1. Diffusion Coefficient (D_{eff}):

$$D_{\text{eff}} = \frac{L^2}{6 \cdot t_l}$$

where:

- L: Thickness of the sample (cm),
- t_l: Time lag (s), corresponding to the time at which the current density reaches 63% of the steady-state current density value I_{ss},
- D_{eff}: Apparent diffusion coefficient (cm^2/s).

2. Steady-State Flux (J_{ss}) in moles:

$$J_{\text{ss}} = \frac{I_{\text{ss}}}{F}$$

where:

- I_{ss}: Steady-state hydrogen permeation current (A/cm^2),
- F: Faraday's constant ($96485\,\text{C/mol}$).

For the X65 Bare sample:

- Thickness: $L_{\text{steel}} = 0.09\,\text{cm}$,
- Time lag: $t_l^{\text{steel}} = 391\,\text{s}$,
- Steady-state permeation current: $I_{\text{ss, steel}} = 2.15\,\mu\text{A}/\text{cm}^2$.

Using these parameters, the effective hydrogen diffusion coefficient for bare steel was calculated as $D_{\text{eff, steel}} \approx 3.46 \times 10^{-6}\,\text{cm}^2/\text{s}$, and the steady-state permeation flux was determined to be $J_{\text{ss, steel}} \approx 2.23 \times 10^{-11}\,\text{mol/cm}^2/\text{s}$.

For the first X65 Oxide sample:

- Total sample thickness: $L_{\text{oxide sample}} = 0.147\,\text{cm}$,
- Total time lag: $t_l^{\text{oxide total}} = 6500\,\text{s}$,
- Oxide layer thickness: $L_{\text{oxide}} = 0.00427\,\text{cm}$.

The steel substrate's time lag contribution for the oxide-covered sample was estimated as $t_l^{\text{steel, oxide sample}} \approx 1043\,\text{s}$. By subtracting this from the total time lag, the time lag contribution from the oxide layer was determined to be $t_l^{\text{oxide}} = 5457\,\text{s}$. The effective hydrogen diffusion coefficient for the oxide layer was calculated as $D_{\text{eff, oxide}} \approx 5.57 \times 10^{-10}\,\text{cm}^2/\text{s}$, and the steady-state permeation flux for the oxide-covered sample was $J_{\text{ss, oxide}} \approx 1.14 \times 10^{-11}\,\text{mol/cm}^2/\text{s}$.

For the second X65 Oxide sample:

- Total sample thickness: $L_{\text{oxide sample}} = 0.112\,\text{cm}$,
- Total time lag: $t_l^{\text{oxide total}} = 43200\,\text{s}$,
- Oxide layer thickness: $L_{\text{oxide}} = 0.00427\,\text{cm}$.

The steel substrate's time lag contribution for the oxide-covered sample was estimated as $t_l^{\text{steel, oxide sample}} \approx 604\,\text{s}$. Subtracting this from the total time lag, the time lag contribution from the oxide layer was calculated as $t_l^{\text{oxide}} = 42596\,\text{s}$. The effective hydrogen diffusion coefficient for the oxide layer in the second test was calculated as $D_{\text{eff, oxide}} \approx 7.13 \times 10^{-11}\,\text{cm}^2/\text{s}$, and the steady-state permeation flux was determined to be $J_{\text{ss, oxide, second}} \approx 3.01 \times 10^{-11}\,\text{mol/cm}^2/\text{s}$.

Assumptions and Considerations

The use of the modified diffusion model in this study requires the following assumptions and considerations. These assumptions simplify the analysis while ensuring that the dominant diffusion mechanisms are appropriately captured:

1. **Homogeneity of the Oxide Layer:** It is assumed that the oxide layer is uniform in thickness ($42.7\,\mu$m) and consistent in diffusion properties. Variations in thickness or porosity were not included.
2. **Negligible Interface Resistance:** The steel/oxide interface is assumed to have no significant resistance or time-lag contribution, and hydrogen trapping effects were neglected.
3. **One-Dimensional Diffusion:** Diffusion is treated as a one-dimensional process through the thickness of the sample. Edge effects or lateral diffusion are not considered.
4. **Steady-State Conditions:** The time-lag method assumes steady-state diffusion is reached before measurements are made.
5. **No Degradation of the Oxide Layer:** The oxide layer is considered stable during the experiment, without cracking, hydration, or other effects.
6. **Hydrogen Absorption Negligible in the Oxide Layer:** The oxide layer is assumed not to trap significant amounts of hydrogen, indicating all diffused hydrogen contributes to the measured flux.

The following table summarizes the hydrogen diffusion properties of bare steel and the oxide layer (for both tests):

Parameter (Units)	**Bare Steel**	**Oxide Layer (T1)**	**Oxide Layer (T2)**
Thickness, L (cm)	0.09	0.00427	0.00427
Time Lag, t_l (s)	391	5457	42596
Diffusion Coefficient, D_{eff} (cm^2/s)	3.46×10^{-6}	5.57×10^{-10}	7.13×10^{-11}
Steady-State Permeation Current, I_{ss} ($\mu\text{A}/\text{cm}^2$)	2.15	1.1	2.9
Steady-State Flux, J_{ss} ($\text{mol}/\text{cm}^2/\text{s}$)	2.23×10^{-11}	1.14×10^{-11}	3.01×10^{-11}

Table 4.8: Comparison of hydrogen diffusion properties between bare steel and oxide layers (both with $42.7\,\mu$m oxide thickness).

4.4. Electrochemical Response to Hydrogen Charging

To investigate the impact of hydrogen charging on the electrochemical behaviour of X65 steel, cyclic voltammetry (CV) and electrochemical impedance spectroscopy (EIS) were conducted on both the X65 Bare and X65 Oxide samples. These measurements were performed after a 2-hour stabilization period at open circuit potential (OCP) to ensure consistent surface conditions. The procedure was carried out under two distinct conditions: first, to evaluate the uncharged state of the samples, and later, following hydrogen permeation testing to assess the post-charging condition. This approach allowed for a direct comparison of the electrochemical responses before and after hydrogen exposure.

4.4.1. X65 Bare Sample - OCP

Figure 4.22 illustrates the variation in OCP over a period of 2 hours for the X65 Bare sample in the uncharged condition. The upward trend in OCP indicates the gradual formation of a passive film on the steel surface. This is consistent with the stabilization of the OCP observed after approximately 2 hours, suggesting that a stable and protective passive layer has formed on the surface. The passive film is likely composed of iron oxides and hydroxides, which reduce the surface's electrochemical reactivity and contribute to the observed potential stabilization. This behaviour demonstrates the natural tendency of bare steel to passivate under open-circuit conditions in the absence of hydrogen charging.

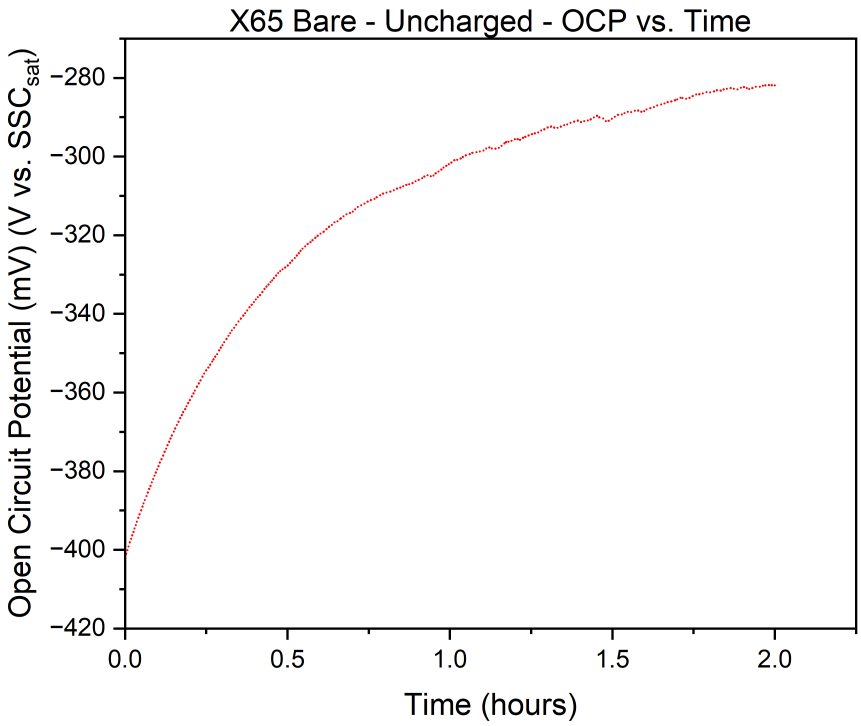

Figure 4.22: OCP vs. time for the X65 Bare sample in the uncharged condition.

Figure 4.23 illustrates the OCP vs. time plot for the X65 Bare sample in the post-charging condition. Compared to the uncharged surface (shown in Figure 4.22), which shows a steady upward trend and stabilization after 2 hours due to passive film formation, the post-charging

surface exhibits markedly different behaviour.

The initial sharp fluctuations in OCP for the post-charging surface can be attributed to transient electrochemical reactions caused by the charged surface's interaction with the electrolyte, as well as residual hydrogen desorption from the steel surface. These fluctuations are not observed in the uncharged surface, where the OCP response is smoother, reflecting a stable and intact passive layer.

The gradual shift of the OCP to more negative values over time in the post-charging condition reflects the impact of hydrogen absorbed during charging. Hydrogen ingress likely disrupted the passive layer, exposing reactive sites on the surface and contributing to continued surface reactivity. Additionally, the inability of the OCP to stabilize within the 2-hour timeframe suggests that competing processes — such as surface oxidation, hydrogen diffusion, and dissolution of the passive layer — prevent the system from achieving equilibrium. This persistent influence of hydrogen charging on the electrochemical properties of the bare steel surface contrasts with the stable passive behaviour observed for the uncharged bare steel surface.

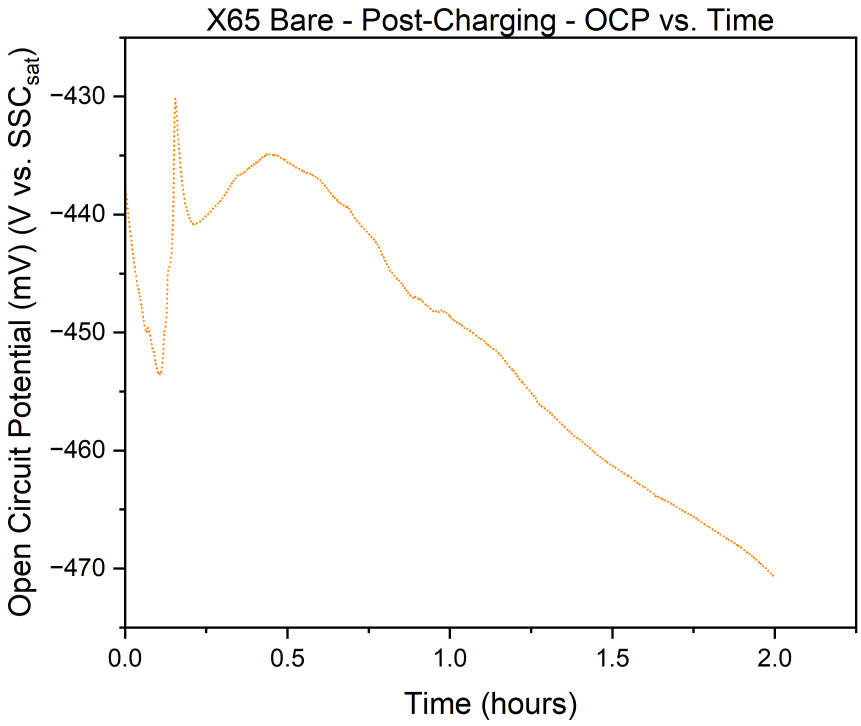

Figure 4.23: OCP vs. time for the X65 Bare sample in the post-charging condition.

4.4.2. X65 Oxide Sample - OCP

Figure 4.24 illustrates the OCP vs. time plot for the X65 Oxide sample in the uncharged condition. The OCP shows a gradual downward trend over the first 2 hours, reflecting the equilibration of the oxide layer with the electrolyte. This behaviour may be attributed to the interaction between the electrolyte and the mixed oxide composition, including haematite, magnetite, and oxyhydroxides. The oscillations observed during this period are likely due to the non-uniform and porous nature of the oxide layer, leading to localized variations in electrochemical reac-

tions. The overall trend suggests that the oxide layer undergoes chemical adjustments as it interacts with the electrolyte but reaches a relatively steady state over time.

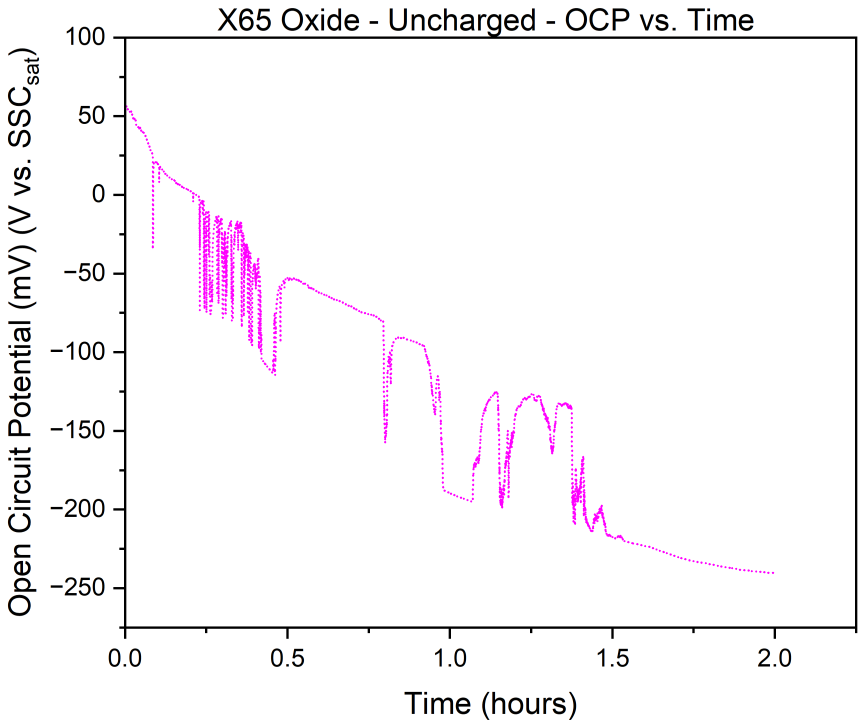

Figure 4.24: OCP vs. time for the X65 Oxide sample in the uncharged condition.

Figure 4.25 illustrates the OCP vs. time plot for the X65 Oxide sample after hydrogen charging. The behaviour of the OCP reflects the impact of hydrogen on the oxide layer. Initially, a rapid decline in OCP is observed, which can be attributed to residual hydrogen present within the oxide layer and underlying steel following the charging procedure. This decline suggests that the oxide-electrolyte interface is highly reactive due to hydrogen ingress, potentially causing localized disruptions or structural modifications within the oxide layer.

Over time, the rate of decline slows, and the OCP begins to stabilize toward a relatively constant value by the end of the monitoring period. This stabilization indicates that the system is gradually reaching a new equilibrium state, as hydrogen desorbs, redistributes, or becomes less electrochemically active. Despite this stabilization, the OCP behaviour highlights that hydrogen ingress has altered the oxide layer's electrochemical properties, maintaining an influence even as the surface reactivity decreases.

The uncharged condition (Figure 4.24) exhibits a more gradual and fluctuating trend during the measurement period, reflecting the intrinsic electrochemical response of the oxide layer in the absence of hydrogen. This comparison underscores the disruptive effect of hydrogen charging on the oxide layer, even as the system stabilizes.

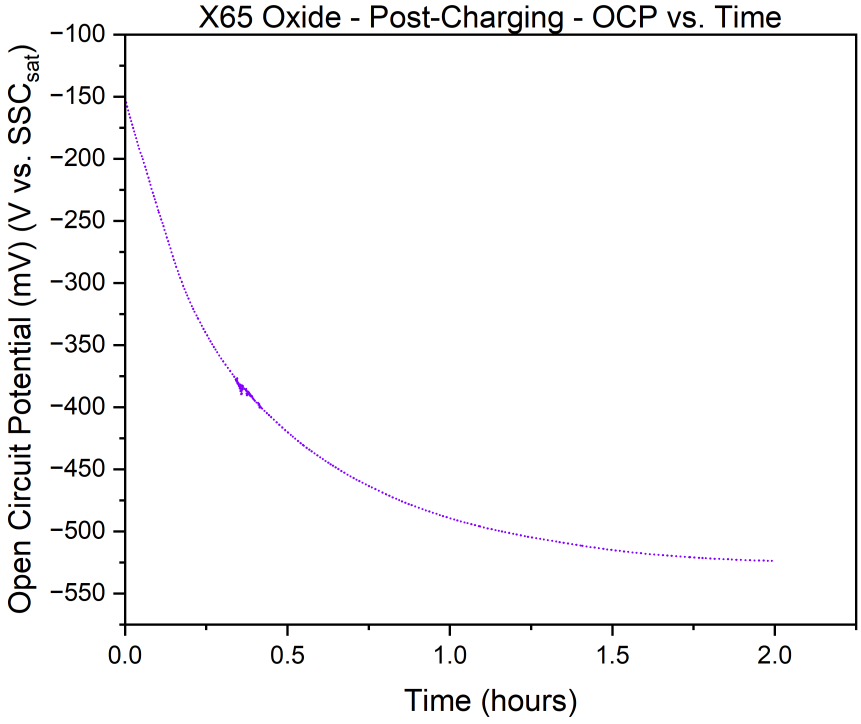

Figure 4.25: OCP vs. time for the X65 Oxide sample in the post-charging condition.

4.4.3. X65 Bare Sample - CV

CV was performed on the X65 Bare sample in both the uncharged and post-charging condition to investigate the electrochemical responses and identify key peaks corresponding to reduction and oxidation reactions. Initially, 3 cycles were performed; however, the CV was extended to 6 cycles to observe how the surface evolves in terms of the electrochemical reactions occurring, as shown in Figure 4.26. With increasing cycles, the system evolves, and noticeable changes occur in the current response due to ongoing surface modifications, including oxide formation, hydrogen adsorption, and gradual exposure of active sites.

The CV scan begins at $-1.740\,\text{V}$ vs. SSC_{sat}, proceeds to $0.160\,\text{V}$ vs. SSC_{sat}, and then reverses back to the starting potential of $-1.740\,\text{V}$ vs. SSC_{sat}. This process is repeated for 6 cycles. It must be noted that the selected region of the CV is presented in order to effectively illustrate the peak positions and their corresponding current densities.

The anodic peak A_1 observed at $-0.65\,\text{V}$ vs. SSC_{sat} corresponds to the oxidation of $Fe(OH)_2$ to Fe_3O_4, as well as the oxidation of FeO to Fe_3O_4 [122, 123]. Peak A_2 at $-0.794\,\text{V}$ vs. SSC_{sat} is attributed to the oxidation of Fe to FeO and $Fe(OH)_2$ [122]. The secondary anodic peak A_3', occurring at $-0.937\,\text{V}$ vs. SSC_{sat}, is attributed to the hydrogen desorption reaction ($H_{\text{ads}} \rightarrow H^+ + e^-$) [124, 125]. With increasing cycles, the current density of A_3' slightly increases, suggesting the evolution of hydrogen adsorption and desorption processes, likely as the system exposes new active sites or re-equilibrates.

On the cathodic side, the peak C_1 in $-0.952\,\text{V}$ vs. SSC_{sat} corresponds to the reduction of γ-Fe_2O_3 and α-FeOOH to Fe_3O_4. The peak C_2, occurring at $-1.156\,\text{V}$ vs. SSC_{sat}, is assigned to the reduction of water and the adsorption of hydrogen onto the steel surface.Furthermore,

the shoulder peak C_3', observed at approximately -0.67 V vs. SSC_{sat}, corresponds to another iron oxide reduction reaction. However, identifying the specific reaction associated with this shoulder peak proved challenging after reviewing existing literature. Further investigation is necessary to clarify the nature of this reaction.

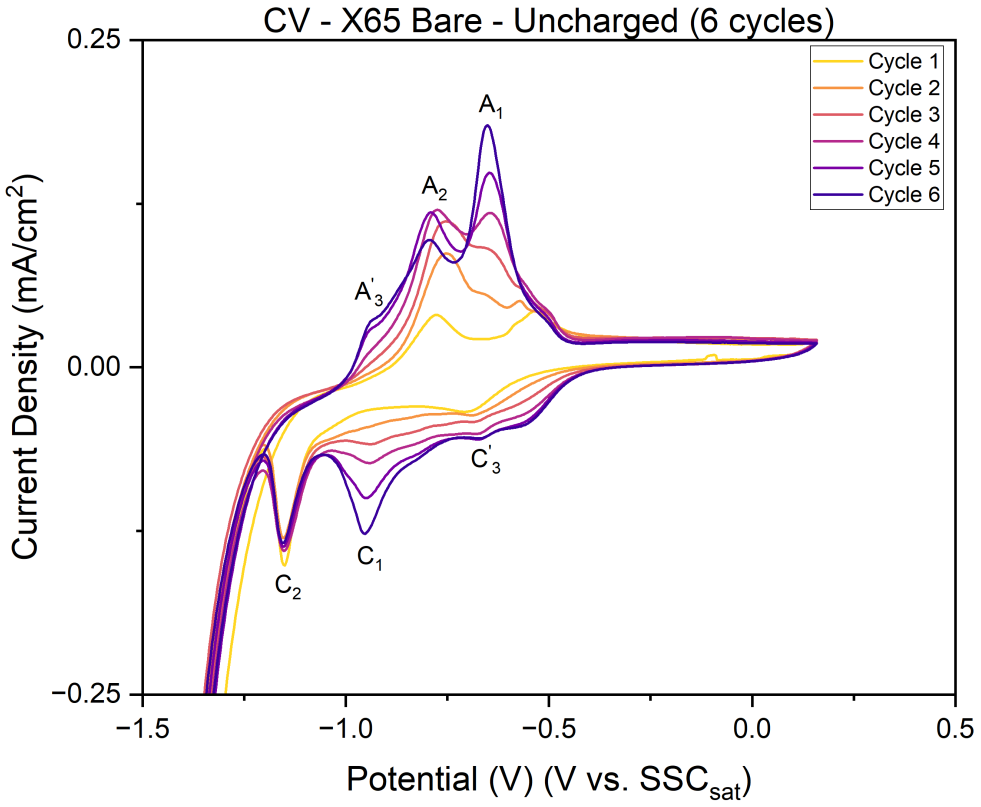

Figure 4.26: Cyclic voltammogram (CV) for X65 bare steel in uncharged condition, showing six cycles of data.

Peak Label	Potential (V vs. SSC_{sat})	Assigned Reaction
A_1	-0.65	$3Fe(OH)_2 + 2OH^- \rightarrow Fe_3O_4 + 4H_2O + 2e^-$ $3FeO + 2OH^- \rightarrow Fe_3O_4 + H_2O + 2e^-$
A_2	-0.794	$Fe + 2OH^- \rightarrow FeO + H_2O + 2e^-$ $Fe + 2OH^- \rightarrow Fe(OH)_2 + 2e^-$
A'_3	-0.937	$H_{ads} \rightarrow H^+ + e^-$
C_1	-0.952	$3\gamma\text{-}Fe_2O_3 + H_2O + 2e^- \rightarrow 2Fe_3O_4 + 2OH^-$ $3\alpha\text{-}FeOOH + e^- \rightarrow Fe_3O_4 + OH^- + H_2O$
C_2	-1.156	$H_2O + e^- \rightarrow H_{abs} + OH^-$

Table 4.9: Assignment of peaks in the CV plot to their corresponding reactions for the X65 Bare sample in the uncharged condition.

As the number of cycles increases, the current density evolves, and the peaks become more defined due to continuous surface processes. These include the formation and reduction of iron oxides, ongoing hydrogen adsorption/desorption, and changes in the electrochemical activity of the exposed surface. This evolution provides clearer insights into the underlying electrochemical mechanisms.

It should be noted that the analysis of this data is based on a single iteration of the experiment, and multiple iterations must be performed to ensure the reliability and reproducibility of the findings.

CV was also conducted for the X65 Bare samples after hydrogen charging to evaluate the influence of hydrogen charging on surface electrochemical processes. Figure 4.27 shows the CV data obtained over six cycles, where distinct anodic (A_1, A_2, and A_3') and cathodic (C_1 and C_2) peaks are observed. Compared to the uncharged condition, the system evolves differently post-hydrogen charging, as evidenced by shifts in peak potentials and changes in current density values of the peaks.

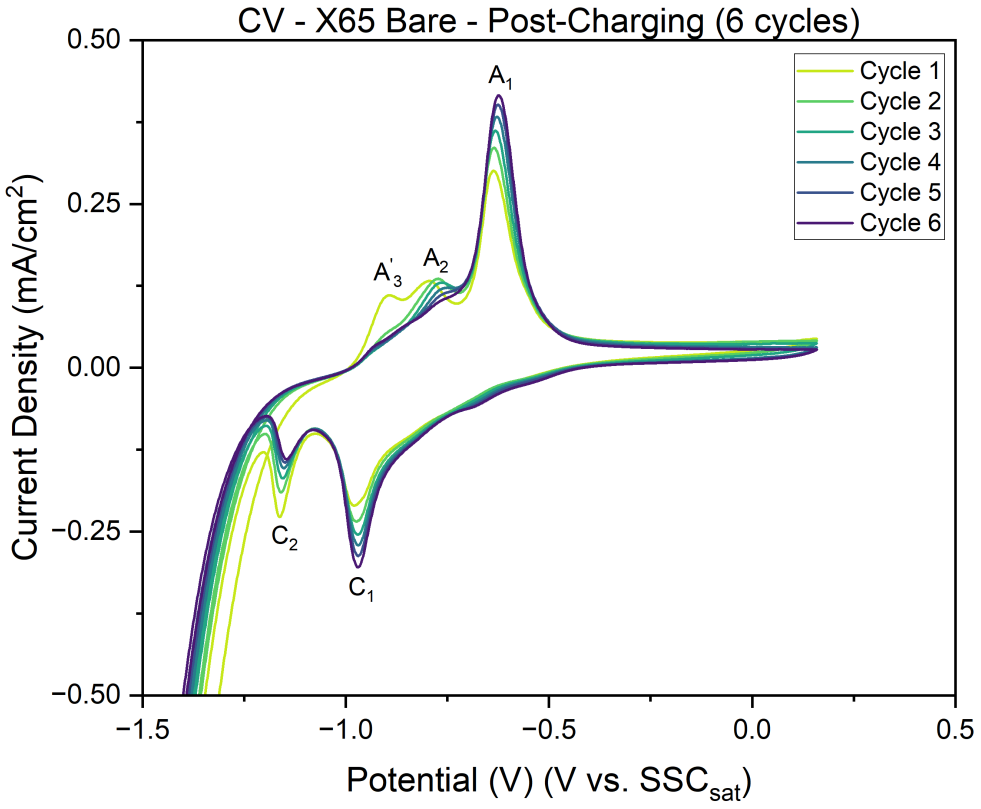

Figure 4.27: Cyclic voltammogram (CV) for X65 bare steel after hydrogen charging, showing six cycles of data.

The anodic peak A_1 at -0.637 V vs. SSC_{sat} corresponds to the oxidation of $Fe(OH)_2$ and FeO to Fe_3O_4 [122, 123]. Peak A_2 at -0.795 V vs. SSC_{sat} represents the oxidation of Fe to FeO and $Fe(OH)_2$. The anodic peak A_3', occurring at -0.893 V vs. SSC_{sat}, is attributed to the hydrogen desorption reaction ($H_{ads} \rightarrow H^+ + e^-$). In contrast to the uncharged condition, the current density of A_3' decreases with increasing cycles, indicating a reduction in hydrogen desorption

activity as hydrogen diffuses out of the steel and fewer adsorbed hydrogen species remain.

On the cathodic side, peak C_1 at -0.979 V vs. SSC_{sat} corresponds to the reduction of γ-Fe_2O_3 and α-FeOOH to Fe_3O_4. Peak C_2, occurring at -1.163 V vs. SSC_{sat}, is associated with the reduction of water and hydrogen adsorption onto the steel surface ($H_2O + e^- \rightarrow H_{ads} + OH^-$).

With increasing cycles, the current density increases across all peaks compared to the uncharged condition, reflecting heightened electrochemical activity. This evolution is attributed to hydrogen-induced changes on the steel surface, such as loss of passivation, increased reactivity, and exposure of new active sites. The decline in the current density of the peak A_3' indicates the gradual depletion of hydrogen from the steel surface over repeated cycles, highlighting the transient nature of hydrogen desorption post-charging.

Peak Label	Potential (V vs. SSC_{sat})	Assigned Reaction
A_1	-0.637	$3Fe(OH)_2 + 2OH^- \rightarrow Fe_3O_4 + 4H_2O + 2e^-$ $3FeO + 2OH^- \rightarrow Fe_3O_4 + H_2O + 2e^-$
A_2	-0.795	$Fe + 2OH^- \rightarrow FeO + H_2O + 2e^-$ $Fe + 2OH^- \rightarrow Fe(OH)_2 + 2e^-$
A'_3	-0.893	$H_{ads} \rightarrow H^+ + e^-$
C_1	-0.979	3γ-$Fe_2O_3 + H_2O + 2e^- \rightarrow 2Fe_3O_4 + 2OH^-$ 3α-$FeOOH + e^- \rightarrow Fe_3O_4 + OH^- + H_2O$
C_2	-1.163	$H_2O + e^- \rightarrow H_{abs} + OH^-$

Table 4.10: Assignment of peaks in the CV plot to their corresponding reactions for the X65 Bare sample in the post-charging condition.

The CV results for the X65 Bare sample compare the sixth cycle of data obtained under uncharged and post-hydrogen charging conditions, as shown in Figure 4.28. The uncharged condition (red curve) exhibits distinct anodic and cathodic peaks, corresponding to the oxidation and reduction reactions occurring at the steel surface. Notably, post-hydrogen charging (blue curve) reveals an increase in current density for both anodic and cathodic peaks, which is indicative of heightened electrochemical activity due to hydrogen ingress.

The anodic peaks (A_1 and A_2) show slight shifts in potential and increased current density post-charging, suggesting that hydrogen charging alters the surface chemistry, possibly exposing additional reactive sites or modifying the passive layer. Similarly, the cathodic peaks (C_1 and C_2) exhibit higher current density values post-charging, consistent with an increased reduction activity due to the presence of absorbed hydrogen. These trends highlight the significant impact of hydrogen charging on the electrochemical behaviour of steel, characterized by a more reactive and destabilized surface. A detailed analysis of these trends and their implications will be discussed in the following chapter.

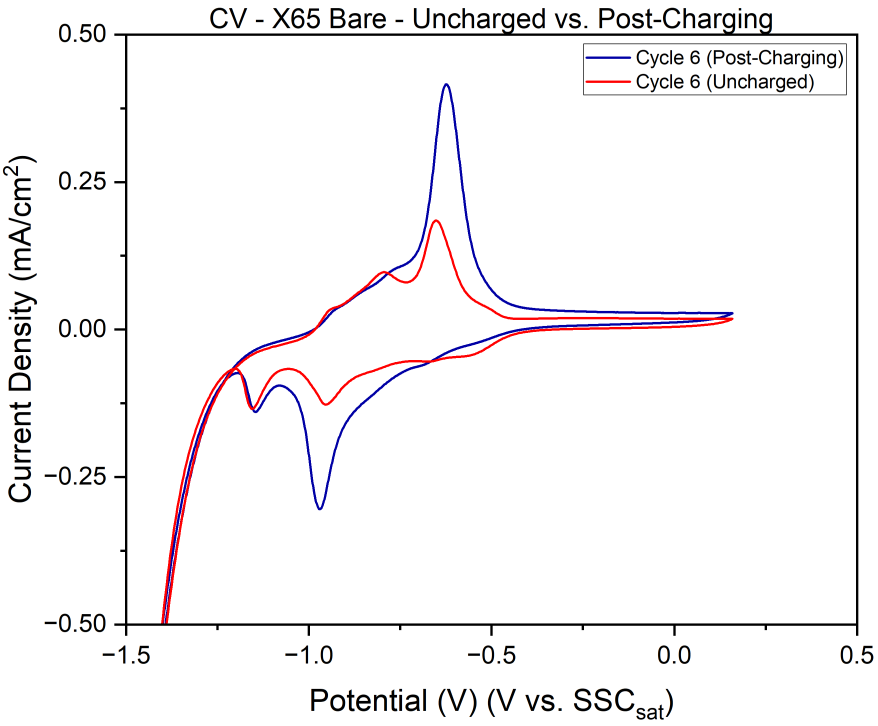

Figure 4.28: CV comparison of X65 Bare samples in the uncharged (cycle 6, red) and post-charging condition (cycle 6, blue). The graph shows a notable increase in current density values post-charging.

4.4.4. X65 Oxide Sample - CV

Figure 4.29 shows the cyclic voltammogram (CV) for the X65 Oxide sample under uncharged conditions, recorded over three cycles. The voltammogram reveals an unstable and poorly defined cyclic response across the potential range, particularly in the cathodic scan region associated with the hydrogen evolution reaction (HER).

The instability observed in the CV can be attributed to the high resistance of the thick oxide layer ($42.7\,\mu$m), which impedes efficient charge transfer at the electrode/electrolyte interface. Additionally, the structural heterogeneity and presence of defects within the oxide layer likely contribute to the inconsistent current density behaviour observed across cycles. These characteristics hinder the formation of a well-defined voltammogram for the oxide-covered sample.

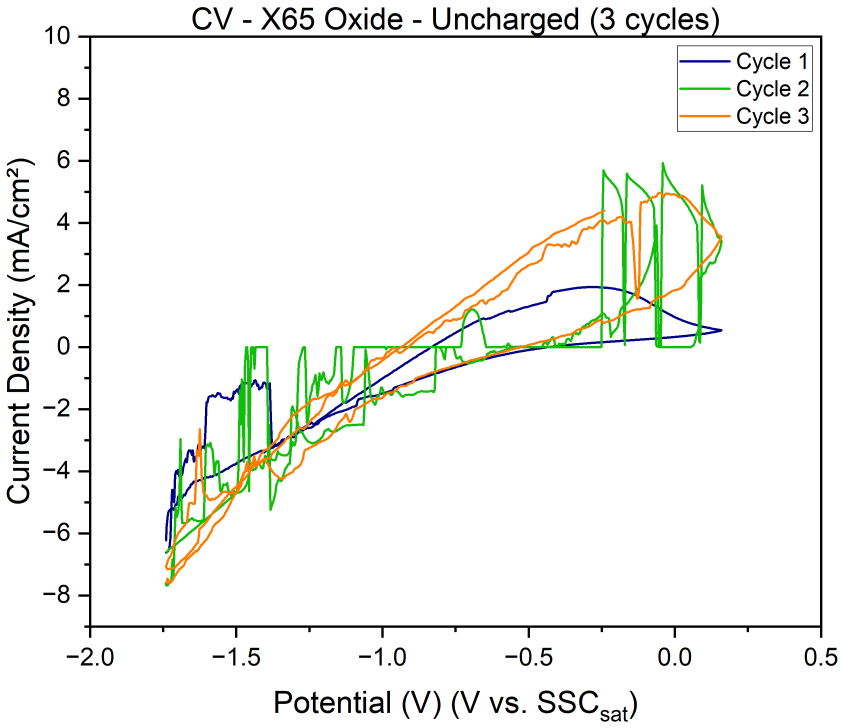

Figure 4.29: Cyclic voltammogram (CV) for the X65 Oxide sample under uncharged conditions, recorded over three cycles.

EIS was performed on the X65 Bare and X65 Oxide samples in 0.1 M NaOH + 3 g/L NH_4SCN (the hydrogen charging solution used in the DS experiments) to evaluate corrosion resistance and electrochemical behaviour before and after hydrogen charging. Nyquist and Bode plots were analysed for each condition to extract key parameters such as charge transfer resistance and double-layer capacitance. These plots provide complementary information about how hydrogen ingress influences the corrosion resistance of both sets of steel samples.

4.4.5. X65 Bare Sample − EIS

The Nyquist plot for the uncharged condition (shown in Figure 4.32) shows an incomplete semicircular appearance, characteristic of charge transfer processes at the steel-electrolyte interface. The large arc diameter indicates high corrosion resistance and the presence of a stable passive film [126], which minimizes charge transfer at the interface. The high-frequency region of the Nyquist plot corresponds to the charge transfer resistance (R_1) and capacitance (C_1), which together describe the electrochemical properties of the steel in its passive state. The fitting was performed using the equivalent electrical circuit (EEC) model shown in Figure 4.30. Capacitance values for C_1 are calculated using the resistance R_1, and constant phase element values $CPE1-T$ and $CPE1-P$, with the Hsu and Mansfeld formula [127], where $CPE1-T$ is Q and $CPE1-P$ is n.

$$C = Q^{\frac{1}{n}} \left(R^{1-n}\right)^{\frac{1}{n}}$$

The fitting results indicate that the charge transfer resistance (R_1) is $193,270\,\Omega\cdot\text{cm}^2$, reflecting the strong surface protection provided by the passive film. The double-layer capacitance (C_1) is calculated as $10.82\,\mu\text{F/cm}^2$. The phase angle exponent (n) is 0.927, suggesting near-ideal capacitive behaviour and minimal surface irregularities.

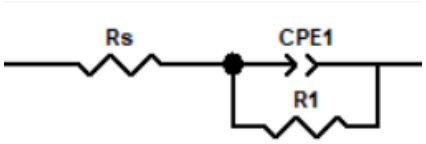

Figure 4.30: EEC model utilized for representing the electrochemical response of X65 Bare sample in 0.1 M NaOH + 3 g/L NH_4SCN.

In addition, an alternative EEC model, as shown in Figure 4.31, was tested. However, the fitting results were poor, indicating the inadequacy of the model in representing the electrochemical behaviour of the X65 Bare sample.

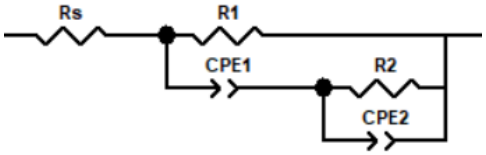

Figure 4.31: Attempted EEC model used to represent the electrochemical response of X65 Bare sample in 0.1 M NaOH + 3 g/L NH_4SCN.

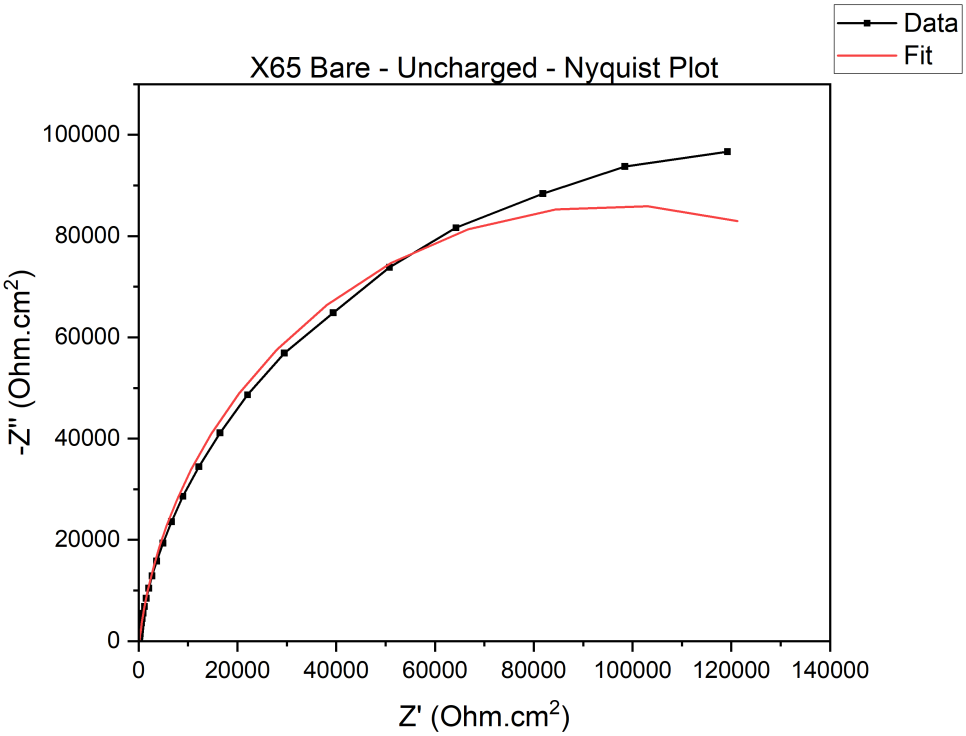

Figure 4.32: Nyquist plot for uncharged X65 bare steel, showing experimental data (black markers) and fitted results (red curve).

The Bode magnitude plot (shown in Figure 4.33) illustrates the variation of the impedance magnitude ($|Z|$) with frequency and provides insight into the overall resistance and capacitive behaviour of the system across a wide frequency range. In this graph, the high frequency region is dominated by the bulk properties of the electrolyte and the resistance of the steel surface, while the low frequency region is governed by processes such as charge transfer and diffusion. The gradual slope at intermediate frequencies is attributed to the double-layer capacitance and resistance of the passive film, highlighting the capacitive contributions at the interface. The high impedance observed at low frequencies under this condition reflects a stable passive film and strong charge transfer resistance.

The corresponding Bode phase angle plot (shown in Figure 4.34) shows a phase angle minimum of approximately $-80°$, characteristic of dominant capacitive behaviour. The smooth transition of the phase angle from capacitive to resistive behaviour at high frequencies indicates the stability of the electrochemical interface. These features confirm the presence of a well-defined and homogeneous double-layer structure, aligning with the high R_1 and C_1 values obtained from the Nyquist plot fitting.

It must be noted that analysis of this data is based on a single iteration of the experiment, and multiple iterations must be performed to ensure reliability and reproducibility of the findings.

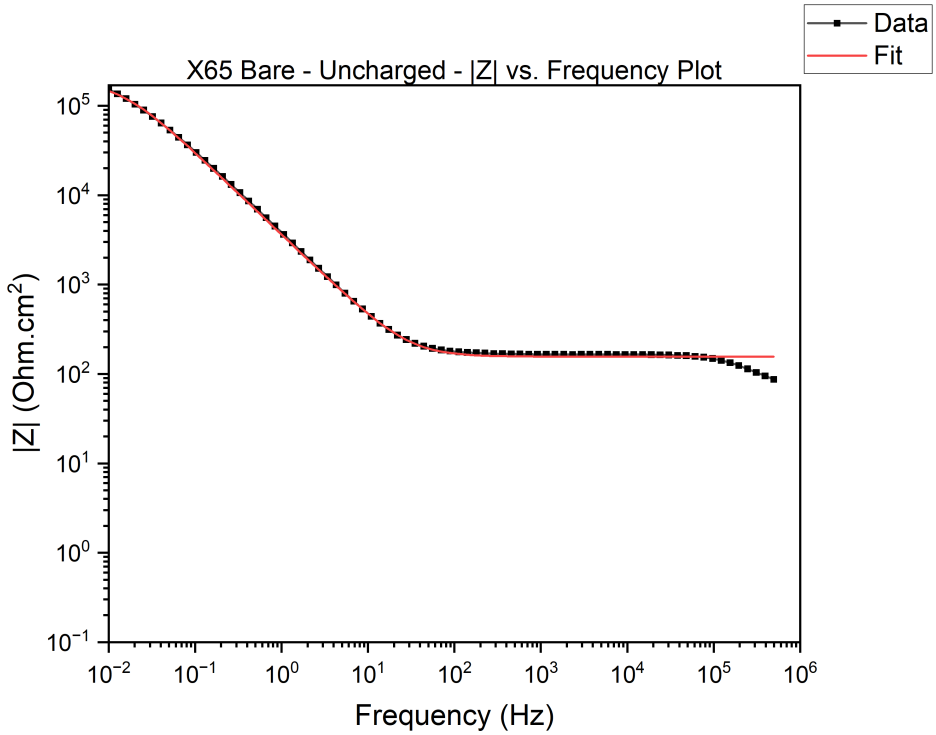

Figure 4.33: Bode magnitude plot for uncharged X65 bare steel, showing experimental data (black markers) and fitted results (red curve).

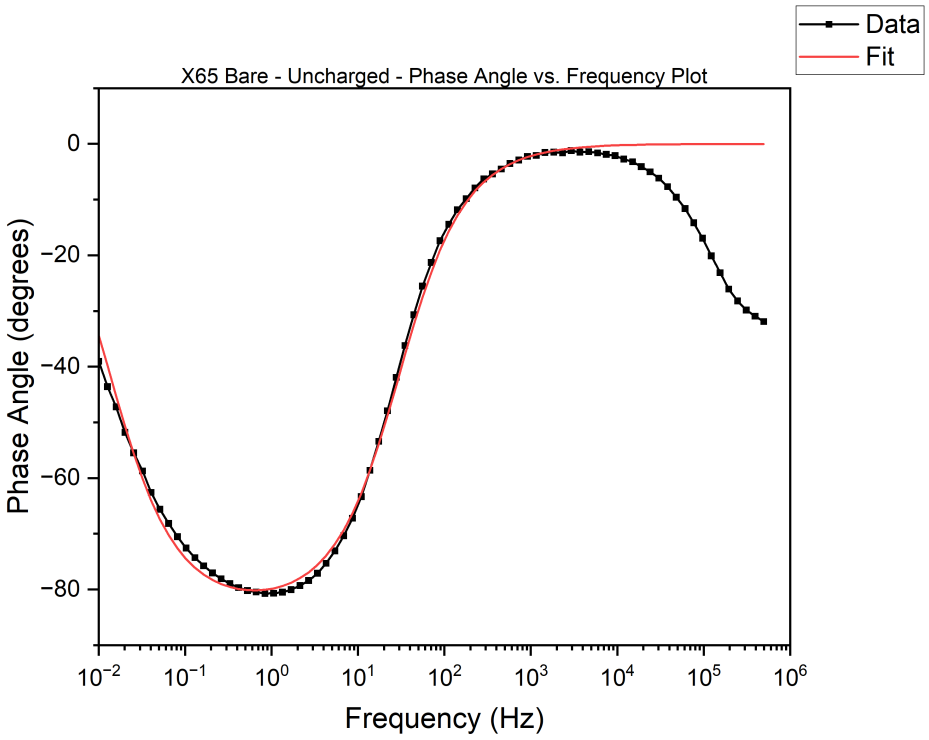

Figure 4.34: Bode phase angle plot for uncharged X65 bare steel, showing experimental data (black markers) and fitted results (red curve).

The Nyquist plot for the post-charging condition (Figure 4.35) shows a much smaller semicircular arc compared to the uncharged condition, indicating a significant reduction in charge transfer resistance. The smaller arc diameter reflects the degradation of the passive layer caused by hydrogen ingress. The fitting results reveal that the charge transfer resistance (R_1) decreases to $9,133\,\Omega{\cdot}\text{cm}^2$, highlighting the loss of surface protection and increased susceptibility to corrosion. The double-layer capacitance (C_1) also decreases to $3.98\,\mu\text{F/cm}^2$, indicating a less stable electrochemical interface. The phase angle exponent (n) is reduced to 0.812, suggesting increased surface irregularities and a deviation from ideal capacitive behaviour.

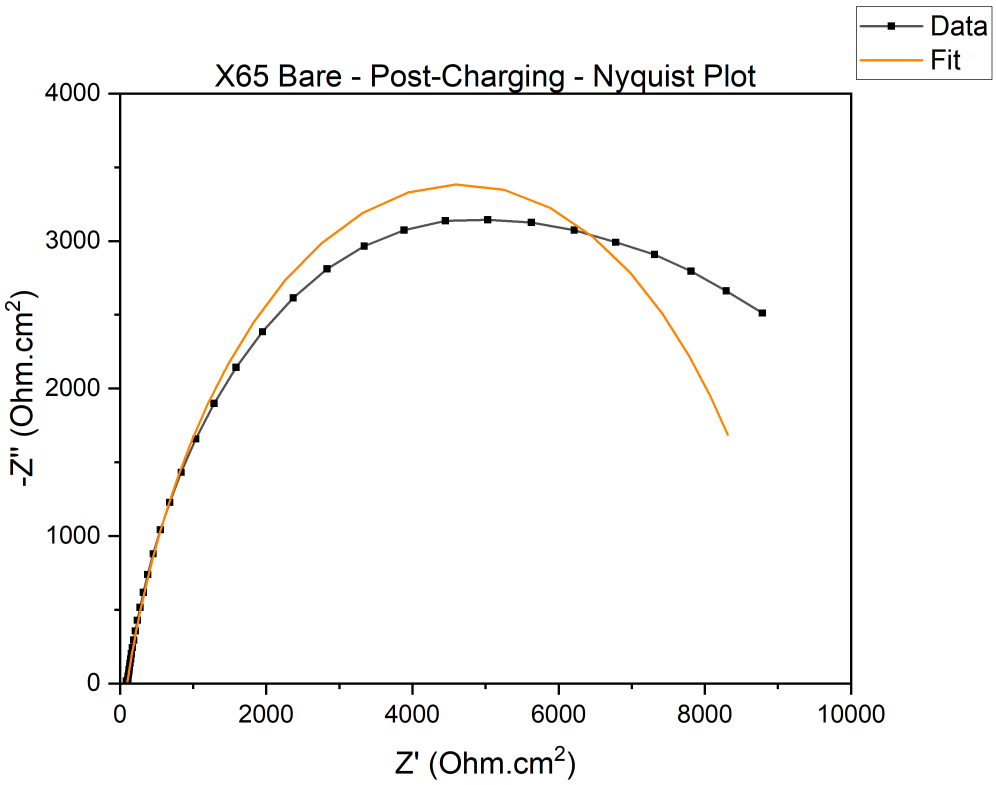

Figure 4.35: Nyquist plot for post-charging X65 bare steel, showing experimental data (black markers) and fitted results (orange curve).

The Bode magnitude plot (shown in Figure 4.36) demonstrates a marked reduction in impedance ($|Z|$) values at low frequencies compared to the uncharged condition. This reduction indicates a weaker charge transfer resistance and degradation of the passive layer. The slope at intermediate frequencies is steeper, reflecting diminished capacitive contributions at the interface. At high frequencies, the impedance values are similar to those in the uncharged condition, indicating that bulk properties are not significantly affected by hydrogen ingress.

The corresponding Bode phase angle plot (shown in Figure 4.37) shows a reduced phase angle minimum of approximately $-70°$, indicating a diminished capacitive response. The transition frequency at which the phase angle shifts from capacitive to resistive behaviour is also shifted to lower frequencies, consistent with increased time constants for charge-transfer processes. These features confirm the degradation of the passive layer and reduced electrochemical stability of the steel after hydrogen charging.

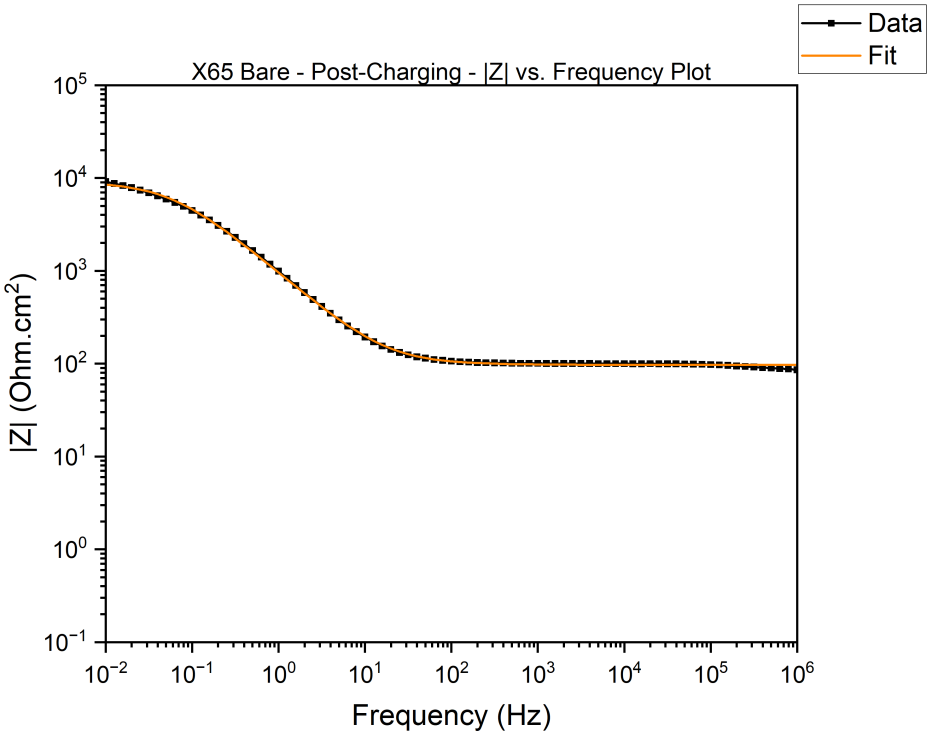

Figure 4.36: Bode magnitude plot for post-charging X65 bare steel, showing experimental data (black markers) and fitted results (orange curve).

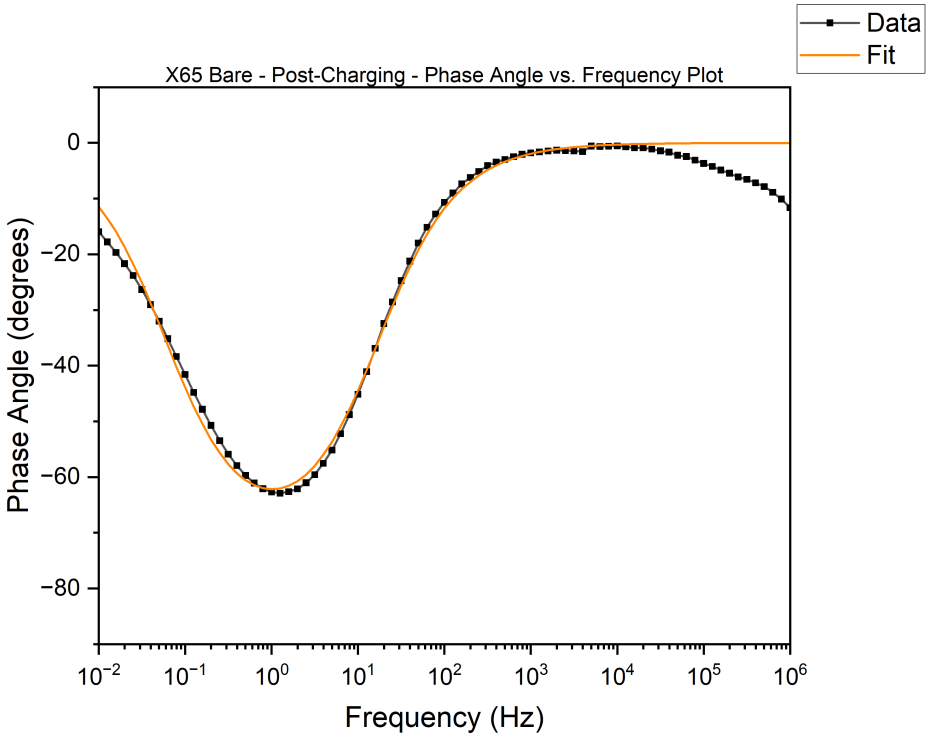

Figure 4.37: Bode phase angle plot for post-charging X65 bare steel, showing experimental data (black markers) and fitted results (orange curve).

Comparison of Nyquist and Bode graphs for uncharged and post-charging conditions highlights the detrimental impact of hydrogen ingress on the electrochemical stability of X65 bare steel. The Nyquist plot shows a significant reduction in charge transfer resistance (R_1) from $193,270\,\Omega\cdot\text{cm}^2$ in the uncharged condition to $9,133\,\Omega\cdot\text{cm}^2$ in the post-charging condition. This decrease corresponds to a substantial decrease in stability of the passive layer. Similarly, the double-layer capacitance (C_1) decreases from $10.82\,\mu$F/cm^2 to $3.98\,\mu$F/cm^2, reflecting the disruption of the electrochemical interface. The Bode magnitude plots complement these results, showing significantly reduced impedance at low frequencies after charging, while the phase angle plots reveal a decrease in the minimum phase angle from $-80°$ to $-70°$. These findings confirm that hydrogen ingress compromises the passive layer, significantly reducing the corrosion resistance and electrochemical stability of X65 bare steel.

Sample	Element	Value	Error (%)	Chi-Squared
Bare (Uncharged)	R_s	155.9 $\Omega\cdot$cm^2	1.89	0.014
	CPE1-T	5.03E-5	2.47	
	CPE1-P	0.926	0.90	
	C_1 (Calculated)	10.82 μF/cm^2	–	
	R_1	193270 $\Omega\cdot$cm^2	7.92	
Bare (Post-Charging)	R_s	97.02 $\Omega\cdot$cm^2	0.672	0.0019
	CPE1-T	3.2665E-4	1.36	
	CPE1-P	0.812	0.58	
	C_1 (Calculated)	3.98 μF/cm^2	–	
	R_1	9133 $\Omega\cdot$cm^2	1.88	

Table 4.11: Fit parameters for the equivalent circuit model for the bare sample, including the Chi-squared values and calculated capacitance (C_1) for both uncharged and post-charging conditions.

4.4.6. X65 Oxide Sample - EIS

The Nyquist plot for the uncharged X65 oxide sample (shown in Figure 4.38) exhibits a semicircular arc, indicative of charge transfer processes at the interface of the oxide layer and the electrolyte. The large arc diameter suggests that the oxide layer provides significant resistance to charge transfer, reflecting its protective properties. Attempts were made to fit the experimental data using various equivalent electrical circuit (EEC) models, but an ideal fit could not be identified. This outcome highlights the complex electrochemical behaviour of the oxide layer, which may involve multiple overlapping processes that are challenging to represent using standard circuit elements.

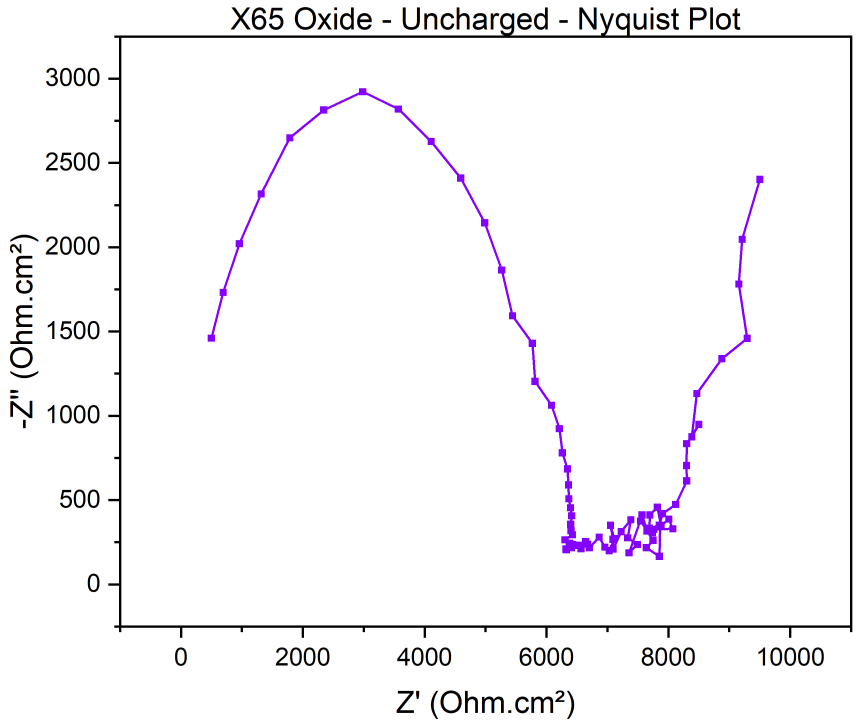

Figure 4.38: Nyquist plot ($-Z''$ vs. Z') for the X65 oxide sample before hydrogen charging.

The Bode magnitude plot (shown in Figure 4.39) reveals a high impedance ($|Z|$) across all frequency ranges, with particularly elevated values at low frequencies. This behaviour reinforces the Nyquist findings, indicating effective protection provided by the oxide layer. The gradual slope at intermediate frequencies corresponds to the capacitive contributions of the oxide layer, while the low-frequency plateau represents the system's resistance to charge transfer.

The phase angle plot (shown in Figure 4.40) shows a maximum phase angle close to $-85°$ at intermediate frequencies, further confirming dominant capacitive behaviour. The smooth transition of the phase angle from resistive to capacitive behaviour at different frequencies supports the protective role of the oxide layer in minimizing electrochemical activity at the interface.

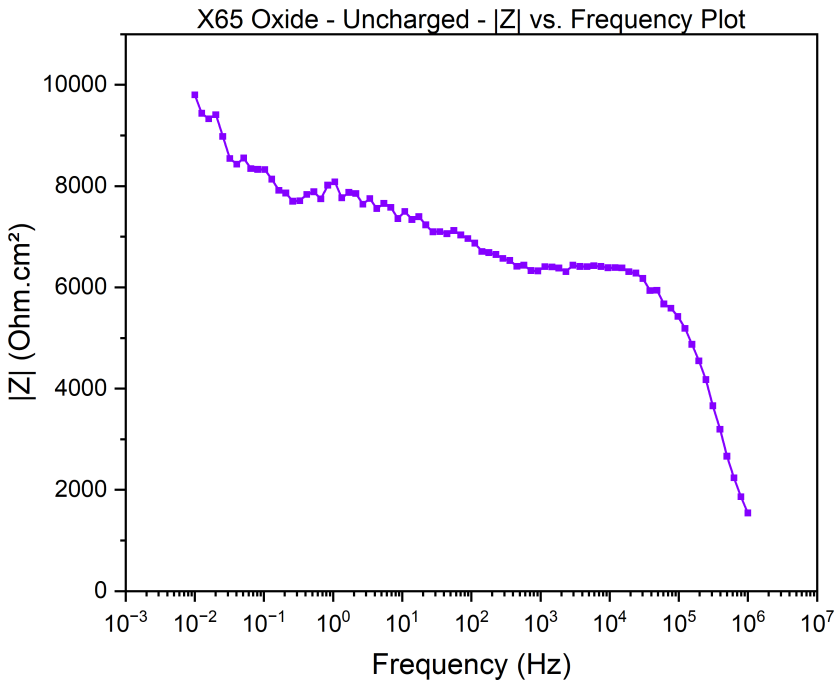

Figure 4.39: Bode magnitude plot ($|Z|$ vs. Frequency) for the X65 oxide sample before hydrogen charging.

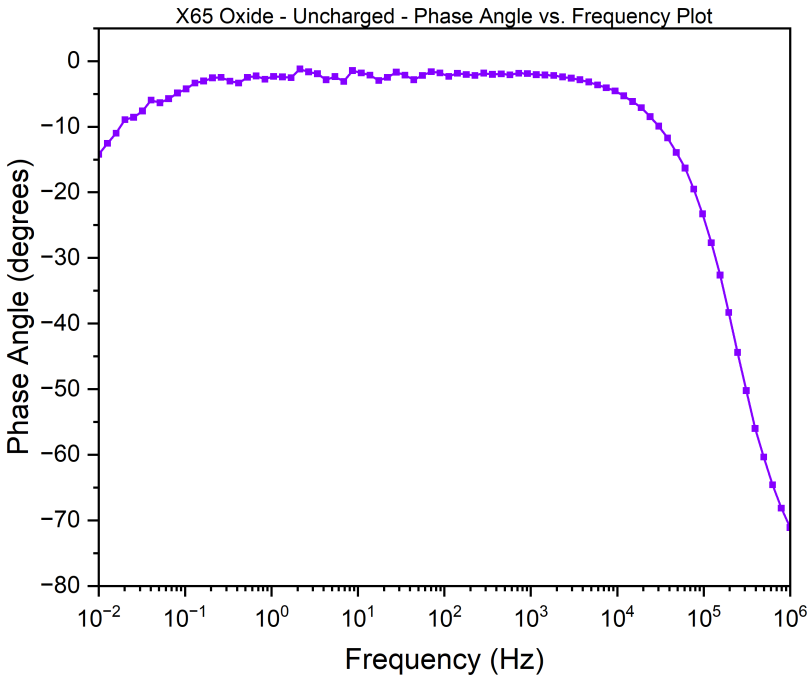

Figure 4.40: Bode phase angle plot (Phase Angle vs. Frequency) for the X65 oxide sample before hydrogen charging.

The Nyquist plot for the oxide sample after hydrogen charging (Figure 4.41) exhibits a reduced semicircular arc compared to the uncharged condition, signifying a decrease in charge transfer resistance. This reduction suggests that hydrogen ingress compromises the protective properties of the oxide layer. Attempts to fit the post-charging data using multiple EEC models were similarly inconclusive, indicating that the hydrogen-induced changes in the oxide layer create additional complexities in the electrochemical response.

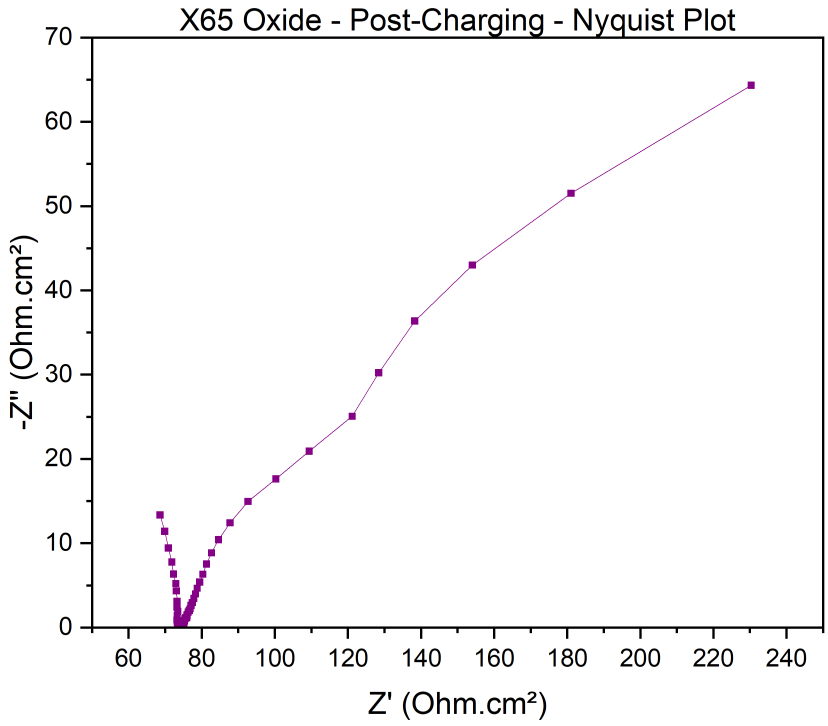

Figure 4.41: Nyquist plot ($-Z''$ vs. Z') for the X65 oxide sample post hydrogen charging.

The Bode magnitude plot (shown in Figure 4.42) shows a marked reduction in impedance ($|Z|$) at low frequencies compared to the uncharged condition. The intermediate-frequency slope becomes steeper, consistent with a reduced capacitive contribution. The plateau at low frequencies remains present but with lower impedance values, highlighting the diminished barrier effect of the oxide layer after hydrogen charging.

The Bode phase angle plot (shown in Figure 4.43) shows a reduced maximum phase angle of $-80°$, indicating a decrease in the capacitive response of the oxide layer. The frequency at which the phase angle transitions from resistive to capacitive behaviour shifts slightly, suggesting changes in the charge transfer dynamics due to hydrogen ingress.

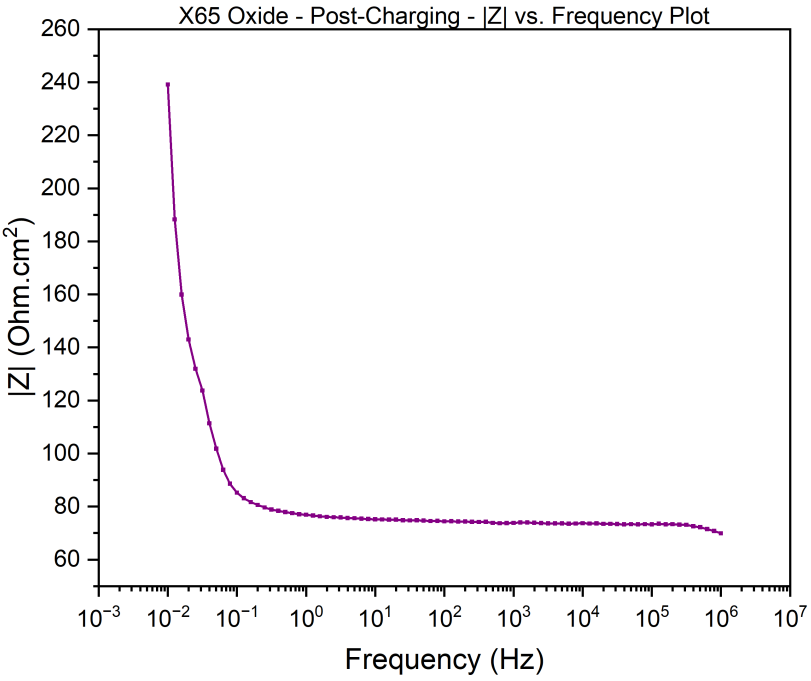

Figure 4.42: Bode magnitude plot ($|Z|$ vs. Frequency) for the X65 oxide sample post hydrogen charging.

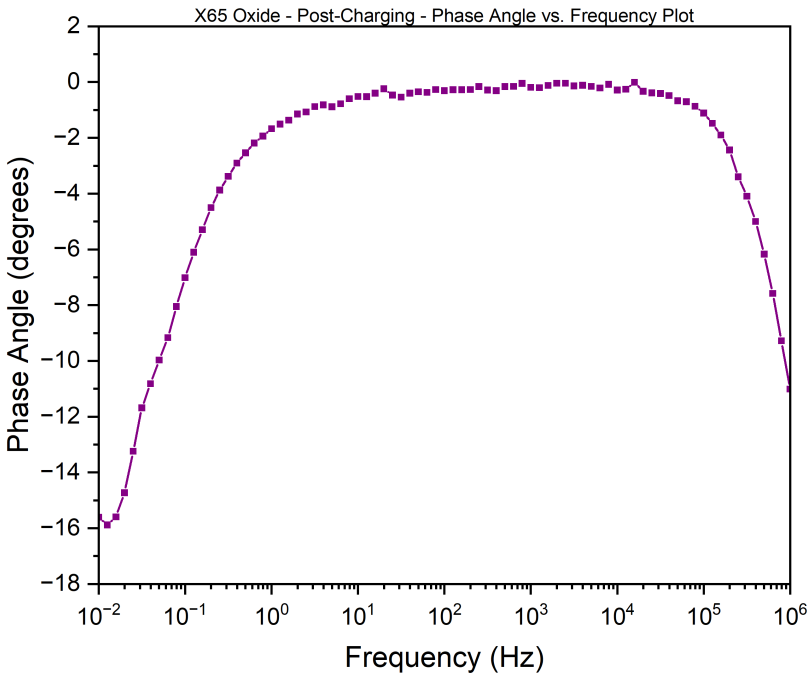

Figure 4.43: Bode phase angle plot (Phase Angle vs. Frequency) for the X65 oxide sample post hydrogen charging.

The Nyquist plots for oxide-covered steel (Figures 4.38 and 4.41) reveal a significant reduction in impedance values after hydrogen charging, with the arc diameter decreasing substantially. This indicates a notable loss in charge transfer resistance (R_1) and a degradation of the oxide layer's protective properties.

In the uncharged condition, the oxide-covered steel initially exhibits lower impedance values compared to the uncharged bare steel. This observation suggests that the oxide layer provides no significant additional protection under these conditions. The lower impedance can be attributed to the porous nature of the oxide layer, which limits its effectiveness as a charge transfer barrier. Furthermore, the oxide layer/steel interface appears to be compromised, potentially isolating the oxide layer from the underlying bare steel and reducing its protective capability.

The Bode plots further support these observations, showing a pronounced decrease in impedance at low frequencies after hydrogen charging. This reduction reflects the diminished resistance of the oxide layer to charge transfer, indicating that its stability is substantially compromised under prolonged hydrogen exposure. The corresponding phase angle plots reveal a decrease in capacitive behaviour post-charging, further suggesting destabilization of the oxide layer and an increase in surface reactivity.

To confirm these findings and better understand the behaviour of the oxide layer post-charging, further investigation of the post-charging oxide layer surface was performed using optical microscopy. Figure 4.44 illustrates the interface region of the oxide layer, transitioning from the unexposed area (brown region) to the hydrogen-charged area (blackish region).

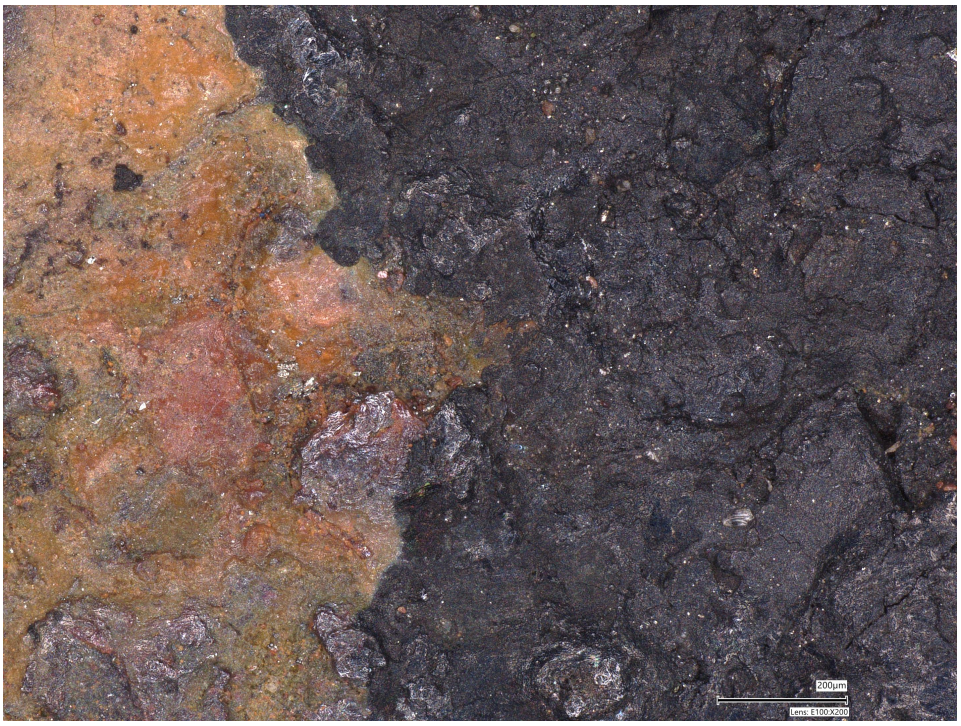

Figure 4.44: Uncharged and post-charging oxide layer interface region at 200x magnification.

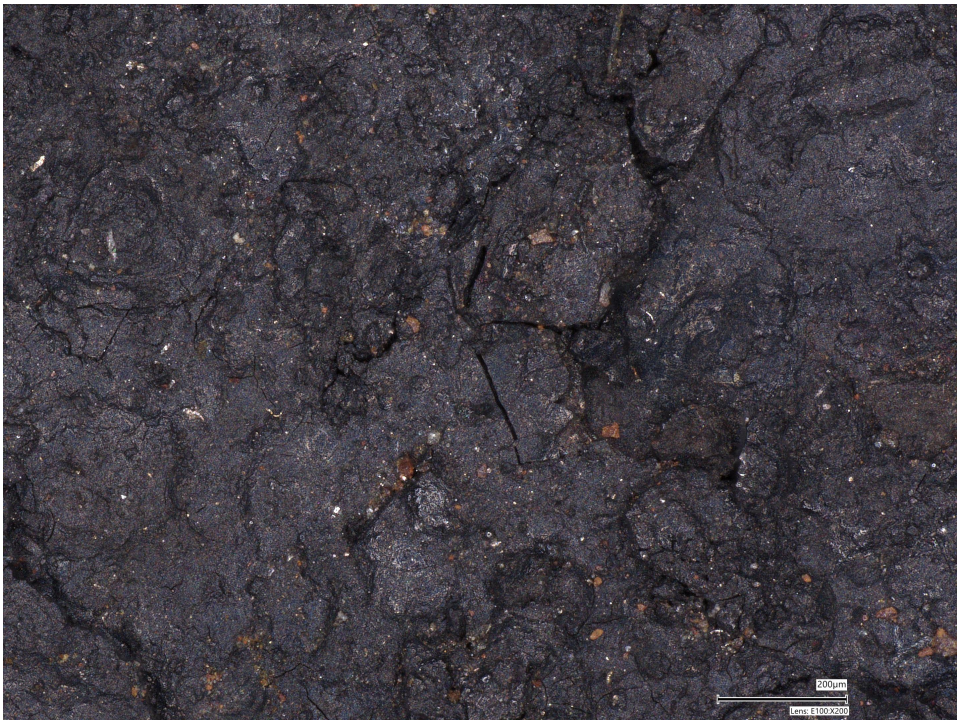

Figure 4.45: Post-charging oxide layer surface at 200x magnification.

Figure 4.46: Post-charging oxide layer surface at 500x magnification.

The optical microscopy images of the oxide layer post-hydrogen charging, shown in Figures 4.45 and 4.46, reveal the presence of numerous cracks and surface defects. At 200x magnification, as seen in Figure 4.45, the surface shows clear discontinuities, indicating mechanical degradation of the oxide layer. These features become more prominent at higher magnifica-

tion (500x, Figure 4.46), where cracks and voids are evident across the oxide layer. These observations suggest that hydrogen charging leads to the formation of cracks and defects, compromising the structural integrity and protective properties of the oxide layer. Such defects may facilitate hydrogen diffusion, reducing the oxide's barrier effectiveness.

Characterization techniques such as scanning electron microscopy (SEM) could provide additional insights into changes in oxide morphology, porosity, and interface integrity after hydrogen exposure.

In summary, while the oxide layer initially presents as a physical barrier, its porous structure and poor interface adhesion significantly reduce its long-term effectiveness. Prolonged hydrogen charging leads to substantial degradation of the structural integrity of the oxide layer, highlighting its limitations in mitigating hydrogen ingress.

5

Discussion

Oxide Layer Characteristics

The as-received surface oxide layer present on X65 steel exhibits a complex, multi-phase composition as revealed by Raman spectroscopy. It consists of haematite (α-Fe_2O_3) and magnetite (Fe_3O_4) or maghemite (γ-Fe_2O_3) beneath a top layer of oxyhydroxides, including goethite (α-FeOOH) and lepidocrocite (γ-FeOOH). This layered structure indicates that the oxide layer is formed through a combination of high-temperature processes, likely occurring during steel processing, and subsequent environmental exposure under ambient conditions.

The thickness of the oxide layer varies significantly, ranging from $27.9\,\mu$m to $63.8\,\mu$m, with an average of $42.7\,\mu$m. Optical microscopy and elemental mapping using SEM-EDS demonstrate a uniform distribution of Fe and O across the thickness of the layer, with minor contributions from Mn and residual C. This consistent composition suggests that the oxide layer is structurally integrated rather than stratified into chemically distinct regions.

While Raman spectroscopy provided valuable qualitative insights into the chemical composition and phase distribution of the oxide layer, the study was limited by the inability to obtain detailed sub-surface maps due to noisy spectral mapping data. Future work will aim to repeat Raman spectral mapping with optimized acquisition parameters to better understand spatial variations within the oxide layer. Moreover, quantitative characterization techniques, such as X-ray photoelectron spectroscopy (XPS) or time-of-flight secondary ion mass spectrometry (ToF-SIMS), could provide detailed compositional analysis, enabling a more comprehensive understanding of the oxide layer's composition and the subsequent variation with depth.

These planned approaches will complement the qualitative findings presented here, providing a deeper understanding of the oxide layer's structure and its implications for material performance. Quantitative data will also allow for a more precise evaluation of the oxide layer's role in mitigating hydrogen ingress and its stability under varying environmental conditions. variability in the oxide's barrier properties.

Influence of Surface Oxide Layers on Hydrogen Permeation

Hydrogen permeation experiments conducted using the DS technique provided insights into the influence of surface oxide layers on hydrogen diffusion. For the bare steel, the diffusion coefficient (D_{eff}) was determined to be $3.46 \times 10^{-6}\,\text{cm}^2/\text{s}$. In comparison, the as-received oxide layer exhibited significantly lower diffusion coefficients of $5.57 \times 10^{-10}\,\text{cm}^2/\text{s}$ (for DS test

1) and 7.13×10^{-11} cm^2/s (DS test 2).

These findings indicate that the surface oxide layer delays hydrogen permeation by slowing its diffusion through the steel. The reduction in hydrogen diffusion coefficient suggests that the oxide layer introduces a retarding effect, temporarily slowing down hydrogen ingress. However, the presence of porosities and localized defects within the oxide layer, as observed in the post-charging optical microscopy images, likely provides pathways for hydrogen transport [72], preventing the oxide from acting as an absolute barrier.

The hydrogen diffusion coefficient for X65 steel reported in the literature varies depending on the microstructure and experimental conditions. For instance, Koren et al. [128] reported diffusion coefficients of 1.50×10^{-6} cm^2/s and 8.78×10^{-7} cm^2/s for Modern and Vintage X65 pipeline steels, respectively, at 25°C using in-situ desorption methods. Similarly, Ma et al. [101] reported an average diffusion coefficient of 7.16×10^{-7} cm^2/s for X65 steel under electrochemical charging conditions in NS4 solution (simulated groundwater). Fallahmohammadi et al. [129] provided a range of diffusion coefficients for X65 steel depending on the microstructure: 2.25×10^{-6} cm^2/s for quenched and tempered samples, and 5.69×10^{-7} cm^2/s for annealed samples. The diffusion coefficient obtained for the bare steel sample in this study (3.46×10^{-6} cm^2/s) is consistent with the upper range of reported values, highlighting the influence of differences in methodology, experimental parameters, and steel microstructure.

In comparison, the oxide layer significantly reduced hydrogen permeation, with diffusion coefficients of 5.57×10^{-10} cm^2/s and 7.13×10^{-11} cm^2/s. However, these values differ substantially from those reported by Ma et al. [101], who observed hydrogen diffusion coefficients between 10^{-18} cm^2/s and 10^{-16} cm^2/s for air-formed anodic oxide layers on X65 steel. This discrepancy likely arises from differences in the nature of the oxide layers. While the oxides in Ma et al.'s study were anodically formed in controlled conditions, the oxide layers in this study were naturally formed and more porous, thus exhibiting lower resistance to hydrogen diffusion. Furthermore, the oxide layer system in this study had not reached steady state during the experiments, and the values were approximations. Consequently, the actual time lag values for the oxide layer tested in this study would be higher, indicating that the layer provides some degree of delay to hydrogen transport.

A notable limitation of this study is the simultaneous reduction of the oxide layer during hydrogen permeation experiments, which may have influenced the observed permeation behaviour. The reduction of oxyhydroxide species such as goethite (α-FeOOH) and lepidocrocite (γ-FeOOH) to oxides such as magnetite (Fe_3O_4) under the applied conditions could alter the oxide layer's resistance. To isolate the contribution of hydrogen permeation alone, future studies could incorporate a palladium (Pd) layer deposited over the oxide on the entry surface to protect the layer from reduction. This approach would allow for a more accurate assessment of the oxide layer's diffusion resistance.

To summarize, the oxide layer serves as a hindrance to hydrogen transport rather than a true barrier, and this ability to delay permeation diminishes under prolonged hydrogen exposure. Electrochemical experiments further revealed evidence of hydrogen-induced degradation, suggesting that hydrogen gradually compromises the oxide layer's structural integrity.

Impact of Hydrogen Charging on Electrochemical Response

This study aimed to evaluate the influence of hydrogen charging on the electrochemical response of both the X65 Bare and X65 Oxide samples. Results from OCP, EIS, and CV measurements demonstrate distinct behaviours for the two sample types under hydrogen charging

conditions.

For the X65 Bare samples, the uncharged surface exhibited an upward trend in OCP, indicating the progressive formation of a passive oxide layer in the alkaline electrolyte, which reduced surface reactivity and stabilized its electrochemical behaviour. However, hydrogen charging caused a dramatic shift in the surface response, with EIS and CV results showing increased surface reactivity. EIS analysis revealed a substantial reduction in charge transfer resistance (R_{ct}), suggesting enhanced reaction kinetics at the electrode-electrolyte interface due to the breakdown of the protective passive film and activation of new reactive sites. Similarly, the Bode plots indicated reduced impedance magnitude ($|Z|$) across all frequencies and a decline in double-layer capacitance (C_{dl}), likely caused by hydrogen-induced defects at the surface. The CV data further supported these findings, showing higher current densities and enhanced faradaic activity post-charging [122, 125], driven by hydrogen destabilizing the passive film and exposing more active sites. Collectively, these results indicate that hydrogen charging compromises the passivated state of bare X65 steel, making it more reactive and less stable under electrochemical conditions. Previous literature [130, 131] on iron and microalloyed X70 steel also highlighted a similar decrease in charge transfer resistance and stability of the passive film post-hydrogen charging.

For the X65 Oxide samples, hydrogen charging had a markedly different impact. The as-received oxide layer exhibited a downward trend in OCP over time, reflecting its gradual destabilization in the electrolyte due to dissolution of unstable surface phases, such as lepidocrocite (γ-FeOOH) and goethite (α-FeOOH). Compared to the bare steel, the initial impedance of the oxide-covered steel was lower, highlighting the non-protective nature of the oxide layer due to defects, cracks, or porosities that allow electrolyte penetration.

Hydrogen charging further exacerbated the vulnerabilities of the oxide-covered steel. EIS data showed a significant reduction in both R_{ct} and impedance magnitude, and the Bode phase plots revealed a loss of C_{dl}. These observations suggest that hydrogen embrittled the oxide layer and penetrated pre-existing defects, transitioning the surface to a highly reactive state dominated by faradaic processes. This response contrasts with that of the bare steel, where the absence of pre-existing porous oxides enabled the formation of a relatively more stable passive layer post-charging.

Overall, the findings demonstrate that while hydrogen charging compromises the electrochemical stability of both bare and oxide-covered X65 steel surfaces, the extent of degradation is greater for the oxide-covered steel due to the intrinsic weaknesses of the oxide layer. These insights highlight that hydrogen-induced degradation in the oxide layer indicates its inability to effectively protect pipeline steel from hydrogen permeation, underscoring the need for further investigation into the role of internal surface oxides in mitigating hydrogen ingress.

6

Conclusions

This research investigated the characteristics of the as-received oxide layer on API 5L X65 steel and its influence on hydrogen permeation and electrochemical behaviour. The study combined oxide layer characterization, hydrogen permeation testing, and electrochemical analysis to evaluate the interaction between hydrogen and the oxide layer under alkaline conditions. The findings provide a comprehensive understanding of the role of surface oxides in controlling hydrogen ingress and their limitations.

- **Oxide Layer Characteristics:** The as-received oxide layer exhibited a mixed composition of haematite (α-Fe_2O_3) and magnetite (Fe_3O_4), with surface oxyhydroxides such as goethite (α-FeOOH) and lepidocrocite (γ-FeOOH). SEM-EDS analysis revealed uniform elemental distribution, but the layer was porous and variable in thickness ($27.9\,\mu$m to $63.8\,\mu$m, average $42.7\,\mu$m).
- **Experimental Considerations:** The hydrogen permeation experiments utilized a D-S setup with distinct galvanostatic and potentiostatic charging conditions. While galvanostatic charging resulted in surface changes due to high current density, potentiostatic charging allowed for more controlled evaluation of hydrogen diffusion.
- **Hydrogen Diffusion Experiments:** The oxide layer delayed hydrogen permeation compared to bare steel, as evidenced by its lower diffusion coefficient values ($D_{\text{eff1}} = 5.57 \times 10^{-10}\,\text{cm}^2/\text{s}$ and $D_{\text{eff2}} = 7.13 \times 10^{-11}\,\text{cm}^2/\text{s}$). However, its effectiveness was hindered by structural porosity and defects, emphasizing the need for further investigation into the mechanisms governing hydrogen transport through oxide layers.
- **Impact of Hydrogen-Oxide Interaction:** Electrochemical experiments demonstrated the destabilization of both bare and oxide-covered steel surfaces following hydrogen charging. The oxide layer exhibited significant reductions in charge transfer resistance and double-layer capacitance, indicating hydrogen-induced damage. The observed degradation highlights the limited capacity of the oxide layer to act as a long-term hydrogen barrier.

In summary, this study demonstrates the utility of a combined methodological approach to characterizing oxide layers and evaluating their interaction with hydrogen. Future work should focus on extending this methodology to investigate other types of oxide layers and their behaviour under controlled gaseous hydrogen charging conditions. These insights will provide a more detailed understanding of oxide-hydrogen interactions and contribute to the broader field of hydrogen embrittlement mitigation in pipeline steels.

7

Recommendations

The following recommendations are proposed to enhance the understanding of hydrogen interaction with the surface oxide layers and the steel substrate, as well as to build on the findings of this study:

1. **Perform Multiple Repetitions of Key Experiments:** Conduct repeated hydrogen permeation tests and EIS measurements under identical conditions to ensure the reliability and reproducibility of the data.
2. **Utilize Additional Quantitative Characterization Techniques:** Utilize quantitative characterization techniques to gain information on the amount of oxides and oxyhydroxides present in the surface oxide layer. Additionally, employ techniques such as X-ray Diffraction (XRD) to identify crystalline phases within the surface oxide layer, including compounds not identifiable by Raman spectroscopy.
3. **SEM Investigation of X65 Bare and Oxide Samples Post-Charging:** Perform SEM analysis of the X65 Bare and X65 Oxide sample surfaces post-hydrogen charging to identify cracks, defects and porosities formed during hydrogen charging and supplement the CV and EIS findings.
4. **Expand Experimental Parameters:** Broaden the scope of permeation tests by varying experimental parameters such as charging time, discharging time, pH of the charging solution, and the concentration of the charging solution. This approach will allow for a more comprehensive understanding of hydrogen permeation behaviour through the oxide layer compared to bare steel.
5. **Focused Permeation Experiments with Palladium (Pd) Coating:** Conduct hydrogen permeation experiments with a coating of Pd on the entry surface (covering both the steel and oxide layer). This will help isolate and focus on hydrogen diffusion specifically through the oxide layer, reducing interference from other surface phenomena.
6. **Gaseous Hydrogen Charging Experiments:** Conduct hydrogen charging experiments under gaseous conditions to study hydrogen permeation through the oxide layer in a non-electrochemical environment. This can serve to establish a link between electrochemical hydrogen charging and gaseous hydrogen charging methods, providing insights into how the oxide layer behaves under different charging conditions.
7. **Mechanical Testing for Hydrogen Embrittlement:** Follow up with mechanical experiments to assess the impact of hydrogen embrittlement on the X65 steel. Compare the

results for steel with and without an oxide layer to understand the protective role of the oxide layer in mitigating embrittlement.

By implementing these recommendations, future studies can build on the findings of this research, offering deeper insights into hydrogen-steel interactions in the presence of surface oxide layers.

References

[1] Daisuke Mizuno et al. “Recent activities in ISIJ HLP research committee corrosion working group: Proposal of pH buffer test solution for fitness-for-purpose HIC evaluations”. In: *ISIJ International* 56.3 (2016), pp. 498–503.

[2] J Bauer et al. “Microstructure and properties of thermomechanical controlled processing steels for linepipe applications”. In: *Ironmaking & steelmaking* 32.4 (2005), pp. 325–330.

[3] American Petroleum Institute. *Specification for Line Pipe*. 46th. API Specification 5L. 2018. url: `https://www.apiwebstore.org/standards/5L`.

[4] Tom Depover et al. “Understanding the interaction between a steel microstructure and hydrogen”. In: *Materials* 11.5 (2018), p. 698.

[5] R Silverstein and D Eliezer. “Mechanisms of hydrogen trapping in austenitic, duplex, and super martensitic stainless steels”. In: *Journal of Alloys and Compounds* 720 (2017), pp. 451–459.

[6] S Birosca, D Dingley, and RL Higginson. “Microstructural and microtextural characterization of oxide scale on steel using electron backscatter diffraction”. In: *Journal of microscopy* 213.3 (2004), pp. 235–240.

[7] Jan Wielant et al. “Electronic properties of thermally formed thin iron oxide films”. In: *Electrochimica Acta* 52.27 (2007), pp. 7617–7625.

[8] PB Sewell, CD Stockbridge, and M Cohen. “An electrometric and electron diffraction study of air-formed oxide films on iron”. In: *Journal of The Electrochemical Society* 108.10 (1961), p. 933.

[9] D Gilroy and JEO Mayne. “The oxidation of iron at room temperature”. In: *Corrosion Science* 5.1 (1965), pp. 55–58.

[10] SI Ali and GC Wood. “Oxidation of iron at room temperature”. In: *British Corrosion Journal* 4.3 (1969), pp. 133–137.

[11] HJ Mathieu, M Datta, and D Landolt. “Thickness of natural oxide films determined by AES and XPS with/without sputtering”. In: *Journal of Vacuum Science & Technology A: Vacuum, Surfaces, and Films* 3.2 (1985), pp. 331–335.

[12] Sungkyu Lee and Roger W Staehle. “Coulometric reduction of oxides formed on copper, nickel, and iron”. In: *Journal of the Electrochemical Society* 142.7 (1995), p. 2189.

[13] S Suzuki et al. “Native oxide layers formed on the surface of ultra high-purity iron and copper investigated by angle resolved XPS”. In: *Materials Transactions, JIM* 38.11 (1997), pp. 1004–1009.

[14] Hidetaka Konno, Masato Kawai, and Masaichi Nagayama. “The mechanism of spontaneous dissolution of the air-formed oxide film on iron in a deaerated neutral phosphate solution”. In: *Surface technology* 24.3 (1985), pp. 259–271.

[15] AP Grosvenor, BA Kobe, and NS McIntyre. “Studies of the oxidation of iron by air after being exposed to water vapour using angle-resolved x-ray photoelectron spectroscopy and QUASES™”. In: *Surface and Interface Analysis: An International Journal devoted to the development and application of techniques for the analysis of surfaces, interfaces and thin films* 36.13 (2004), pp. 1637–1641.

[16] Shigeru Suzuki, Katsuyuki Yanagihara, and Kichinosuke Hirokawa. “XPS study of oxides formed on the surface of high-purity iron exposed to air”. In: *Surface and Interface Analysis: An International Journal devoted to the development and application of techniques for the analysis of surfaces, interfaces and thin films* 30.1 (2000), pp. 372–376.

[17] G Chan-Rosado and MA Pech-Canul. “Influence of native oxide film age on the passivation of carbon steel in neutral aqueous solutions with a dicarboxylic acid”. In: *Corrosion Science* 153 (2019), pp. 19–31.

[18] Brian R Strohmeier. “An ESCA method for determining the oxide thickness on aluminum alloys”. In: *Surface and interface analysis* 15.1 (1990), pp. 51–56.

[19] M Pl Seah and WA Dench. “Quantitative electron spectroscopy of surfaces: A standard data base for electron inelastic mean free paths in solids”. In: *Surface and interface analysis* 1.1 (1979), pp. 2–11.

[20] I Frateur et al. “Role of pH and calcium ions in the adsorption of an alkyl N-aminodimethylphosphonate on steel: An XPS study”. In: *Applied surface science* 252.8 (2006), pp. 2757–2769.

[21] RP Frankenthal, PC Milner, and DJ Siconolfi. “Long-Term Atmospheric Oxidation of High Purity Iron”. In: *Journal of the Electrochemical Society* 132.5 (1985), p. 1019.

[22] K Asami and K Hashimoto. “An X-ray photo-electron spectroscopic study of surface treatments of stainless steels”. In: *Corrosion Science* 19.7 (1979), pp. 1007–1017.

[23] Antonella Rossi, G Puddu, and B Elsener. “The surface of iron and Fe10Cr alloys in alkaline media”. In: *Corrosion of reinforcement in concrete* (2001), p. 44.

[24] M Flori et al. “A study of the 42CrMo4 steel surface by quantitative XPS electron spectroscopy”. In: *Applied surface science* 254.15 (2008), pp. 4738–4743.

[25] Maurizio Olla et al. “Nondestructive in-depth composition profile of oxy-hydroxide nanolayers on iron surfaces from ARXPS measurement”. In: *Surface and Interface Analysis: An International Journal devoted to the development and application of techniques for the analysis of surfaces, interfaces and thin films* 38.5 (2006), pp. 964–974.

[26] Díaz de la Fuente et al. “Long-term atmospheric corrosion of mild steel”. In: *Corrosion Science* 53.2 (2011), pp. 604–617.

[27] Iván Diaz et al. “Atmospheric corrosion of Ni-advanced weathering steels in marine atmospheres of moderate salinity”. In: *Corrosion Science* 76 (2013), pp. 348–360.

[28] Jenifer Alcántara et al. “Marine atmospheric corrosion of carbon steel: A review”. In: *Materials* 10.4 (2017), p. 406.

[29] Kui Xiao et al. “Corrosion products and formation mechanism during initial stage of atmospheric corrosion of carbon steel”. In: *Journal of Iron and Steel Research International* 15.5 (2008), pp. 42–48.

[30] Kikuchi Asami and M Kikuchi. “In-depth distribution of rusts on a plain carbon steel and weathering steels exposed to coastal–industrial atmosphere for 17 years”. In: *Corrosion Science* 45.11 (2003), pp. 2671–2688.

[31] Vladimir B Ginzburg. *Steel-rolling technology: theory and practice*. CRC Press, 1989.

[32] MM Wolf. “Scale formation and descaling in continuous casting and hot rolling. Part VII”. In: *Iron Steelmaker* 27 (2000), pp. 63–64.

[33] MM Wolf. “Scale formation and descaling in continuous casting and hot rolling. Part VII”. In: *Iron Steelmaker* 27 (2000), pp. 114–115.

[34] RY Chen and WYD Yeun. “Review of the high-temperature oxidation of iron and carbon steels in air or oxygen”. In: *Oxidation of metals* 59.5 (2003), pp. 433–468.

[35] RY Chen and WYD Yuen. “Oxidation of low-carbon, low-silicon mild steel at 450–900 C under conditions relevant to hot-strip processing”. In: *Oxidation of metals* 57.1 (2002), pp. 53–79.

[36] D Caplan and M Cohen. “Scaling of iron at 500 C”. In: *Corrosion Science* 3.3 (1963), 139–IN2.

[37] WE Boggs and RH Kachik. “The Oxidation of Iron-Carbon Alloys at 500 C”. In: *Journal of the electrochemical Society* 116.4 (1969), p. 424.

[38] Zhi-Feng Li et al. “High-efficiency reduction behavior for the oxide scale formed on hot-rolled steel in a mixed atmosphere of hydrogen and argon”. In: *Journal of Materials Science* 55.4 (2020), pp. 1826–1839.

[39] M. H. Davies, M. T. Simnad, and C. E. Birchenall. “Heat Transfer to Boiling Metals”. In: *Transactions of the American Institute of Mining, Metallurgical, and Petroleum Engineers* 193 (1953), pp. 1250–1256.

[40] WW Smeltzer and DJ Young. “Oxidation properties of transition metals”. In: *Progress in Solid State Chemistry* 10 (1975), pp. 17–54.

[41] Fumio Matsuno. “Blistering and hydraulic removal of scale films of rimmed steel at high temperature”. In: *Transactions of the Iron and Steel Institute of Japan* 20.6 (1980), pp. 413–421.

[42] R Griffiths. “The blistering of iron oxide scales and the conditions for the formation of a non-adherent scale”. In: *J. iron steel Inst* 130 (1934).

[43] R Rolls. “Scale blisters on ferrous alloys”. In: *ATB Metallurgie* 7.2 (1967), pp. 53–60.

[44] CA Siebert and C Upthegrove. “Oxidation of a low carbon steel in the temperature 1650 to 2100° F”. In: *Transactions of the American Society for Metals* 23 (1935), pp. 187–224.

[45] CA Siebert. “The effect of carbon content on the rate of oxidation of steel in air at high temperatures”. In: *Transactions of the American Society for Metals* 27 (1939), pp. 752–757.

[46] Harish D Merchant. “Oxidation kinetics of iron-carbon base alloys”. In: *Oxidation of metals* 2.2 (1970), pp. 145–153.

[47] J Baud et al. “The oxidation and decarburizing of Fe-C alloys in air and the influence of relative humidity”. In: *Oxidation of metals* 9.1 (1975), pp. 69–97.

[48] A G Goursat and WW Smeltzer. “Kinetics and morphological development of the oxide scale on iron at high temperatures in oxygen at low pressure”. In: *Oxidation of Metals* 6 (1973), pp. 101–116.

[49] H Abuluwefa, RIL Guthrie, and Frank Ajersch. “The effect of oxygen concentration on the oxidation of low-carbon steel in the temperature range 1000 to 1250 C”. In: *Oxidation of Metals* 46 (1996), pp. 423–440.

[50] B Gleeson, SMM Hadavi, and DJ Young. “Isothermal transformation behavior of thermally-grown wüstite”. In: *Materials at High Temperatures* 17.2 (2000), pp. 311–318.

[51] RA Oriani. “Hydrogen embrittlement of steels”. In: *Annual review of materials science* 8.1 (1978), pp. 327–357.

[52] RP Frohmberg, WJ Barnett, and AR Troiano. *Delayed failure and hydrogen embrittlement in steel*. Wright Air Development Center, Air Research and Development Command, United …, 1954.

[53] E Legrand et al. “Computational analysis of geometrical factors affecting experimental data extracted from hydrogen permeation tests: II–consequences of trapping and an oxide layer”. In: *international journal of hydrogen energy* 37.18 (2012), pp. 13574–13582.

[54] Gianfranco Lovicu et al. “Hydrogen embrittlement of automotive advanced high-strength steels”. In: *Metallurgical and Materials Transactions A* 43 (2012), pp. 4075–4087.

[55] M Loidl et al. “Characterization of hydrogen embrittlement in automotive advanced high strength steels”. In: *Materialwissenschaft und Werkstofftechnik* 42.12 (2011), pp. 1105–1110.

[56] Enyinnaya Ohaeri, Ubong Eduok, and Jerzy Szpunar. “Hydrogen related degradation in pipeline steel: A review”. In: *International Journal of Hydrogen Energy* 43.31 (2018), pp. 14584–14617.

[57] Olga Barrera et al. “Understanding and mitigating hydrogen embrittlement of steels: a review of experimental, modelling and design progress from atomistic to continuum”. In: *Journal of materials science* 53.9 (2018), pp. 6251–6290.

[58] Harshad Kumar Dharamshi Hansraj Bhadeshia. “Prevention of hydrogen embrittlement in steels”. In: *ISIJ international* 56.1 (2016), pp. 24–36.

[59] Hung M Ha, Jia-He Ai, and John R Scully. “Effects of prior cold work on hydrogen trapping and diffusion in API X-70 line pipe steel during electrochemical charging”. In: *Corrosion* 70.2 (2014), pp. 166–184.

[60] VP Ramunni, T De Paiva Coelho, and PE Valadaes de Miranda. “Interaction of hydrogen with the microstructure of low-carbon steel”. In: *Materials Science and Engineering: A* 435 (2006), pp. 504–514.

[61] KO Findley, MK O’Brien, and H Nako. “Critical Assessment 17: Mechanisms of hydrogen induced cracking in pipeline steels”. In: *Materials Science and Technology* 31.14 (2015), pp. 1673–1680.

[62] Stan Lynch. “Hydrogen embrittlement phenomena and mechanisms”. In: *Corrosion reviews* 30.3-4 (2012), pp. 105–123.

[63] MI Luppo and J Ovejero-Garcia. “The influence of microstructure on the trapping and diffusion of hydrogen in a low carbon steel”. In: *Corrosion science* 32.10 (1991), pp. 1125–1136.

[64] WC Luu and JK Wu. “The influence of microstructure on hydrogen transport in carbon steels”. In: *Corrosion Science* 38.2 (1996), pp. 239–245.

[65] Tim Rubben et al. “Influence of thermal oxide layers on the hydrogen transport through the surface of SAE 1010 steel”. In: *Journal of The Electrochemical Society* 169.11 (2022), p. 111503.

[66] Lorenzo Vecchi et al. “Modelling of hydrogen permeation experiments in iron alloys: Characterization of the accessible parameters–Part I–The entry side”. In: *Electrochimica Acta* 262 (2018), pp. 57–65.

[67] L Vecchi et al. “A modelling approach on the impact of an oxide layer on the hydrogen permeation through iron membranes in the Devanathan-Stachurski cell”. In: *Electrochimica Acta* 286 (2018), pp. 139–147.

[68] T Chikada et al. “Surface behaviour in deuterium permeation through erbium oxide coatings”. In: *Nuclear Fusion* 51.6 (2011), p. 063023.

[69] Qun Li et al. “Thickness impacts on permeation reduction factor of Er2O3 hydrogen isotopes permeation barriers prepared by magnetron sputtering”. In: *International Journal of Hydrogen Energy* 41.4 (2016), pp. 3299–3306.

[70] Qun Li et al. “Study on influence factors of permeation reduction factor of Al2O3-hydrogen isotopes permeation barriers”. In: *International Journal of Hydrogen Energy* 41.7 (2016), pp. 4326–4331.

[71] Y Ishikawa, T Yoshimura, and M Arai. “Effect of surface oxides on the permeation of deuterium through stainless steel”. In: *Vacuum* 47.6-8 (1996), pp. 701–704.

[72] Timing Zhang et al. “Effects of surface oxide films on hydrogen permeation and susceptibility to embrittlement of X80 steel under hydrogen atmosphere”. In: *International Journal of Hydrogen Energy* 43.6 (2018), pp. 3353–3365.

[73] De-jun Kong, Yong-zhong Wu, and LONG Dan. “Stress corrosion of X80 pipeline steel welded joints by slow strain test in NACE H2S solutions”. In: *Journal of Iron and Steel Research, International* 20.1 (2013), pp. 40–46.

[74] Chengshuang Zhou et al. “Effect of Oxidation Temperature on the Hydrogen Barrier Properties of X52 Pipeline Steel Surface Oxide Films”. In: *Available at SSRN 4954950* (2024).

[75] Di He et al. “Deuterium permeation of Al2O3/Cr2O3 composite film on 316L stainless steel”. In: *International Journal of Hydrogen Energy* 40.6 (2015), pp. 2899–2903.

[76] Stefan Evers, Ceylan Senöz, and Michael Rohwerder. “Hydrogen detection in metals: a review and introduction of a Kelvin probe approach”. In: *Science and technology of advanced materials* (2013).

[77] Shu Xiao et al. “Hydrogen permeation barriers and preparation techniques: A review”. In: *Journal of Vacuum Science & Technology A* 40.6 (2022).

[78] D Levchuk et al. “Gas-driven deuterium permeation through Al2O3 coated samples”. In: *Physica Scripta* 2004.T108 (2004), p. 119.

[79] Di He et al. “Influence of microstructure on the hydrogen permeation of alumina coatings”. In: *International journal of hydrogen energy* 38.22 (2013), pp. 9343–9348.

[80] Sung Jin Kim and Kyoo Young Kim. “An overview on hydrogen uptake, diffusion and transport behavior of ferritic steel, and its susceptibility to hydrogen degradation”. In: *Corrosion Science and Technology* 16.4 (2017), pp. 209–225.

[81] Shi Zheng et al. “Effect of hydrogen traps on hydrogen permeation in X80 pipeline steel——a joint experimental and modelling study”. In: *International Journal of Hydrogen Energy* 48.12 (2023), pp. 4773–4788.

[82] WY Choo and Jai Young Lee. “Thermal analysis of trapped hydrogen in pure iron”. In: *Metallurgical Transactions A* 13 (1982), pp. 135–140.

[83] Xiusai Xu et al. “Experimental study on the temperature dependence of gaseous hydrogen permeation and hydrogen embrittlement susceptibility of X52 pipeline steel”. In: *Engineering Failure Analysis* 155 (2024), p. 107746.

[84] Zhen Zhao et al. “Hydrogen permeation behavior of QP1180 high strength steel in simulated coastal atmosphere”. In: *journal of materials research and technology* 18 (2022), pp. 2320–2330.

[85] JA Ronevich et al. “Improvement of the hydrogen microprint technique on AHSS steels”. In: *Metallography, Microstructure, and Analysis* 1 (2012), pp. 79–84.

[86] José Ovejero-García. “Hydrogen microprint technique in the study of hydrogen in steels”. In: *Journal of materials science* 20 (1985), pp. 2623–2629.

[87] Alen Thomas and Jerzy A Szpunar. “Hydrogen diffusion and trapping in X70 pipeline steel”. In: *International Journal of Hydrogen Energy* 45.3 (2020), pp. 2390–2404.

[88] Koji Ichitani and Motohiro Kanno. “Visualization of hydrogen diffusion in steels by high sensitivity hydrogen microprint technique”. In: *Science and Technology of Advanced materials* 4.6 (2003), pp. 545–551.

[89] Shigeaki Matsuda, Kouji Ichitani, and Motohiro Kanno. “Visualization of hydrogen diffusion path by a high sensitivity hydrogen microprint technique”. In: *Environment-Induced Cracking of Materials*. Elsevier, 2008, pp. 239–248.

[90] ES Ivanov et al. “Use of impedance spectroscopy for evaluating pipe steel susceptibility towards hydrogenation and hydrogen cracking”. In: *Metallurgist* 56 (2012), pp. 597–603.

[91] XY Peng and YF Cheng. “A comparison of hydrogen permeation and the resulting corrosion enhancement of X65 and X80 pipeline steels”. In: *Canadian Metallurgical Quarterly* 53.1 (2014), pp. 107–111.

[92] Cheng Zeng et al. “Hydrogen interaction characteristic of nanoscale oxide films grown on iron–nickel based stainless steel by selective thermal oxidation”. In: *international journal of hydrogen energy* 42.32 (2017), pp. 20910–20921.

[93] Chilou ZHOU et al. “Review on hydrogen permeation barrier coatings on stainless steels”. In: *Chemical Industry and Engineering Progress* 39.9 (2020), p. 3458.

[94] Yufan Li et al. “Mechanism and evaluation of hydrogen permeation barriers: a critical review”. In: *Industrial & Engineering Chemistry Research* 62.39 (2023), pp. 15752–15773.

[95] Liangliang Liu et al. “Fabrication and hydrogen permeation resistance of dense CrN coatings”. In: *Surface and Coatings Technology* 437 (2022), p. 128326.

[96] Xinfeng Li et al. “Review of hydrogen embrittlement in metals: hydrogen diffusion, hydrogen characterization, hydrogen embrittlement mechanism and prevention”. In: *Acta Metallurgica Sinica (English Letters)* 33 (2020), pp. 759–773.

[97] Lorenzo Vecchi et al. “Modelling of hydrogen permeation experiments in iron alloys: Characterization of the accessible parameters–Part II–The exit side”. In: *Electrochimica Acta* 262 (2018), pp. 153–161.

[98] Qian Liu et al. “Determination of the hydrogen fugacity during electrolytic charging of steel”. In: *Corrosion Science* 87 (2014), pp. 239–258.

[99] Erik Koren et al. “Experimental comparison of gaseous and electrochemical hydrogen charging in X65 pipeline steel using the permeation technique”. In: *Corrosion Science* 215 (2023), p. 111025.

[100] Erik Koren et al. “Investigating electrochemical charging conditions equivalent to hydrogen gas exposure of X65 pipeline steel”. In: *Materials and Corrosion* 75.3 (2024), pp. 315–321.

[101] HC Ma et al. “Influence of iron oxides and calcareous deposits on the hydrogen permeation rate in X65 steel in a simulated groundwater”. In: *International Journal of Hydrogen Energy* 46.9 (2021), pp. 6669–6679.

[102] Peixuan Wang et al. “Investigation of SiC films deposited onto stainless steel and their retarding effects on tritium permeation”. In: *Surface and Coatings Technology* 128 (2000), pp. 99–104.

[103] Yu Liu et al. “Vanadium carbide coating as hydrogen permeation barrier: A DFT study”. In: *International Journal of Hydrogen Energy* 44.12 (2019), pp. 6093–6102.

[104] Vincenc Nemanič. “Hydrogen permeation barriers: Basic requirements, materials selection, deposition methods, and quality evaluation”. In: *Nuclear Materials and Energy* 19 (2019), pp. 451–457.

[105] Bojan Zajec. “Hydrogen permeation barrier–recognition of defective barrier film from transient permeation rate”. In: *International journal of hydrogen energy* 36.12 (2011), pp. 7353–7361.

[106] Cailin Wang et al. “Study on hydrogen embrittlement susceptibility of X80 steel through in-situ gaseous hydrogen permeation and slow strain rate tensile tests”. In: *International Journal of Hydrogen Energy* 48.1 (2023), pp. 243–256.

[107] Yinghao Sun and Y Frank Cheng. “Thermodynamics of spontaneous dissociation and dissociative adsorption of hydrogen molecules and hydrogen atom adsorption and absorption on steel under pipelining conditions”. In: *International Journal of Hydrogen Energy* 46.69 (2021), pp. 34469–34486.

[108] May L Martin et al. “Hydrogen embrittlement in ferritic steels”. In: *Applied physics reviews* 7.4 (2020).

[109] Qidong Li et al. “Hydrogen impact: A review on diffusibility, embrittlement mechanisms, and characterization”. In: *Materials* 17.4 (2024), p. 965.

[110] Eiji Akiyama and Songjie Li. “Electrochemical hydrogen permeation tests under galvanostatic hydrogen charging conditions conventionally used for hydrogen embrittlement study”. In: *Corrosion reviews* 34.1-2 (2016), pp. 103–112.

[111] MA Mohtadi-Bonab et al. “Hydrogen-induced cracking assessment in pipeline steels through permeation and crystallographic texture measurements”. In: *Journal of Materials Engineering and Performance* 25 (2016), pp. 1781–1793.

[112] Anubhav Jain et al. “Commentary: The Materials Project: A materials genome approach to accelerating materials innovation”. In: *APL materials* 1.1 (2013).

[113] Anjli M Patel et al. “Efficient Pourbaix diagrams of many-element compounds”. In: *Physical Chemistry Chemical Physics* 21.45 (2019), pp. 25323–25327.

[114] Arunima K Singh et al. “Electrochemical stability of metastable materials”. In: *Chemistry of Materials* 29.23 (2017), pp. 10159–10167.

[115] Kristin A Persson et al. “Prediction of solid-aqueous equilibria: Scheme to combine first-principles calculations of solids with experimental aqueous states”. In: *Physical Review B—Condensed Matter and Materials Physics* 85.23 (2012), p. 235438.

[116] Monika Hanesch. “Raman spectroscopy of iron oxides and (oxy) hydroxides at low laser power and possible applications in environmental magnetic studies”. In: *Geophysical Journal International* 177.3 (2009), pp. 941–948.

[117] Didier Chicot et al. “Mechanical properties of magnetite (Fe3O4), hematite (α-Fe2O3) and goethite (α-FeO· OH) by instrumented indentation and molecular dynamics analysis”. In: *Materials Chemistry and Physics* 129.3 (2011), pp. 862–870.

[118] RK Singh Raman, B Gleeson, and DJ Young. “Laser Raman spectroscopy: a technique for rapid characterisation of oxide scale layers”. In: *Materials Science and Technology* 14.5 (1998), pp. 373–376.

[119] Dalva LA De Faria, Sérgio Venâncio Silva, and Múcio Tavares de Oliveira. “Raman microspectroscopy of some iron oxides and oxyhydroxides”. In: *Journal of Raman spectroscopy* 28.11 (1997), pp. 873–878.

[120] Philippe Refait et al. “Corrosion of carbon steel in marine environments: role of the corrosion product layer”. In: *Corrosion and Materials Degradation* 1.1 (2020), p. 10.

[121] *Method of Measurement of Hydrogen Permeation and Determination of Hydrogen Uptake and Transport in Metals by an Electrochemical Technique*. Geneva, Switzerland: International Organization for Standardization, 2014. url: `https://www.iso.org/standard/64514.html`.

[122] Dallin J Barton et al. “Towards quantitative analysis of deuterium absorption in ferrite and austenite during electrochemical charging by comparing cyclic voltammetry and cryogenic transfer atom probe tomography”. In: *International Journal of Hydrogen Energy* 50 (2024), pp. 30–40.

[123] Suzanne Joiret et al. “Use of EIS, ring-disk electrode, EQCM and Raman spectroscopy to study the film of oxides formed on iron in 1 M NaOH”. In: *Cement and Concrete Composites* 24.1 (2002), pp. 7–15.

[124] Berk Ozdirik et al. “Development of an electrochemical procedure for monitoring hydrogen sorption/desorption in steel”. In: *Journal of The Electrochemical Society* 164.13 (2017), p. C747.

[125] Berk Ozdirik. “Electrochemical investigation of the hydrogen and steel interaction”. PhD thesis. Vrije Universiteit Brussel, 2018.

[126] Ane C Rovani et al. “Scratch resistance of low-temperature plasma nitrided and carburized martensitic stainless steel”. In: *Wear* 376 (2017), pp. 70–76.

[127] CH Hsu and Florian Mansfeld. “Concerning the conversion of the constant phase element parameter Y0 into a capacitance”. In: *Corrosion* 57.09 (2001).

[128] Erik Koren et al. “Hydrogen diffusivity in X65 pipeline steel: Desorption and permeation studies”. In: *International Journal of Hydrogen Energy* 61 (2024), pp. 1157–1169.

[129] Ehsan Fallahmohammadi et al. “Hydrogen diffusion into three metallurgical microstructures of a C–Mn X65 and low alloy F22 sour service steel pipelines”. In: *International Journal of Hydrogen Energy* 39.25 (2014), pp. 13300–13313.

[130] JG Yu, JL Luo, and PR Norton. “Effects of hydrogen on the electronic properties and stability of the passive films on iron”. In: *Applied surface science* 177.1-2 (2001), pp. 129–138.

[131] YM Zeng, JL Luo, and PR Norton. “New interpretation of the effect of hydrogen on the ion distributions and structure of passive films on microalloyed steel”. In: *Journal of the Electrochemical Society* 151.6 (2004), B291.

A

Raman Spectroscopy

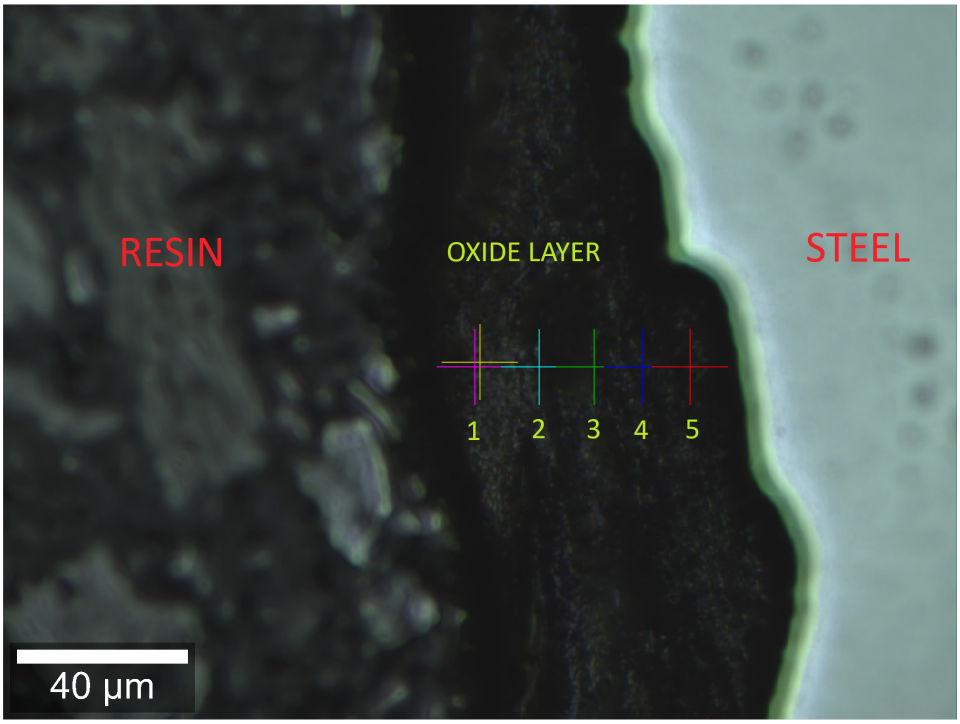

Figure A.1: Optical micrograph showing the cross-section of the oxide layer, with marked locations (1, 2, 3, 4, and 5) indicating depth-wise locations within the oxide layer where Raman spectra were captured.

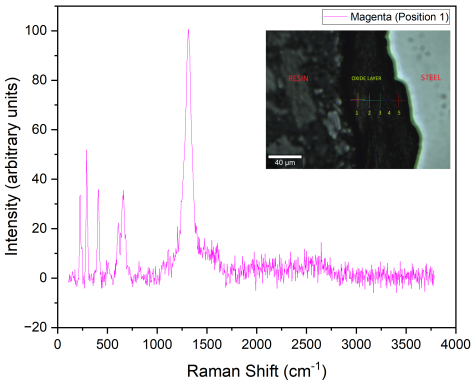

(a) Raman spectrum at location 1.

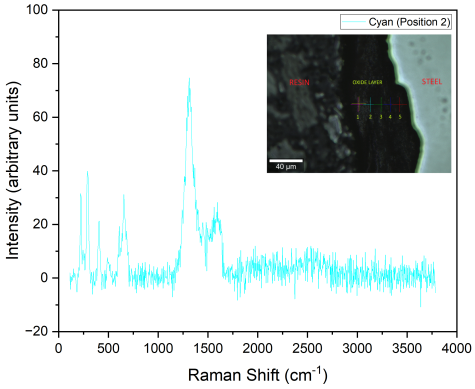

(b) Raman spectrum at location 2.

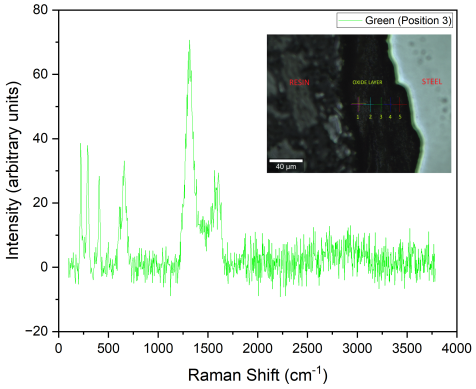

(c) Raman spectrum at location 3.

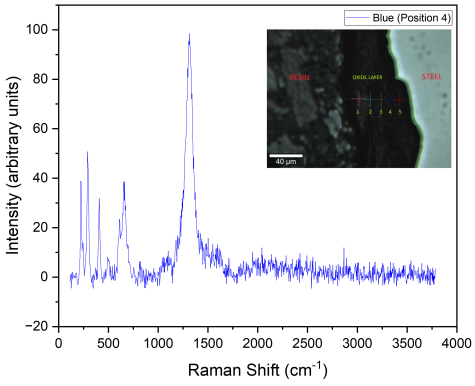

(d) Raman spectrum at location 4.

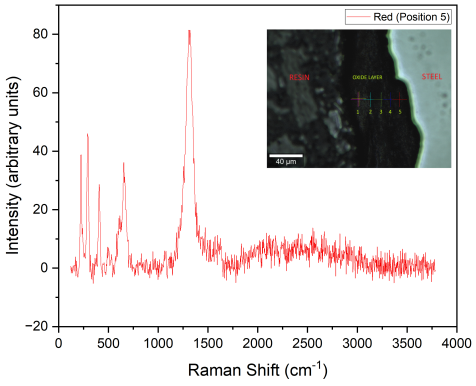

(e) Raman spectrum at location 5.

Figure A.2: Raman spectra at the various locations (1, 2, 3, 4, and 5) within the oxide layer cross-section, with the corresponding microscopic image inset.

B

Palladium Layer Deposition

The palladium (Pd) layer was deposited on the samples using a Leica EM SCD500 sputter coater. The step-by-step procedure for the deposition of a thick 71.1 nm Pd layer is described in Table B.1.

Step No.	Procedure	Parameters
1	**Vacuum Initialization:** Achieve a clean vacuum environment to minimize contamination.	Vacuum Level: 10^{-4} mbar
2	**Surface Cleaning:** Sputter-clean the sample surface in pure argon gas to remove impurities.	• Gas: Pure argon (quality 5.0, Linde Gas) • Pressure: 0.1 mbar • Current: 5 mA • Bias Voltage: 400 V • Duration: 180 s
3	**Restore Vacuum:** Re-establish the vacuum environment after cleaning.	Vacuum Level: 10^{-4} mbar
4	**Target Pre-Cleaning:** Clean the sputter target with the shutter closed before deposition.	Duration: 180 s
5	**Deposition:** Deposit the palladium layer using sputtering.	• Bias Voltage: 370 V • Current: 40 mA • Deposition Rate: 0.12 nm/s • Thickness: 71.1 nm

Table B.1: Step-by-step procedure and parameters for palladium layer deposition.

C

DS Permeation Test - Galvanostatic Charging - Charging Potential

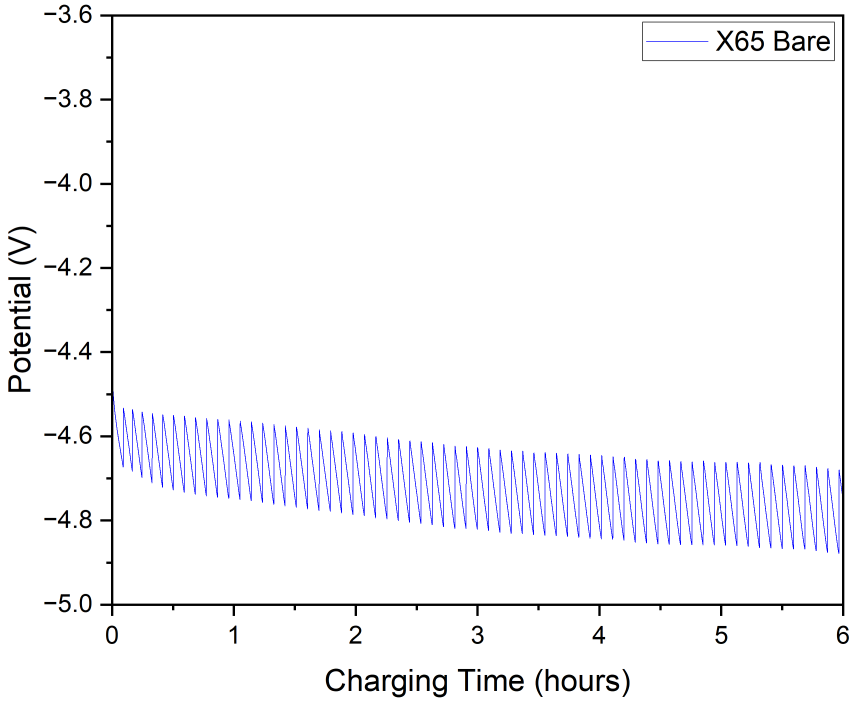

Figure C.1: Potential (V) versus charging time plot for the X65 Bare sample under constant current charging of 5.9 µA/cm^2 over a duration of 6 hours.

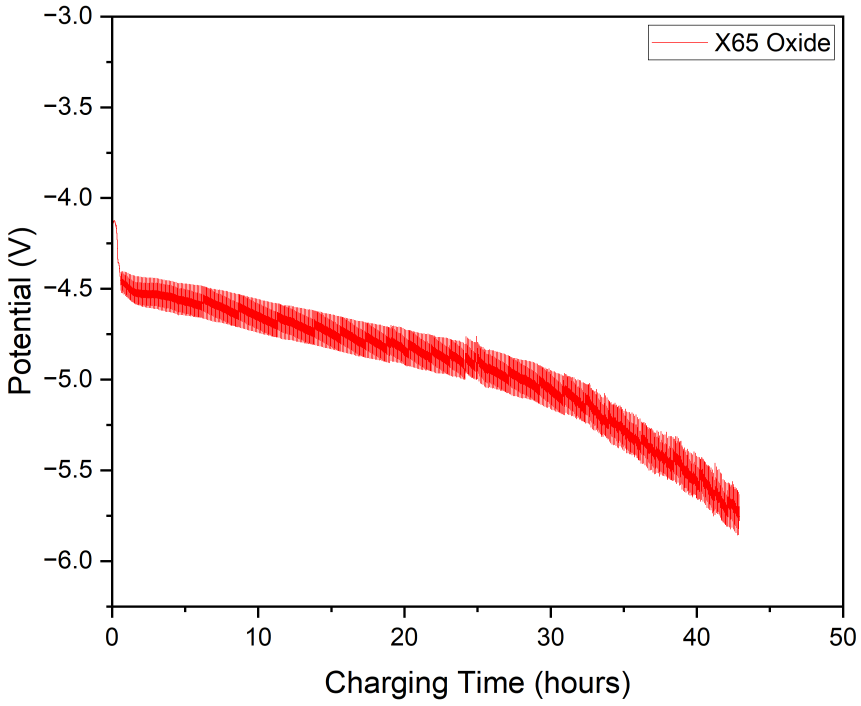

Figure C.2: Potential (V) versus charging time plot for the X65 Oxide sample under constant current charging over a duration of 43 hours.